Precursors for the Solution-Based Formation of $CuInSe_2$ Absorber Layers, Synthesis and Transformation Behaviour

Ruben Dierick

Promotor: Prof. Dr. Ir. Z. Hens
Thesis submitted in fulfillment of the requirements of the degree of Doctor (Ph.D.) in Sciences: Chemistry

Department of Inorganic and Physical Chemistry
Faculty of Sciences
2015

UNIVERSITEIT GENT

Promotor:

Prof. dr. ir. Zeger Hens

Jury:

Prof. dr. Klaartje De Buysser (chair)	Ghent University
Prof. dr. ir. Zeger Hens (promotor)	Ghent University
Prof. dr. Christophe Detavernier	Ghent University
Dr. Guido Huyberechts	Flamac, a division of SIM
Prof. dr. An Hardy	Hasselt University
Dr. Petra Lommens	Ghent University
Dr. Marc Meuris	IMEC

Ghent University
Faculty of Sciences
Department of Inorganic and Physical Chemistry
Krijgslaan 281–S3
9000 Ghent
Belgium

UNIVERSITEIT GENT

Thesis submitted in fulfillment
of the requirements of the degree of
Doctor of Science: Chemistry
2015

Contents

List of Acronyms

DLS	Dynamic light scattering
DMSO	Dimethylsulfoxide
DOSY	Diffusion ordered spectroscopy
DTC	Dithiocarbamate
CIGS	$Cu(In,Ga)(S,Se)_2$
CIS	$CuInS_2$
CISe	$CuInSe_2$
CZTSSe	$Cu_2ZnSn(S,Se)_4$
EDX	Energy-dispersive x-ray spectroscopy
EtOH	Ethanol
FWHM	Full width at half maximum
HSQC	Heteronuclear single quantum coherence
i-ProH	Isopropanol
LED	Light emitting diode
MeOH	Methanol
MS	Mass spectrometry
NC	Nanocrystal
NIR	Near-infrared
NOE	Nuclear Overhauser effect
NOESY	Nuclear Overhauser effect spectroscopy
NP	Nanoparticle
NMR	Nuclear magnetic resonance
OAc	Oleic acid
ODAm	n-Octadecylamine
ODE	1-Octadecene
ODPAc	Octadecylphosphonic acid
OLAm	Oleylamine
PDC	Pyrrolidinedithiocarbamate
PET	Phenylethylthiol

RBS	Rutherford backscattering spectrometry
SEM	Scanning electron microscope
TEM	Transmission electron microscopy
TOP	Trioctyl phosphine
TGA	Thermogravimetric analysis
UDAc	1-undecenoid acid
UV-Vis	Ultra-voilet visible
XPS	X-ray photoelectron spectroscopy
XRF	X-ray fluorescence
XRD	X-ray diffraction

Chapter I

Introduction

1.1 The energy challenge

To meet our ever-increasing demand for energy, we could continue to tear up the Earth's crust to retrieve and burn the limited resources of oil, coal and natural gas which have established over billions of years. Following a business-as usual path of energy use based on fossil fuels will raise the atmospheric CO_2 concentration from 390 parts per million by volume (ppmv) to approximately 1000 ppmv by the end of this century[1]. This means the human species and global ecosystems will be placed in a climate state never before experienced in their evolutionary history. Moreover, the combination of declining fossil fuel resources and our dependence on it will have major economic and political consequences.

With the energy consumption predicted in 2050 as 28 Terawatt-years (TWy), compared to 16 TWy in 2009[2], it is clear that research for alternative energy sources is of utmost importance. In 2012, non-renewable energy sources - including nuclear energy - accounted for more than 90 % of the global power production[3]. Among renewable and clean energy sources, solar energy has by far the most potential[4]. Capturing the energy of one hour of sunlight would be sufficient to meet our current yearly power demand.

While the sun provides an inexhaustible, clean energy source, the technology to capture this and convert to electricity - referred to as photovoltaics - has yet to reach its full potential. A global shift in fossil fuels to solar energy requires the latter to compete in terms of price, which is a result of both the efficiency and cost

to fabricate the photovoltaic device.

1.2 Photovoltaic concepts and materials

A photovoltaic device converts sunlight directly to electricity. Typically, the fundamental material is a semiconductor, which can absorb photons from the solar spectrum, creating charge carriers which are lead to an external circuit guided by the architecture of the device. At a temperature of absolute zero Kelvin, a semiconductor consists of completely filled valence bands and completely empty conduction bands. The energy difference between these bands is given by the band gap E_g. When the semiconductor is illuminated, photons with an energy of E_g or higher are absorbed and electrons are promoted from the valence to the conduction bands. These excited electrons are allowed to move freely trough the semiconductor, and leave behind positively charged holes. In an isolated semiconductor, electrons and holes will recombine and the material will return to its original state. In a solar cell, one attempts to separate the excited electron-hole pairs and allow current to be extracted from the device. This is realized by employing two semiconductor layers: a p-type layer, where there is an excess of hole type carriers, and an n-type, which holds an excess of electrons at thermal equilibrium.

Contacting these two layers creates a diode structure. Near the contact, electrons from the n-type side will diffuse to the p-type side, leaving behind positively charged ions. Similarly, holes from the p-type side move to the n-type side, leaving behind ions with a negative charge. This results in the formation of *space charge region* or *depletion layer*, which creates an electric field that counteracts the diffusion process for both electrons and holes. This leads to a situation where the dimensions of the depletion layer reaches an equilibrium. By the contact between the different layers, a potential difference or *build-in voltage* is created, which acts as a force to separate excited electron-hole pairs formed by illumination near the depletion layer. Excited electrons will move to the n-type side, while holes will move to the p-type side. By contacting both layers, and connecting the electrodes to an external load, the excited electron can now travel trough the wire, power the load and continue to recombine with a hole in the p-type side.

Currently, the dominant technology for solar cells is based on

crystalline Si wafers[5]. Si can be doped by boron or phosphorous to achieve p-type and n-type properties, respectively. This technology is mature and achieves module efficiencies of 14-21 %, with respectable energy payback times. Although Si is an abundant element, the process to obtain solar grade Si is energy intensive. Moreover, relatively thick Si layers are required (in the range of hundreds of micrometers), owing to the indirect band gap of Si.

A second generation of solar cells are called thin film devices. Here, alternative semiconductors are used with a direct band gap and consequently high absorption coefficients, making relatively thin layers sufficient (in the range of micrometers) to capture the solar spectrum[6]. CdTe and Cu(In,Ga)(S,Se)$_2$ (CIGS) PV modules are the dominating thin film technologies[7,8], with cell efficiencies up to 20 %, making them competitive with Si technology. In this work, we focus on the CIGS absorber layer. The main reason that large-scale application of this type of thin film device is not realized yet, is that the production cost of a CIGS solar cell is not yet substantially lower compared to Si solar cells[9]. The prevalent fabrication technique of CIGS absorber layers is co-evaporation - a vacuum-based process to evaporate copper, indium and gallium onto a substrate followed by or during selenization. Selenization refers to the thermal annealing in a Se-rich atmosphere. Achieving similar solar cell results with an alternative, non-vacuum based process would imply a considerable cost reduction and the possible breakthrough of CIGS solar cells[10].

1.3 CIGS structural properties

CIGS belongs to the family of I-III-VI$_2$ semiconductors and its crystal structure is named after the mineral chalcopyrite ($CuFeS_2$). This structure can be derived from the diamond structure according to the Grimm-Sommerfeld-rule, stating that a tetragonal structure is formed if the average number of valence electrons per atom in the compound equals 4 (other examples include Si, CdSe and GaAs). CIGS features a high optical absorption coefficient ($\alpha = 10^5\,\mathrm{cm}^{-1}$) and tuning of the band gap by composition over a large range (from 1.04 eV for $CuInSe_2$ up to 2.40 eV for $CuGaS_2$)[12]. The chalcopyrite structure follows a zincblende (*e.g.* ZnS) structure in which half of the cations are replaced by Cu, and the other half by In[11–13]. Consequently, each Cu and In/Ga atom is surrounded

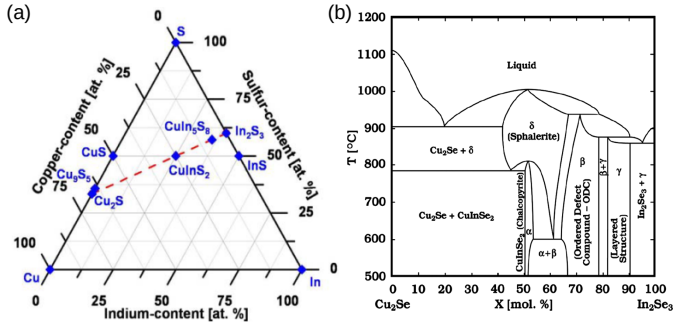

Figure 1.1: (a) Gibbs phase triangle for the Cu-In-S system at room temperature and atmospheric pressure [11]. Phase diagram along the pseudobinary section of the Cu-In-Se system [12].α = chalcopyrite-$CuInSe_2$; δ = sphalerite-$CuInSe_2$; β = Ordered defect compound-$CuIn_3Se_5$; γ = layered structure - $CuIn_5Se_8$.

by 4 S/Se atoms. Compared to zincblende, the lattice is slightly distorted due to different cations occupying the cation sites, as a result of different bond lengths between Cu-S/Se and In/Ga-S/Se.

In the context of this work, the phase relations in the CIGS system are relevant. Both during the synthesis of colloidal nanocrystals and the transformation of a precursor thin film to a dense CIGS absorber layer, it is worthwhile to examine the phase diagrams of these materials. Depending on the stoichiometry, temperature and pressure different compounds are predicted to be synthesized. In Figure 1.1a, a Gibbs phase triangle is presented for the Cu-In-S system at standard ambient temperature and pressure. Depending on the stoichiometry, a number of compounds are highlighted. Here, one finds the chalcopyrite $CuInS_2$ along the line connecting the Cu_2S and In_2S_3 binary compounds. Figure 1.1b shows a phase diagram as a function of composition and temperature for the pseudobinary section of the Cu-In-Se system. It should be noted that phase diagrams for Cu-In-S and Cu-In-Se are very similar [12]. The phase relations learn us is that In-rich $CuInSe_2$ will tend to form In-rich ternary phases, while a Cu-rich stoichiometry will result in the formation of chalcopyrite $CuInSe_2$ and a binary Cu_2Se phase. Due to the metallic character of the Cu_2Se compound, an overall Cu-rich stoichiometry is usually avoided [14]. High efficiency CIGS solar cells are overall Cu-poor, with a Cu/III ratio between 0.8-0.9. [8,15].

1.4 Solution processing of CIGS

Non-vacuum processes, or solution-based processing of semiconductors requires an ink in which precursors are dissolved. Precursors are molecules, salts or nanoparticles that contain the elements of the targeted compound[16,17]. A good solubility of the precursor is required not only for a homogeneous deposition of the wet thin film, but also for a good drying behaviour of the wet film. In all cases, the as-deposited *building blocks* need to go trough a process of phase formation, densification and/or sintering. This procedure of solution-based deposition towards polycrystalline CIGS absorber layers is schematically shown in Figure 1.2. Each stage of this practice provides challenges: the synthesis of the precursor, the formulation of the ink, the deposition of crack-free layers and the transformation towards the targeted compound.

The evaluation of a certain solution-based approach (categorized in molecular and particulate approaches) is often accomplished by the presentation of the solar cell efficiency of a (single) lab-scale device[16,18]. This makes it often difficult to determine the true effectiveness of that approach, as for example the practice of finishing the device differs from one group to another. Nevertheless, as this is the tendency in literature, we highlight a number of procedures that gained significant attention. Panthani *et al*[19] is recognized as the first author to report a reliable synthesis to produce phase-pure ternary and quaternary CIGS nanocrystals, showing a 0.24 % device by simply drop casting as-synthesized $CuInSe_2$ NCs without any post-treatment. Shown by Guo *et al*[20], annealing and selenization of $CuInSe_2$ NCs leads to a device efficiency of 2.82 %. The same group switched to $CuInS_2$ NCs, where they present that exchange of sulfur for selenium during the selenization clearly has a beneficial effect on the grain growth during the thermal treatment. This approach has lead to an efficiency of 4.76 %[21], which they later fine-tuned to achieve 12.0 % mainly by ink formulation (adjusting concentration, solvents and deposition) and NaCl soaking[22]. Using a molecular approach, the most successful solution-based CIGS devices were reported up to date[23,24], reaching 15.2 %. The major issue with the latter is the use of highly explosive and toxic (pure) hydrazine as a solvent and reducing agent. This hints at the Achilles' heel of solution-based approaches: the incorporation of impurities from solvents/ligands/stabilizers, as hydrazine is a perfect solvent in this respect. This conclusion

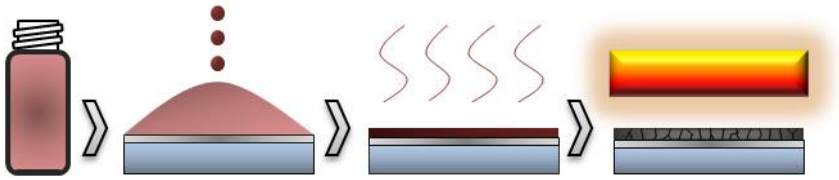

Figure 1.2: Process flow of a solution to a dense polycrystalline absorber.

is supported by reported approaches employing Cu/In salts with added stabilizers[25–27], which leaves a substantial amount of impurities after selenization, with a resulting efficiency of 5 %.

In this work, our contributions towards the goal of solution-based processing of CIGS are summarized. We mainly focus on colloidal nanocrystals as precursors. We characterize these nanocrystals and provide solutions to optimize the synthesis, surface chemistry and transformation behaviour. We also emphasize the use of solvents and ligands that should result in complete decomposition or evaporation upon annealing in order to minimize leftover impurities in the CIGS absorber. Moreover, as we will show in this work, several contributions can be applied to other applications for colloidal nanocrystals as well.

1.5 Outline of the thesis

This work is divided in three parts:

In the first part, which covers chapters II to IV, we discuss the synthesis of solution-based precursors, with a focus on binary and ternary nanocrystal materials of the $CuIn(S,Se)_2$ material family. Our aim is to understand the synthesis of these colloidal materials to pursue improvements to the reaction speed, yield and final products. We present novel synthesis strategies and extract useful information of the reaction development by monitoring the stoichiometry and yield during the nanocrystal synthesis. Next to colloidal nanocrystals, we investigate metal dithiocarbamates and selenium nanoparticles and show that these compounds are interesting additions to the precursor library.

The second part (chapters V and VI) provides an extensive analysis on the interesting yet unexplored surface chemistry of

our colloidal nanocrystals. With a focus on $CuInS_2$ nanocrystals - interesting as both precursor for $CuInSe_2$ absorber layers and as alternative for conventional quantum dots -, we classify the ligand chemistry in the framework of the covalent bond classification method. By employing Nuclear Magnetic Resonance spectroscopy (NMR), we demonstrate the first example of tightly bound L-type ligands on as-synthesized colloidal nanocrystals and discuss the implications for ligand exchange processes. Besides organic ligands, we consider inorganic ligands as a key to reduce the amount of organics present during transformation of nanocrystal precursors and to provide an excess of chalcogen species.

In the last part (chapters VII-IX), the focus lies on the transformation of our precursors towards dense $CuInSe_2$ absorber layers. We examine the differences in reactivity and sintering during thermal annealing/selenization to provide optimized combinations of nanocrystal precursors. We reveal a strong link between the surface chemistry and the annealing behaviour of colloidal nanocrystals, with a broad analysis on nanocrystals stabilized by inorganic sulfide ligands. The option of employing an excess of selenium included in the precursor ink is investigated to circumvent the need for gas-phase selenization. Moreover, we demonstrate the potential of the obtained $CuInSe_2$ absorber layer in thin film solar cells.

Bibliography

[1] Kiehl, J. Climate change. Lessons from Earth's past. *Science* **2011**, *331*, 158–9.

[2] Armor, J. N. Key questions, approaches, and challenges to energy today. *Catalysis Today* **2014**, *236*, 171–181.

[3] Agency, I. E. *Key World Energy Statistics*; Technical Report, 2013; pp 17–44.

[4] *Global Energy Assessment - Toward a Sustainable Future*; Johansson, T. B., Nakicenovic, N., Patwardhan, A., Gomez-Echeverri, L., Eds.; Cambridge University Press: Cambridge, 2012.

[5] Razykov, T.; Ferekides, C.; Morel, D.; Stefanakos, E.; Ullal, H.; Upadhyaya, H. Solar photovoltaic electricity: Current status and future prospects. *Solar Energy* **2011**, *85*, 1580–1608.

[6] Bosio, a.; Romeo, A.; Menossi, D.; Mazzamuto, S.; Romeo, N. The second-generation of CdTe and $CuInGaSe_2$ thin film PV modules. *Crystal Research and Technology* **2011**, *46*, 857–864.

[7] Green, M.; Emery, K. Solar cell efficiency tables (version 39). *Progress in Photovoltaics: Research and Applications* **2012**, *22*, 701–710.

[8] Jackson, P.; Hariskos, D. New world record efficiency for $Cu(In,Ga)Se_2$ thin-film solar cells beyond 20%. *Progress in Photovoltaics: Research and Applications* **2011**, *19*, 894–897.

[9] Jager-Waldau, A. Progress in chalcopyrite compound semiconductor research for photovoltaic applications and transfer of results into actual solar cell production. *Solar Energy Materials and Solar Cells* **2011**, *95*, 1509–1517.

[10] Azimi, H.; Hou, Y.; Brabec, C. J. Towards low-cost, environmentally friendly printed chalcopyrite and kesterite solar cells. *Energy & Environmental Science* **2014**, *7*, 1829.

[11] Camus, C. Ph.D. thesis, Hahn-Meitner-Institut Berlin, 2008.

[12] Anderson, T. J.; Stanbery, B. J. *Processing of $CuInSe_2$ - Based Solar Cells: Characterization of Deposition Processes in Terms of Chemical Reaction Analyses, Final Report*; Technical Report, 2011.

[13] Binsma, J.; Giling, L.; Bloem, J. Phase relations in the system

Cu_2S-In_2S_3. *Journal of Crystal Growth* **1980**, *50*, 429–436.

[14] Hsieh, T.-P.; Chuang, C.-C.; Wu, C.-S.; Chang, J.-C.; Guo, J.-W.; Chen, W.-C. Effects of residual copper selenide on $CuInGaSe_2$ solar cells. *Solid-State Electronics* **2011**, *56*, 175–178.

[15] Repins, I.; Contreras, M. A.; Egaas, B.; DeHart, C.; Scharf, J.; Perkins, C. L.; To, B.; Noufi, R. 19.9%-efficient $ZnO/CdS/CuInGaSe_2$ solar cell with 81.2% fill factor. *Progress in Photovoltaics: Research and Applications* **2008**, *16*, 235–239.

[16] Hibberd, C. J.; Chassaing, E.; Liu, W.; Mitzi, D. B.; Lincot, D.; Tiwari, a. N. Non-vacuum methods for formation of Cu(In, Ga)$(Se, S)_2$ thin film photovoltaic absorbers. *Progress in Photovoltaics: Research and Applications* **2010**, *18*, 434–452.

[17] Todorov, T.; Mitzi, D. B. Direct Liquid Coating of Chalcopyrite Light-Absorbing Layers for Photovoltaic Devices. *European Journal of Inorganic Chemistry* **2010**, *2010*, 17–28.

[18] Lee, D.; Yong, K. Non-vacuum deposition of CIGS absorber films for low-cost thin film solar cells. *Korean Journal of Chemical Engineering* **2013**, *30*, 1347–1358.

[19] Panthani, M. G.; Akhavan, V.; Goodfellow, B.; Schmidtke, J. P.; Dunn, L.; Dodabalapur, A.; Barbara, P. F.; Korgel, B. A. Synthesis of $CuInS_2$, $CuInSe_2$, and $Cu(In_xGa_{1-x})Se_2$ (CIGS), Nanocrystal Inks for Printable Photovoltaics. *Journal of American Chemical Society* **2008**, *2*, 16770–16777.

[20] Guo, Q.; Kim, S.; Kar, M.; Shafarman, W. Development of $CuInSe_2$ nanocrystal and nanoring inks for low-cost solar cells. *Nano letters* **2008**, *8*, 1–6.

[21] Guo, Q.; Ford, G. G. M.; Hillhouse, H. W. H.; Agrawal, R. Sulfide nanocrystal inks for dense $Cu(In_{1-x}Ga_x)(S_{1-y}Se_y)_2$ absorber films and their photovoltaic performance. *Nano letters* **2009**, *9*, 3060–5.

[22] Guo, Q.; Ford, G. Ink formulation and low temperature incorporation of sodium to yield 12% efficient Cu(In, Ga)$(S, Se)_2$ solar cells from sulfide nanocrystal inks. *Progress in Photovoltaics: Research and Applications* **2013**, *21*, 64–71.

[23] Liu, W.; Mitzi, D. B.; Yuan, M.; Kellock, A. J.; Chey, S. J.;

Gunawan, O. 12% Efficiency $CuIn(Se,S)_2$ Photovoltaic Device Prepared Using a Hydrazine Solution Process. *Chemistry of Materials* **2010**, *22*, 1010–1014.

[24] Todorov, T. K.; Gunawan, O.; Gokmen, T.; Mitzi, D. B. Solution-processed $Cu(In,Ga)(S,Se)_2$ absorber yielding a 15.2% efficient solar cell. *Progress in Photovoltaics: Research and Applications* **2012**, *21*, 82–87.

[25] Wang, W.; Su, Y.-W.; Chang, C.-h. Inkjet printed chalcopyrite $CuIn_xGa_{1-x}Se_2$ thin film solar cells. *Solar Energy Materials and Solar Cells* **2011**, *95*, 2616–2620.

[26] Lee, E.; Park, S. J.; Cho, J. W.; Gwak, J.; Oh, M.-K.; Min, B. K. Nearly carbon-free printable CIGS thin films for solar cell applications. *Solar Energy Materials and Solar Cells* **2011**, *95*, 2928–2932.

[27] Park, M.; Ahn, S. S.; Yun, J. H.; Gwak, J.; Cho, A.; Shin, K.; Nam, D.; Cheong, H.; Yoon, K. Characteristics of $Cu(In,Ga)Se_2$ (CIGS) thin films deposited by a direct solution coating process. *Journal of Alloys and Compounds* **2012**, *513*, 68–74.

Part 1: Solution synthesis of CIS materials

Introduction

The formation of sterically stabilized colloidal nanocrystals (NCs) from metalorganic complexes in reaction mixtures containing metalorganic precursors has seen a tremendous evolution over the last 20 years[1]. Introduced by Murray *et al*[2] and Brust *et al*[3] to make cadmium chalcogenide and gold nanocrystals, respectively, the approach was rapidly extended to the synthesis of nanocrystals of various metal, metal oxide and semiconductor materials[4]. Especially in the field of semiconducting nanocrystals, driven by their unique size and shape dependent opto-electronic properties, a considerable research effort has been put in optimizing the typical hot-injection synthesis with respect to size distribution, yield and upscaling[5–9]. This mostly concerns Cd and Pb chalcogenide nanocrystals, which can serve as model system for the currently emerging, environmentally friendly materials. Recently, I-III-VI_2 compounds such as $Cu(In,Ga)(S,Se)_2$ (CIGS in short) have gained interest in this perspective[10]. It has been shown that synthesis of ternary and quaternary materials is more complicated compared to the binary materials synthesized initially[11], due to the difference in precursor reactivity of the cations. Nevertheless, increasing efforts are made to improve the synthesis of CIGS NCs[12–15], mainly driven by their applications in, e.g, bioimaging[16–18], LEDs[19–21] and NC solar cells[22–24].

A different type of application of colloidal nanocrystals lies in the field of thin-film photovoltaics, where solution-based processing of CIGS absorber layers has attracted considerable attention[25,26]. The focus here lies on the formation of CIGS NCs to be used as a solution-based precursor for bulk thin films. The as-deposited NCs are subjected to a heat treatment with the goal to sinter the nanocrystals, densify the layer and remove organic contaminants. This approach has been demonstrated by Guo *et al*[27,28], where sulfide CIGS NCs were synthesized in the presence

of oleylamine and selenized in a reactive atmosphere at high selenium pressures to obtain bulk selenide CIGSe layers with large crystallite sizes. These layers were successfully incorporated into solar cells and yielded promising conversion efficiencies up to 12 %. However, these reports mainly focus on the transformation and properties of the final thin film, and does not seem to address relevant issues in the chemistry of the CIGS NC synthesis, such as reaction development, upscaling problems and chemical yield.

While ternary and quaternary NCs of the CIGS system received attention, reports on the use of binary NCs as precursor for CIGS layers are scarce[29]. Together with molecular precursors - which have also been used as solution-based precursors for CIGS[30–32] - they give rise to a so-called *hybrid ink*, which is interesting to compare with CIGS NCs with respect to reactivity in sintering/selenization. In this part, we systematically investigate the synthesis of ternary $CuInS_2$ and $CuInSe_2$ NCs, and the binary $Cu_xS(e)$ and $In_2S(e)_3$ constituents. We manage to improve the chemical yield and speed up the rate of the reaction by a careful choice of precursors and reaction conditions. Moreover, we investigate the stoichiometry and yield evolution during the synthesis of ternary NCs and compare them to their binary counterparts. Next to colloidal NCs, we focus on metal dithiocarbamates. We discuss their synthesis and transformation behaviour, demonstrating that they are interesting precursors for bulk sulfide thin films, and are due to their versatility promising additions to the library of CIGS precursors. Finally, we investigate the synthesis of selenium nanoparticles, with the intention of adding them to the precursor ink to circumvent the need for gas-phase selenization.

Chapter II

Synthesis of ternary and binary sulfide nanocrystals

2.1 $CuInS_2$ nanocrystals

2.1.1 Synthesis

For the synthesis of $CuInS_2$ nanocrystals (CIS NCs), we used the procedure developed by Panthani *et al*[23] as a starting point. Here, we changed the solvent from o-dichlorobenzene to 1-octadecene (ODE), and changed the hot-injection method to heating-up. This makes the reaction viable at higher temperatures - to investigate the effect of temperature - while using a cheaper and environmentally more friendly solvent. In a typical synthesis, 1 mmol $Cu(acac)_2$ (0.262 g) 1 mmol $In(acac)_3$(0.412 g) and 2.1 mmol (0.067 g) elemental S are combined in 15 mL of ODE using a three-neck flask. This flask is then attached to a Schlenk line, after which the heterogeneous mixture is flushed with nitrogen for 1 h. Next, 2 mL oleylamine (OLAm) is injected, followed by increasing the temperature to 180 °C. During the heating period, the precursors dissolve forming a brown mixture, followed by a color change to green and finally black. Upon reaching 180 °C, the reaction is allowed to continue for 1 h. After this period, the flask is cooled down using a water bath, and the CIS NCs are washed using toluene and ethanol. The NCs are then collected by centrifugation and the brown-red supernatant is discarded. The NC pellet is redissolved in toluene and the resulting clear black solution is stored in the fridge.

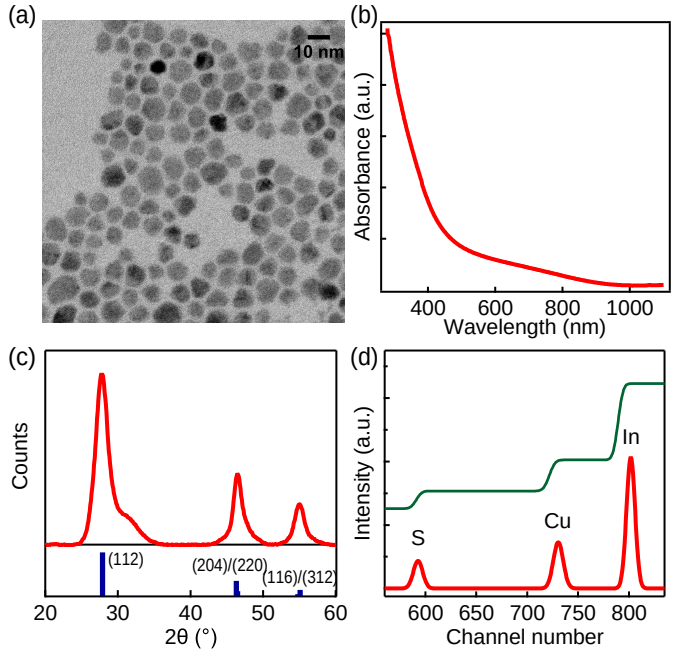

Figure 2.1: Characterization of as-synthesized CIS NCs. (a) TEM micrograph. (b) UV-Vis spectrum of a NC solution in chloroform. (c) XRD pattern of a NC thin film. The expected reflections of chalcopyrite $CuInS_2$ are shown as blue bars. (d) (red) RBS spectrum and (green) integrated backscattering intensities of a CIS NC thin film spincoated on a MgO substrate.

The procedure described above is the backbone of the CIS NC synthesis. We managed to improve the properties of the synthesis and the nanocrystals thus formed in terms of reaction yield, stoichiometry and size by changing the reaction temperature, the heating rate and the concentration of precursors/ligands. These results are presented in the characterization section.

2.1.2 Characterization

Using the synthesis procedure as described above, we obtain CIS NCs of which the basic properties follow from characterization results as summarized in Figure 2.1. Figure 2.1a shows a representative TEM micrograph of the as-synthesized CIS NCs. The NCs appear as quasi-spherical with a mean diameter of ≈8 nm and a size dispersion of ≈15 %. According to the XRD pattern, chal-

copyrite $CuInS_2$ NCs are obtained with no observable secondary phases present, while the UV-Vis absorption spectrum (Figure 2.1b) shows an absorption onset around the band gap of bulk CIS (1.54 eV). The Rutherford Backscattering Spectrum shown in Figure 2.1d is used to calculate the stoichiometry of the CIS NCs. Here, we use the integration of the signals obtained for S, Cu and In nuclei by taking the Z^2 dependency into account. This yields a Cu:In ratio of 1.23±0.10 and a S:In ratio of 1.54±0.18. This results in a ratio between the formal charge on the metal cations (Cu^+ and In^{3+}) and the sulfide anions (S^{2-}) of 1.50±0.14. In other words, the as-synthesized CIS NCs are cation rich, and contain more copper than indium.

When working with colloidal NCs, an essential unit to determine is the amount of nanocrystal material or the concentration of nanocrystals in solution. Since our CIS NCs exceed the exciton Bohr radius for $CuInS_2$ [10], their absorption spectrum should correspond to the expected for spherical CIS nanocrystals with the optical properties of bulk CIS. We can conveniently derive the NC concentration using UV-Vis absorption spectroscopy, by measuring the absorbance A, which is determined by the length ℓ of the cuvette, the volume fraction f of the NCs – which is the ratio between the volume of all nanocrystals and the volume of the nanocrystal dispersion – and the intrinsic absorption coefficient μ_i of the NCs (Lambert-beer).

$$A = \frac{f\ell\mu_i}{\ln(10)} \tag{2.1}$$

The intrinsic absorption coefficient is determined by the optical constants n and k of the material, the refractive index of the solvent n_s, the observation wavelength λ and the local field factor f_{LF}. This factor is defined as the ratio between the light intensity inside the NCs and in the medium around the NCs [33]. For spherical particles the following relations are used [34]:

$$|f_{LF}|^2 = \frac{9n_s^4}{(n^2 - k^2 + 2n_s^2)^2 + 4(nk)^2} \tag{2.2}$$

$$\mu_i = \frac{2\pi}{n_s\lambda}|f_{LF}|^2 2nk \tag{2.3}$$

After the calculation of μ_i, using the optical constants derived from bulk $CuInS_2$ [35], the volume fraction f is calculated using

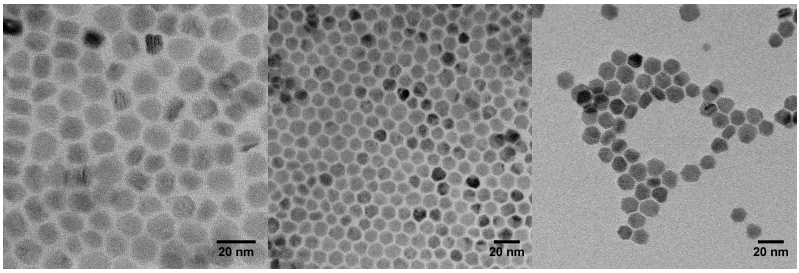

Figure 2.2: CIS NCs obtained by modifying the synthesis temperature. (a) 210 °C (b) 240 °C (c) 270 °C.

equation 2.1. This allows us to determine the amount of material in solution n using the molar volume V_m, the density ρ of CIS and the sample volume V.

$$V_m = \frac{M}{\rho} \tag{2.4}$$

$$n = \frac{fV}{V_m} \tag{2.5}$$

The above equations enable us to measure the concentration of CIS in solution and the chemical yield of the synthesis. For the synthesis procedure described above, we typically come to a yield of 70%.

In many cases, it is not so much the volume fraction of nanocrystal materials that is of interest - for instance to determine the ligand density (See chapter V) - yet the nanocrystal concentration. This can be calculated from the volume fraction when the volume of a single nanocrystal is known or, alternatively, equation 2.1 can be rewritten in terms of the molar extinction coefficient ϵ of the nanocrystals. For spherical particles, ϵ can be determined from the intrinsic absorption coefficient according to:

$$\epsilon = \frac{N_a d^3 \mu_{intr} \pi}{6 \ln 10} \tag{2.6}$$

Using ϵ, the nanocrystal concentration c is then calculated from the Lambert-Beer law expressed as:

$$A = \epsilon c \ell \tag{2.7}$$

As mentioned before, CIS NCs obtained by the modified procedure of Panthani *et al* are cation rich and the reaction has a

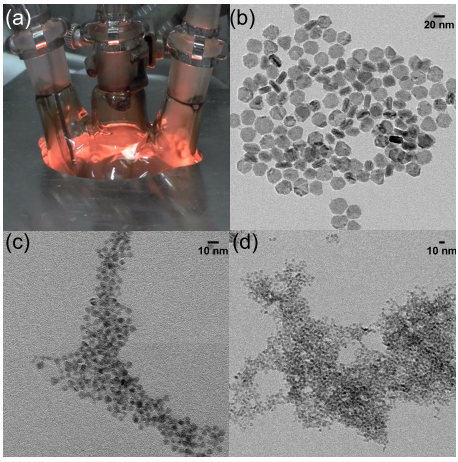

Figure 2.3: (a) Infrared heating lamp setup used to control heating rates. (b), (c) and (d)$CuInS_2$ NCs obtained at different combinations of OLAm and ODE amounts.

chemical yield of 70 %. To further optimize this procedure, we increased the reaction temperature from 180 °C to 210 °C, 240 °C and 270 °C, while keeping the other parameters constant. The resulting CIS NCs are shown in Figure 2.2a-c. We observe that the mean particle size increases slightly at higher temperature (from ≈10 nm to ≈11 nm to ≈12 nm), and the shape evolves from quasi-spherical to hexagonal prisms, or *tiles*. Importantly, we calculated a higher chemical yield compared to the synthesis at 180 °C. At 210 °C, 83 % is obtained, while at 240 °C, this rises to 91 %. Performing synthesis at higher temperatures is not advised because the boiling point of the solvent is approached. This makes the yield calculation unreliable. Nevertheless, the resulting NCs are still characterized by TEM (Fig 2.2c), exhibiting a tile shape comparable to the NCs synthesized at 240 °C.

2.1.3 Size and shape tuning

As briefly mentioned in Chapter I, important elements in synthesizing NCs as precursor for dense layers are the reaction yield and nanocrystal morphology, whereas polydispersity is less of a concern since the nanocrystals will be sintered during the heat treatment. Having access to different sizes and shapes of CIS NCs, however, is an advantage, since we hypothesize that combinations of rela-

tively large and small NCs provides better packing in a NC layer. With the highest yield obtained at 240 °C, we tested the influence of concentration and relative amounts of coordinating versus non-coordinating solvents. An infrared heating lamp was used to gain increased control over the heating rate and access higher heating rates compared to a conventional heating mantle (Figure 2.3a). At a set heating rate of 80 °C/min, we obtained different CIS NCs sizes and shapes after a total reaction time of 1 h. Using 1 mmol $Cu(acac)_2$, 1 mmol $In(acac)_3$ and 2.1 mmol elemental S, we obtained relatively large tile shaped CIS NCs using 2 mL OLAm and 30 mL ODE as shown in Figure 2.3b. This corresponds to a concentration of precursors halve that of the standard CIS NCs synthesis at 240 °C. In Figure 2.3b, CIS NCs are shown when the amount of OLAm is set to 8 mL and ODE to 8 mL in the synthesis. Here, small quasi-spherical CIS NCs are obtained. Roughly the same size and shape is obtained when 16 mL OLAm and 16 mL ODE is used. The relation between the synthesis parameters and the NC output is complex, especially in these ternary systems. It is not the scope of this work to provide a clear explanation in this respect. The final size, composition, shape and yield of a NC synthesis is governed by many parameters which are linked. We conclude that the concentration of precursors and coordinating solvent has a large influence on the morphology of CIS NCs, and these parameters could be further optimized to achieve different sizes and shapes.

2.1.4 Synthesis development

To get insight in the reaction pathway leading to the formation of ternary CIS NCs, we followed the optimized procedure involving heating to 240 °C as a function of time and temperature by taking quantitative aliquots. In Figure 2.4, the UV-Vis-NIR absorbance spectra of these aliquots are shown, together with the spectrum of the purified reaction product, taken at the intervals indicated in the figure. Here, the $t = 0$ s is chosen as the moment where the reaction temperature reaches 130 °C mark, since the reaction mixture contains undissolved precursors before reaching this temperature. We notice that at the start of the reaction, the spectrum is dominated by an intense NIR band, which shifts and gradually disappears throughout the heating period. This NIR band is attributed to a plasmon resonance, typical for Cu_xS species[36], which

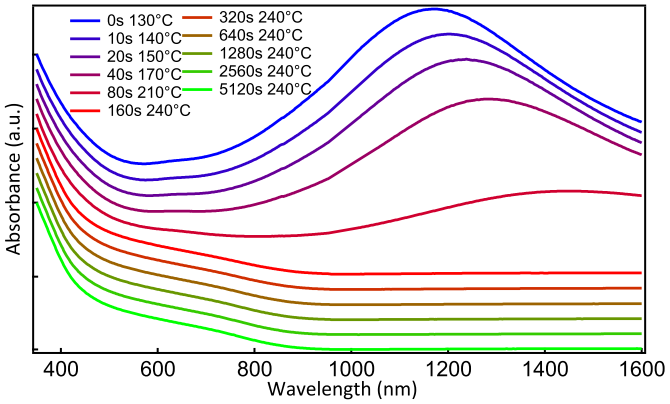

Figure 2.4: UV-Vis-NIR absorbance spectra taken at different time intervals during the heating-up synthesis of CIS NCs.

have a considerable density of free charge carriers due to their cation deficiency. Upon reaching 240 °C the NIR band disappears, and the spectra for subsequent aliquots show little differences.

We further investigated the evolution of the reaction using elemental analysis by means of X-ray Fluorescence (XRF). We made a series of standard samples, in the same range of concentration as the supernatant and the particles solutions using nitrate salts. The X-ray fluorescence intensities of these have been used to make a calibration curve and subsequently determine the concentration of the elements in the samples. By precipitating the reaction aliquots and redispersing them in a known amount of toluene, we were able to differentiate between cations present in the NCs formed, and cations present as precursor complexes. Figure 2.5a shows that the amount of Cu in the CIS NCs stays put at 1 mmol, which is the starting amount of both Cu and In in this reaction, throughout the reaction. In contrast, In is gradually incorporated in the nanocrystals during the first 3 min of the synthesis.

The quantitative analysis of the nanocrystals is in line with the change in composition of the supernatant, as these show the opposite trend. Here, no Cu precursors are present throughout the reaction, while In gradually decreases in the first minutes. To analyze possible changes in the NC morphology, we have selected purified aliquots taken at the start of the reaction (Fig 2.5b), after 3 min (Fig 2.5c) and after prolonged heating at 240 °C (Fig 2.5d). We noticed no significant changes in size and shape of the obtained

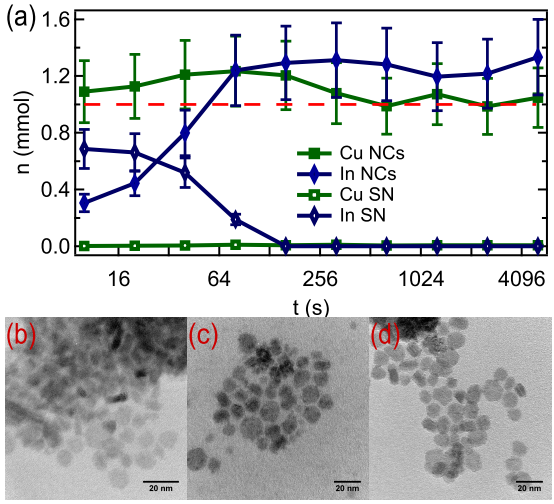

Figure 2.5: (a) Time development of the amount of Cu (green dots) and In (blue dots) in the precipitate - denoted as NC - and the amount of Cu (green squares) and In (blue squares) in the supernatant - denoted as SN - as a function of reaction time. TEM micrographs takes of the purified aliquots at (b) start of the reaction (c) 3 min and (d) 85 min.

CIS NCs at different times.

The analysis of the reaction aliqouts brings us to a general picture of the reaction pathway. During the heating period, Cu_xS and/or Cu-rich $CuInS_2$ nanocrystals are formed first. At our arbitrary choice of the start of the reaction - when no undissolved species were present - all Cu precursors are already incorporated into NCs, whereas little In is. When the temperature increases, In is gradually incorporated in the existing NCs, which serve as templates for the final, stoichiometric CIS NCs. Stoichiometric CIS NCs are obtained as soon as the temperature reaches 240 °C, or after 3 min at a heating rate of 40 °C/min used in the XRF analysis. This is supported by the RBS measurements of CIS NCs obtained by prolonged heating at 180 °C, where CIS NCs are rich in Cu compared to In. Further heating at 240 °C does not seem to influence the stoichiometry, yield and morphology of the CIS NCs. This implies that total reaction time in our optimized procedure can be relatively short compared to literature procedures; a matter of minutes depending on the heating rate compared to hours[10].

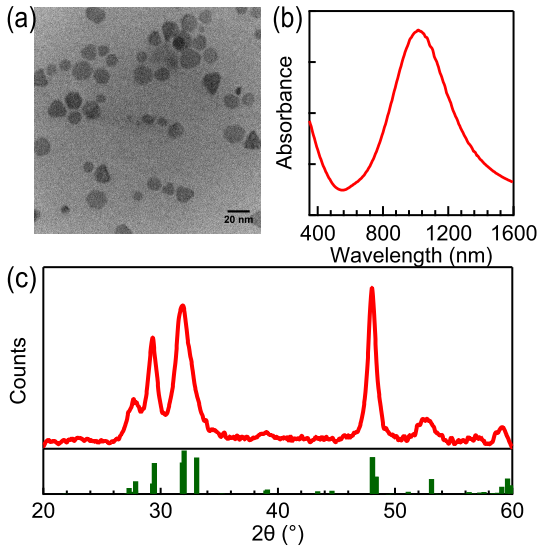

Figure 2.6: Characterization of as-synthesized CuS NCs. (a) TEM micrograph. (b) UV-VIS-NIR absorption spectrum of a CuS NC solution in C_2Cl_4. (c) XRD pattern of a dried CuS NC thin film (red) and expected reflections of covellite CuS (green bars).

2.2 CuS nanocrystals

2.2.1 Synthesis

To synthesize CuS NCs, 3 mmol $Cu(acac)_2$ (0.786 g) is flushed with nitrogen together with 3.05 mmol S (0.0978 g) in 20 mL of ODE at room temperature. After 1 h, 10 mL of OLAm is injected and the reaction mixture is heated to 130 °C. When the flask arrives at 130 °C, the reaction mixture is dark green. After 1 h, the flask is cooled down to room temperature using a water bath. Then, the CuS NCs are collected using toluene and precipitated using ethanol. Following centrifugation, the brown red supernatant is discarded while the NCs are dispersed using toluene.

2.2.2 Characterization

Figure 2.6a shows a TEM image of the purified reaction product. We observe polydisperse CuS NCs with a mean diameter around 10 nm. The most prevalent feature in the UV-VIS-NIR absorption spectrum in Figure 2.6b is the appearance of a large NIR

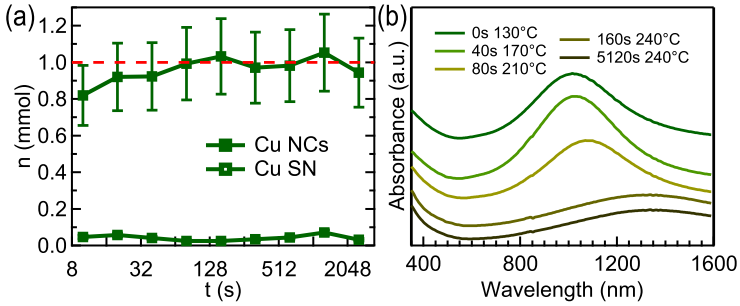

Figure 2.7: Monitoring of a heating-up CuS synthesis with a target temperature of 240 °C.(a) Time development of the amount of Cu in the CuS NCs (dots) and Cu in the supernatant (squares). (b) UV-VIS-NIR absorption spectra taken at different intervals in the synthesis.

band, which is typical for $Cu_{2-x}S$ NC species with x close to 1[37]. This stoichiometry is confirmed by the diffraction pattern in Figure 2.6c, where the measurement closely resembles the expected reflections for CuS.

In order to compare the CuS NCs synthesis with the monitoring results gathered in the CIS NC synthesis, we repeated this reaction using the same temperature profile as in 2.1.4. Here, quantitative aliquots were collected and purified at similar reaction times. In Figure 2.7a, the evolution of the yield of the synthesis is shown, as measured by XRF. We can see that throughout the reaction, full yield is obtained (normalized by the amount of Cu used for the synthesis). This is supported by the negligible amount of unreacted Cu found in the supernatant. While all Cu is consumed at the start of the reaction, we observe a color shift from green to brown at higher temperatures. This is confirmed by the UV-VIS-NIR measurement in Figure 2.7b, where a selected amount of aliquots are shown. It appears that the large NIR band shifts to longer wavelengths, while gradually decreasing in intensity. This is an indication that the CuS NCs formed at the start of the reaction, gradually transform to Cu-rich $Cu_{2-x}S$ species ($0 < x < 1$) by reduction, as the free carrier density decreases in the nanocrystals during that process[37,38]. This has both an effect on the plasmon frequency and the extinction coefficient at that frequency. For perfect, non oxidized Cu_2S NCs, such a plasmon resonance would not exist. Our synthesis of CuS NCs thus allows

to tune the stoichiometry by reaction temperature and time.

2.3 In_2S_3 nanocrystals

2.3.1 Synthesis

In a typical In_2S_3 NC synthesis, 2 mmol $InCl_3$ (0.465 g) is stirred and flushed with nitrogen after adding 8 mL ODE at 110 °C. Meanwhile, 3.65 mmol S (0.128 g) is dissolved in 6 mL ODE in a nitrogen-filled glovebox at 150 °C. After the injection of 4 mL OLAm in the flask with the In precursor and raising the temperature to 170 °C, 5 mL of the S-ODE solution is injected in this flask. The reaction is allowed to stir for 1 h at 170 °C, followed by cooling down to room temperature using a water bath. The In_2S_3 NCs are seperated by adding toluene and ethanol, and are redissolved in toluene. During the course of the reaction, quantitative aliquots were taken to analyse the evolution of the chemical yield.

2.3.2 Characterization

The TEM image in Figure 2.8a shows the morphology of the as-synthesized In_2S_3 NCs. It appears that the synthesis procedure described above leads to the formation of In_2S_3 nanosheets; thin flat objects of a few atomic layers thick with a top diameter around 20 nm. This preliminary conclusion is drawn by the observation of stacked nanocrystalline material in the TEM image, implying a very limited thickness. The UV-Vis absorption spectrum (Figure 2.8b) shows an absorption onset at around 500 nm, while the bulk band gap of In_2S_3 lies at longer wavelengths (600 nm). This quantum confinement effect can be understood by the dimensions of the NCs. The XRD pattern (Figure 2.8c) features both very broad and narrow peaks, typical for anisotropic particles such as nanosheets. Unlike the CuS NC synthesis in 2.2.2, the yield of the synthesis increases relatively slowly during course of the reaction, as shown in Figure 2.8d. We notice a slow increase of In in the NCs as a function of time, accompanied by a slow decrease of In in the supernatant after purification of the quantitative aliquots.

It has to be noted that the yield evolution in the synthesis of CuS NCs and In_2S_3 NCs concurs with the yield evolution in the CIS NC synthesis. It is concluded that, most likely due to a different reactivity of the precursor complexes, CuS NCs form

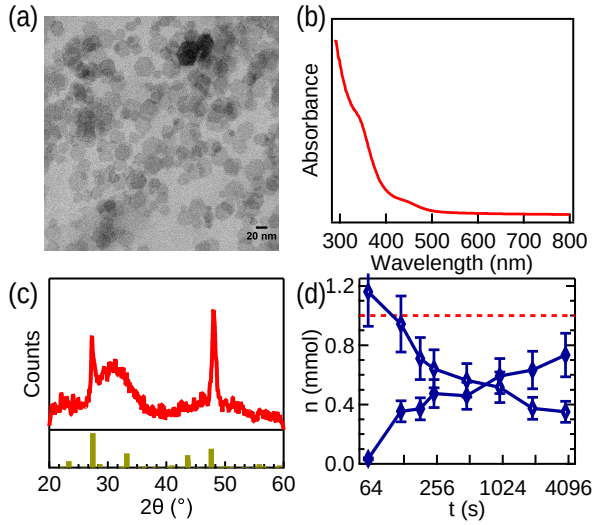

Figure 2.8: (a)TEM image of as-synthesized In_2S_3 NCs. (b) UV-VIS absorption spectrum of a In_2S_3 NC solution in $CHCl_3$. (c) XRD pattern of a dried In_2S_3 NC thin film (red) and expected reflections of In_2S_3 (brown bars). (d) Time development of the amount of In in NCs (blue dots) and in the supernatant (blue squares)

much faster than In_2S_3 NCs, and In is incorporated in the existing CuS NCs to produce CIS NCs.

2.4 Conclusions

$CuInS_2$, CuS and In_2S_3 NCs are successfully synthesized by mixing the cation salts (acetylacetonates for $CuInS_2$ and CuS NCs, $InCl_3$ for In_2S_3) with elemental sulfur in the presence of OLAm at elevated temperatures. Insight in the reaction pathway was obtained trough elemental analysis of reaction aliquots. Here, we notice that in the synthesis of CIS NCs, Cu_xS NCs are nucleated at the start of the reaction, consuming all Cu. This is followed by a gradual incorporation of In in the existing NCs. We managed to increase the reaction yield mainly by increasing the reaction temperature. At 180 °C, even at prolonged reaction times, the incorporation of In in CIS NCs is not complete leading to Cu-rich CIS NCs and a lower chemical yield. The observed pathway leading to stoichiometric, ternary CIS NCs was supported by the reaction analysis of

binary CuS and In_2S_3 in similar reaction conditions. We indeed observed a fast, complete reaction towards CuS NCs while In_2S_3 are found to nucleate/grow slower. By changing reaction parameters such as concentration of precursors and coordinating species, we managed to obtain CIS NCs with different sizes and shapes. Most notably, large CIS tiles were obtained at low precursor concentrations. Taking into account the application - deposition and sintering of the NCs - we did not provide a thorough investigation of the complex relation between the NC morphology and synthesis parameters. Both relatively small and large NCs offer advantages and disadvantages in this respect. For example, smaller NCs contain proportionally more ligands than larger NCs (which are ought to be removed/decomposed upon sintering), while they are more stable in solution. Most importantly, our optimized, heating-up procedure allows us to obtain CIS NCs at full yield within minutes after mixing the precursors.

Chapter III

Synthesis of ternary and binary selenide nanocrystals

On a line with sulfide nanocrystals of the CIGS materials family, selenides are interesting as both alternatives for conventional quantum dots[22,39] and precursors for dense CIGS thin films[40–42]. In this chapter we discuss the synthesis of $CuInSe_2$, $Cu_{2-x}Se$ and In_2Se_3 NCs with a focus on achieving fast and complete reactions. We emphasize the importance of the selenium precursor in this respect. The synthesis of metal selenide NCs in general suffers from a limited amount of selenium precursors, often making use of expensive and oxidation prone trioctylphosphine selenide, as is the case for $CuInSe_2$ NCs[16,43]. Here, we introduce the direct injection of Se powder - heterogeneously dispersed in a carrier solvent such as ODE - as an alternative precursor for the synthesis of colloidal metal selenide nanocrystals of the CIGS family. This has been shown to produce state-of-the-art CdSe and ZnSe NCs within a lower time frame and at full yield even without protective atmosphere compared to conventional Se precursors[44].

3.1 Reaction analysis

All nanocrystal syntheses have been executed as described in the respective sections. After synthesis, nanocrystal purification is achieved by standard precipitation methods using methanol or methanol/isopropanol mixtures as the non-solvent and toluene as the solvent. The quantitative analysis of the reaction development is based on the weight of the reaction mixture and of the different

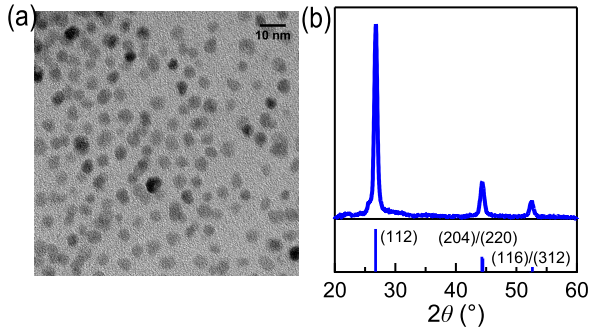

Figure 3.1: (a) TEM micrograph of $CuInSe_2$ nanocrystals formed by the injection of Se powder in a solution of $Cu(acac)_2$ and $In(acac)_3$ in oleylamine after 10 min of reaction time. Scale bar: 10 nm. (b) X-ray diffractogram of the CISe nanocrystals thus formed. The vertical lines indicate the most important reflections of chalcopyrite $CuInSe_2$.

aliquots taken. The amount of product formed in the aliquots is determined using X-ray fluorescence spectroscopy. The final reaction yield is obtained from the amount of unreacted precursors as determined using XRF in the supernatant after purification of the reaction product. For quantitative XRF analysis (Rigaku NEX CG), UltraCarry's® have been used to measure the liquid samples. A series of standard samples, in the same range of concentration as the supernatant and the particles solutions, have been made making use of chloride salts and selenious acid solutions. The X-ray fluorescence intensities have been used to make a calibration curve and subsequently determine the concentration of the elements in the samples. X-ray diffraction (XRD) measurements were carried out using a Thermo scientific ARL X'TRA model on dried dispersions dropcast on silica substrates. Transmission electron microscopy (TEM) micrographs were acquired using a Cs-corrected Jeol 2200 FS microscope.

3.2 $CuInSe_2$ nanocrystals

For the synthesis of $CuInSe_2$ (CISe) nanocrystals, we start from a mixture of $Cu(acac)_2$ (2 mmol) and $In(acac)_3$ (2 mmol) in oleylamine (OLAm) (16 mL). After flushing the mixture for 1 h with nitrogen at 110 °C, its temperature is raised to 240 °C, leading to

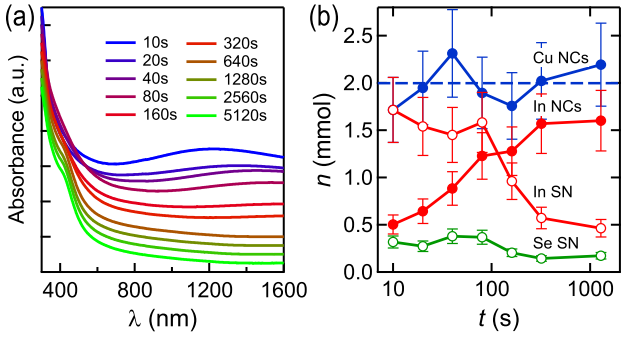

Figure 3.2: (a) Normalized absorption spectra of aliquots taken at the indicated time after the Se injection. The different spectra are offset for clarity. (b) Time development of the amount of (blue dots) Cu and (red dots) In in the precipitate - indicated as NC - and of (red circles) In and (green circles) Se in the supernatant - indicated as SN - after the second, size selective precipitation step of the respective aliquots.

a color change from blue to brown to brown-red at 240 °C. At this temperature, Se powder (4.1 mmol), heterogeneously dispersed in ODE (8 mL) is swiftly injected, after which the reaction mixture turns black immediately. . Figure 3.1a shows a TEM micrograph and an XRD diffractogram of the product collected when stopping the reaction after 10 min. Clearly, quasi-spherical nanocrystals with a mean diameter of about 7 nm are formed with a crystal structure that corresponds to that of chalcopyrite $CuInSe_2$ (Figure 3.1b).

A more detailed view on the reaction development follows from the analysis of aliquots, taken at different times after the Se injection. The UV-Vis absorption spectra of the aliquots taken in the first 5 min of the reaction clearly show the infrared absorption band characteristic of the plasmon resonance of Cu_xSe_y nanocrystals (see Figure 3.2a)[45]. From 10 min on, the infrared absorption is absent, and we notice no difference with subsequent absorbance spectra. In line with the TEM and XRD analyses, this indicates that the formation of CISe is finished at about 10 min. Further analysis of the aliquots using XRF provides more information on the synthesis development (Figure 3.2b). For these measurements, we first precipitated the quantitative aliquots. Since for all aliquots, the supernatant contained little Cu, In and Se, the precipitated powder was redispersed and subjected to a sec-

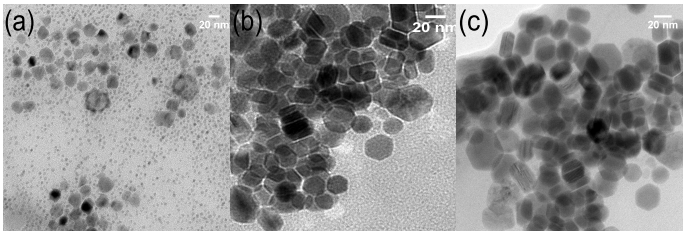

Figure 3.3: Evolution of CISe NC morphology as a function of reaction time. (a) 10 min. (b-c)90 min.

ond precipitation step using a minimum amount of non-solvent (so-called size selective precipitation). This is meant to precipitate larger nanocrystals (denoted as NCs in Figure 3.2b), leaving behind possible precursor complexes or small nanocrystals in the supernatant. Doing so, we find that the amount of Cu collected in the precipitate remains constant, equal to the 2 mmol of Cu used in the reaction. On the other hand, most of the In is initially recovered in the supernatant. Since the supernatant contains little Se and no Cu, this is most likely as an In complex, and not as small In_2Se_3 nanocrystals. During the first 5 minutes, the amount of In in the precipitate gradually increases, at the expense of the In in the supernatant. This points toward a gradual incorporation of In in the Cu_xSe_y nanocrystals, with a concomitant transformation of the initially formed Cu_xSe_y into CISe. In contrast to Kar *et al*[40] we cannot observe the formation of InSe species, as it would imply the Se which is not incorporated in the nanocrystals to follow the In signal, which is not the case.

Even though stoichiometric CISe NCs are formed after 10 min reaction time, we noticed a ripening phenomenon at longer reaction times. Already at 10 min, signs of relatively large CISe NCs are visible in the TEM sample (Figure 3.3a). Aliquots obtained later in the reaction reveal large polydisperse, tile-shaped CISe NCs, as shown in Figure 3.3b-c. We note that although the synthesis of $CuInS_2$ NCs (section 2.1.4) shows the same evolution in stoichiometry during the reaction, the ripening is absent in that case. In the synthesis of $CuInS_2$ NCs, the morphology of the NCs stays put as soon as all initial Cu is consumed, as the existing CuS NCs act as templates for stoichiometric CIS NCs after incorporation of In. A further comparison learns that In is incorporated slower in Cu_xSe_y.

In literature, $CuInSe_2$ NCs have been synthesized using a combination of metal salts and elemental selenium as precursors and OLAm as the ligand. All reagents are either mixed at low temperature, followed by a gradual heating of the reaction mixture[23,41] or selenium is dissolved prior to injection in OLAm by prolonged heating at elevated temperature[46]. In both approaches the reaction mixture is left at elevated temperatures for one to four hours. Although little is known about the yield or the yield development of these reactions, it indicates that this heating up results to a relatively slowly reacting Se precursor. The results shown here indicate that for the synthesis of $CuInSe_2$ NCs, state-of-the-art nanocrystals can be obtained by injecting selenium powder in the reaction mixture at elevated temperature using a carrier liquid. Opposite from heating up approaches or the injection of dissolved selenium species, this initiates a rapid and high yield conversion of the precursors into nanocrystals. The highly reactive selenium species resulting from the injection of selenium powder forms a Cu_xSe_y compound in which In is incorporated in a later stage of the reaction to form CISe. This Cu_xSe_y formation has been described before by Kar *et al*[40], who used a heating up procedure. However, in their case, the CuSe formation extends over a large part of the 1 hour heating up time, while upon injection of Se powder, we find that all CuSe is formed within the first 10-15 s of the reaction.

To explain the difference between our heterogeneous ODE-Se precursor compared to a homogeneous ODE-Se precursor, we refer to the paper of Flamee *et al*[44]. Here, the properties of CdSe NCs synthesized using both Se precursors are compared, and it is shown that state-of-the-art CdSe NCs are obtained using the heterogeneous ODE-Se precursor. Moreover, using this Se precursor, the reaction can be carried out without a protective atmosphere, and leads to a high yield within 5-10 min. Based on a study by Bullen *et al*[47], the lower reactivity of the homogeneous ODE-Se precursor is interpreted in terms of a vulcanization process where ODE molecules are first bridged by short Se chains and later on by single Se atoms. Using the reactive, heterogeneous Se precursor, it appears that the selenium species formed after the injection of Se powder is rather a dissolved Se compound that precedes these vulcanization reactions.

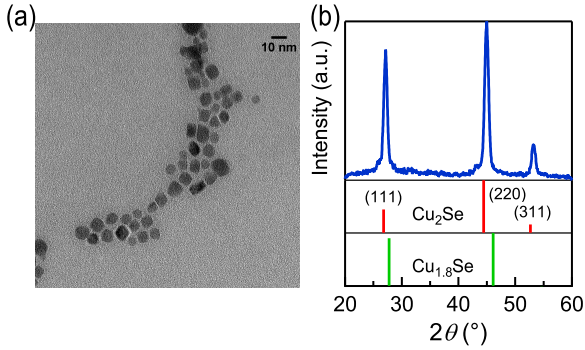

Figure 3.4: (a) TEM micrograph of $Cu_{2-x}Se$ nanocrystals formed by the injection of Se powder in a solution of $Cu(acac)_2$ in oleylamine after 1 hour of reaction time (see text). Scale bar: 10 nm. (b) X-ray diffractogram of the $Cu_{2-x}Se$ nanocrystals thus formed. The vertical lines indicate the most important reflections of chalcopyrite Cu_2Se and $Cu_{1.8}Se$ as a reference.

3.3 Cu_2Se nanocrystals

$Cu_{2-x}Se$ nanocrystals are obtained in a similar fashion as CISe nanocrystals. In this case, 2 mmol of $Cu(acac)_2$ is dissolved in 20 mL of OLAm. This mixture is flushed with nitrogen at 110 °C during 1 h, after which the temperature is increased to 200 °C to obtain a brown mixture. At this point, 1.5 mmol of Se dispersed in 1.5 mL of ODE is injected, leading to a color change to green-brown. The mixture is allowed to react at 200 °C for 30 min, after which the reaction is cooled down and the nanocrystals are separated using a similar procedure as shown above. TEM analysis of the reaction product (Figure 3.4) shows 8 nm nanocrystals with various shapes. In the XRD pattern, we can see that the reflections occur at angles in between those expected for Cu_2Se and $Cu_{1.8}Se$, indicating the formation of a Cu-rich $Cu_{2-x}Se$ phase (see Figure 3.4b). This stoichiometry is supported by SEM-EDX measurements, where a ratio of 62:38 Cu:Se is found. By chemical analysis of the supernatant after precipitating the nanocrystals, a chemical yield of 90-95 % is obtained.

Compared to literature, a very similar approach, based on the injection of selenium dissolved in OLAm, has been described for the synthesis of $Cu_{2-x}Se$ nanocrystals[45]. Although in this case, the reaction time was limited to 15 minutes, no information is

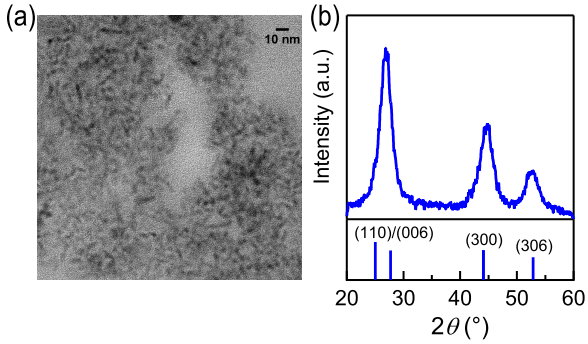

Figure 3.5: (a) TEM micrograph of In_2Se_3 nanocrystals formed by the injection of Se powder in a solution of $In(acac)_3$ in oleylamine after 1 hour of reaction time. Scale bar: 10 nm. (d) X-ray diffractogram of the In_2Se_3 nanocrystals thus formed. The vertical lines indicate the most important reflections of In_2Se_3 as a reference.

provided on the concomitant reaction yield.

3.4 In_2Se_3 nanocrystals

We follow a comparable approach to synthesize In_2Se_3 nanocrystals. Here, we start by dissolving 2 mmol $InCl_3$ in 20 mL of OLAm. This mixture is flushed with nitrogen at 110 °C for 1 h, after which the temperature is increased to 200 °C. At this point, Se powder (3.1 mmol) dispersed in 3 mL of ODE is injected in the reaction. The color of the mixture changes from yellow-red to dark red in the course of a minute. After leaving the reaction mixture at 200 °C for 1 h, the nanocrystals are collected by cooling down the synthesis and using standard centrifugation methods. The TEM micrograph in Figure 3.5a confirms the formation of nanocrystals with a size below 10 nm. The crystal structure obtained by measuring the XRD pattern confirms the presence of the In_2Se_3 phase (Figure 3.5). SEM-EDX measurements corroborate the stoichiometry as a 32:68 In:Se ratio is found. The yield of the reaction, using the same procedure as for $Cu_{2-x}Se$ nanocrystals, was calculated as 80-85 %.

Literature reports on colloidal In_2Se_3 NCs are scarce. It has been shown that prolonged heating of $InCl_3$ and elemental Se in OLA leads to cubic-phase InSe nanowires[48], whereas In-Se

nanosheets have been obtained using selenourea as a selenium precursor[49] and In_2Se_3 nanocrystallites have been obtained using solvothermal methods[50].

3.5 Conclusions

The combination of a fast and high yield reaction with low cost precursors make the approach to synthesize ternary and binary selenides of the CISe system proposed here well suited for larger scale NC synthesis. The synthesis is based on the hot injection of elemental selenium powder, heterogeneously dispersed in a carrier liquid, to a solution of cation precursors in OLAm. Compared to existing synthesis procedure that make use of elemental selenium, e.g., to form $CuInSe_2$ and $Cu_{2-x}Se$, this leads to a fast and close to full yield conversion of precursors into nanocrystals. In addition, the method can be extended to the formation of In_2Se_3 NCs - a material for which little or no low-cost routes have been described - which again results in a fast and close to full yield reaction. Based on these results, we conclude that the hot injection of selenium powder is a versatile approach for the synthesis of metal selenide NCs that allows for their large volume, low cost production.

Chapter IV

Synthesis of other CIS precursors

Previously, we have mentioned that for the formation of dense CIGS layers for photovoltaic applications various solution-based precursors are viable. Up to now, we have investigated, characterized and optimized the synthesis of colloidal nanocrystals of the CIGS system. Alternative precursors are based upon metal containing salts or complexes dissolved in a suitable solvent. The direct use of these precursors have lead to reasonable efficiencies of 4-8 %[30,51,52], yet a reoccurring problem seems the formation of a so-called double layer during thermal treatment. Basically, during annealing and/or selenization, a layer containing mainly carbon and small CIGS crystallites builds up near the back contact of the solar cell, while the dense CIGS layer is formed on top. Additional thermal treatments and excessive selenization conditions can reduce this problem partially, but it leads to limited device efficiencies.

In this chapter, we focus on the synthesis of decomposable metal dithiocarbamates. Dithiocarbamates are a class of molecules which can be used as a precursor for the formation of metal sulfides[53]. These strong metal chelating molecules are commercially available, or can be readily synthesized from their corresponding primary or secondary amines[54]. The phase formation during annealing is investigated using *in situ* XRD, performed by Boris Capon, supervised by Prof. Dr. Christophe Detavernier at the Department of Solid-State Sciences of Ghent University.

Next to dithiocarbamates, we design a synthesis for Se

nanoparticles. In an attempt to further simplify the process of ink to functional CIGS layer, our aim is to make these Se nanoparticles compatible with our CIS precursors, to create an excess of Se that can possibly replace gas-phase selenization. The synthesis and characterization of Se nanoparticles is discussed here, while the annealing of thin films with an excess of selenium is discussed in chapter IX.

4.1 Dithiocarbamates

4.1.1 Concept

The synthesis of metal dithiocarbamates is carried out as shown in the scheme in Figure 4.1a. The reaction involves the deprotonation of the amine by a base, followed by a nucleophilic attack on carbon disulfide. Basically any R group on the amine can be chosen, as long as it withstand the reaction conditions in order not to alter functional groups present. The resulting dithiocarbamate can be used to chelate metal cations, forming a strong complex (Figure 4.1b). The interesting part of dithiocarmate complexes for this work is shown in Figure 4.1c. Above a certain temperature, depending on the type of metal and the R group on the dithiocarbamate, the complex decomposes, forming a metal sulfide and a gaseous isothiocyanate. The versatility of these molecules and the neat decomposition reaction stimulates the use of these molecules as solution-based metal sulfide precursors[55,56]. The R groups on the dithiocarbamate will play an important role in their solubility and deposition behaviour, while it is possible to use a combination of monodithiocarbamates and bis-dithiocarbamates to obtain oligomer molecules.

4.1.2 Experimental

The synthesis of the targeted metal dithiocarbamates relies on a precipitation reaction in water. While the Cu(II), In(III) and dithiocarbamate salts used in the synthesis procedure are readily soluble in water, the resulting complex is hydrophobic. Therefore, we performed the synthesis of Cu- and In dithiocarbamate complexes by combining water-soluble Cu(II) and In(III) salts with ammonium pyrrolidinedithiocarbamate (APDC). 2 mmol $Cu(Ac)_2$ (0.182 g) is dissolved in 10 mL H_2O. In a seperate vial, 5 mmol of

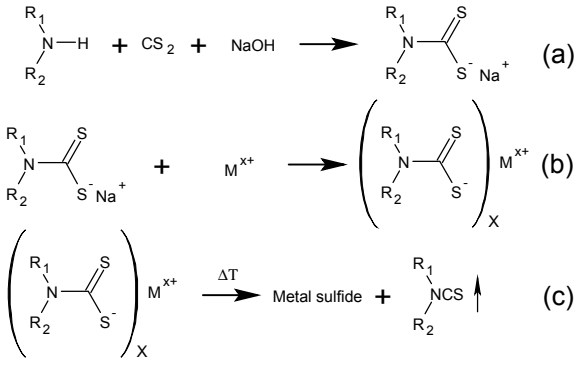

Figure 4.1: Synthesis and heat transformation behaviour of metal dithiocarbamates (a) Reaction from primary or secondary amine to dithiocarbamate. (b) Chelation of dithiocarbamates with metals. (c) Formation of metal sulfide.

APDC (0.821 g) is dissolved in 10 mL of H_2O. Next, the first solution is combined with the APDC solution resulting in the immediate formation of a brown precipitate. After 15 min of vigorous stirring at room temperature, the precipitate is collected by centrifugation. To remove excess APDC and NH_4OAc, the precipitate is washed 3 times with H_2O. Afterwards, it is placed in a drying oven at 70 °C to obtain a dry powder of $Cu(PDC)_2$. The synthesis of $In(PDC)_3$ is carried out in the same fashion, by using 2 mmol of $In(Ac)_3$ (0.292 g) and 7 mmol APDC (1.150 g).

4.1.3 Characterization

The resulting powders are characterized by Thermogravimetric Analysis (TGA) by measuring the mass of approximately 6 mg of material as a function of temperature. The yield of the reaction was measured by the mass of the dried powders. Thin films of the material are formed by dissolving the powder in methylpyrrolidone, and drop casting the resulting solution on a Si substrate heated to 60 °C. This allows for the analysis of the transformation of a metal dithiocarbamate film to a metal sulfide film by in an experimental stainless steel heating chamber, mounted in a Bruker D8 Discover, dedicated for *in situ* XRD. Cu K alpha radiation ($\lambda = 0.15406$ nm) was used as x-ray source, while a linear detector monitored the crystallinity of the films.

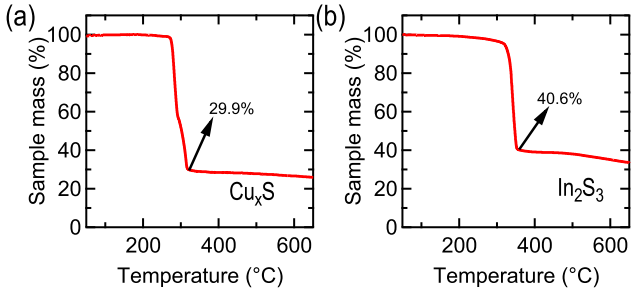

Figure 4.2: TGA curves of $Cu(PDC)_2$ (a) and $In(PDC)_3$ (b).

4.1.4 Results and discussion

The straightforward procedure we use for the synthesis and purification of Cu - and In dithiocarbamates allows chemical yields above 90%. The excess of APDC added to capture all free metal ions in solution can be easily removed by washing the precipitate several times with water. The resulting powders are materials with a seemingly long shelf-life, since we have no indication of reduced quality after a long storage time in air. It is also noted that this procedure can be easily extended to gallium dithiocarbamates.

Figure 4.2 shows the decomposition profiles of $Cu(PDC)_2$ and $In(PDC)_3$ in argon. We observe a high weight loss in a narrow temperature range for both complexes, which we attribute to the loss of the gaseous isothiocyanate. Considering the molecular mass of the complexes, i.e., 357.06 g/mol for $Cu(PDC)_2$ and 553.60 g/mol for $In(PDC)_3$, the weight loss of 2 and 3 isothiocyanate molecules for $Cu(PDC)_2$ and $In(PDC)_3$ corresponds to a loss of 70.1 % and 59.4 % of the initial weigth of the powder, respectively. As these levels are indeed reached at the end of the rapid weight drop, we conclude that the thermogravimetric analysis gives evidence of the fast and complete decomposition of the metal dithiocarbamate complex, leaving behind the corresponding metal sulfide. We also observe that, if the 2 compounds would be combined, copper sulfide will be formed at a lower temperature (318 °C) than indium sulfide (352 °C).

The formation of copper sulfide and indium sulfide from their corresponding dithiocarbamate complexes is investigated using *in situ* XRD. Thin films of the dithiocarbamate complexes are heated to 600 °C at a rate of 1 °C/s while a window of 20° 2θ is being

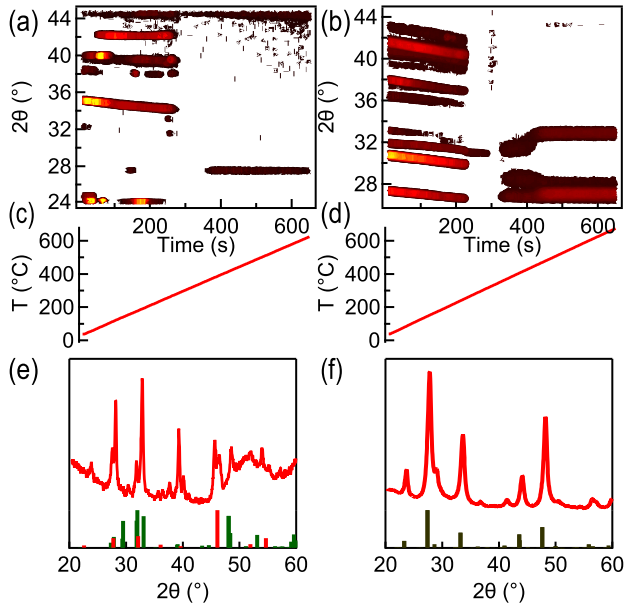

Figure 4.3: Investigation of phase formation. *In situ* XRD showing the diffractions during heating up of a $Cu(PDC)_2$ (a) and $In(PDC)_3$ (b) thin film. (c-d) Temperature profile of the *in situ* XRD measurements. (e) XRD pattern recorded after cooling down the obtained copper sulfide thin film and expected reflections of Cu_2S (red bars) and CuS (green bars). (f) XRD pattern recorded after cooling down the obtained indium sulfide thin film and expected reflections of In_2S_3 (brown bars).

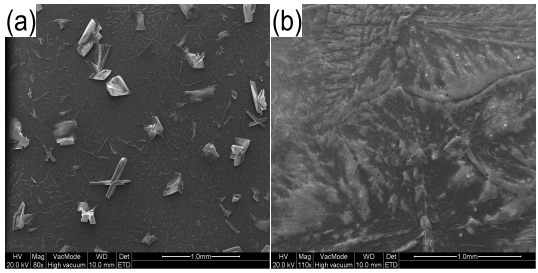

Figure 4.4: SEM images of a drop casted $Cu(PDC)_2$ (a) and $In(PDC)_3$ (b) thin film.

recorded (Figure 4.3). We notice that the peaks of crystalline $Cu(PDC)_2$ disappear starting from 305 °C, indicating the decomposition of the material. This is in agreement with temperature at which loss of material occurs in the TGA measurement. Peaks we assign to a mixture of Cu_2S and CuS phases start appearing when the temperature reaches 375 °C. Cu_2S can be formed by a transition from CuS, releasing gaseous sulfur. Similarly, the melting of $In(PDC)_3$ starts at 265 °C and In_2S_3 appears at 350 °C. When the samples are cooled down to room temperature, an XRD pattern is taken over a range of 20-60° 2θ. We notice that the resulting CuS film consists of a mixture of Cu_2S and CuS (Figure 4.3e), while the decomposition of $In(PDC)_3$ gives rise to an In_2S_3 thin film (Figure 4.3f). The results shown here suggest that crystalline CuS phases are formed at a higher temperature compared to In_2S_3, even though the decomposition of $Cu(PDC)_2$ occurs at a lower temperature than $In(PDC)_3$ (Figure 4.2).

For completeness, we also analyzed the morphology and composition of thin films of the dithiocarmate complexes by SEM-EDX (Figure 4.4). For $Cu(PDC)_2$ (Figure 4.4a), we measure a Cu to S ratio of 1:4, in line with the expected stoichiometry. Here, we notice the formation of large aggregates, which is an indication of precipitation at high concentrations during the drying process. In contrast, a relatively smooth $In(PDC)_3$ thin film is formed with a In to S ratio of 1:5.7, as shown in Figure 4.4b. We conclude that there is no excess of PDC in the dithiocarbamate complexes and that the drying behaviour of $In(PDC)_3$ results in a better thin film compared to $Cu(PDC)_2$.

4.2 Selenium nanoparticles

Se nanoparticles are synthesized by the reduction of selenious acid using a water-in-oil microemulsion process[57]. Here, small water droplets are formed in a hydrophobic solvent (oil), stabilized by surfactants. Because the precursors dissolve in the water phase, these droplets acts as reactors with their size limiting the final particle dimensions. To make the Se nanoparticles soluble in polar inks, and lose most of the organics, we designed a process to extract the nanoparticles to a polar phase. At the same time, this stops the growth of the Se nanoparticles.

4.2.1 Experimental

Two microemulsions are prepared in 8 mL heptane and 1.2 mL Brij30. In the first solution, 0.16 mmol H_2SeO_3 dissolved in 200 µL H_2O is added. The second microemulsion is prepared by the addition of 0.16 mmol $N_2H_4 \cdot H_2O$ (35 w% in H_2O) to 200 µL H_2O. *Caution: Hydrazine -even as an aqueous solution- is toxic and should be handled using appropriate protective equipment!* Both microemulsions are stirred for one hour to assure colloidal stability. To initiate the formation of Se nanoparticles, 2 mL of each microemulsion are added together and the reaction is cooled in an ice bath.

The reaction can be stopped by an extraction using S^{2-} or Se^{2-} salts dissolved in DMSO. For the reaction mixture above, 0.20 mmol Na_2S dissolved in 3 mL DMSO is added while stirring. The nanoparticles transfer to the polar phase as indicated by the color shift.

4.2.2 Characterization

The characteristics of the Se nanoparticles synthesized using a microemulsion procedure are shown in Figure 4.5. Three consecutive dynamic light scattering (DLS) measurements (Figure 4.5a) are performed on a solution of Se nanoparticles in DMSO, capped by Na_2S. Here, the extraction was done 60 s after the reaction was initiated. The mean size deducted from these graphs is 165 nm. SEM measurements were performed on a dried film of Se nanoparticles (Figure 4.5). This image shows quasi-spherical particles, and confirm the dimensions we derived from DLS measurements

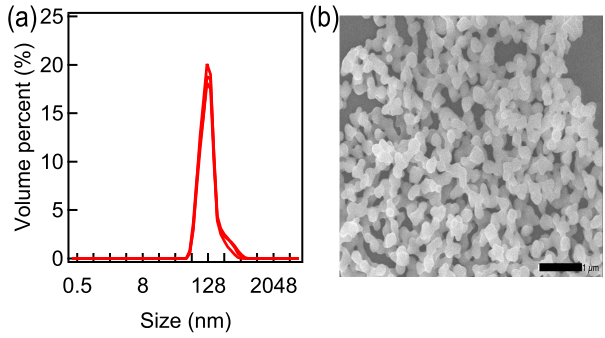

Figure 4.5: Characterization of Se nanoparticles. (a) DLS measurements. (b) SEM image of a dried layer (scale bar = 1 µm.

(190 nm).

4.3 Conclusions

We successfully synthesized Cu and In dithiocarbamate complexes with a simple, inexpensive and upscalable precipitation reaction in water. It is demonstrated that these complexes are interesting precursors for their corresponding sulfides, leaving behind gaseous molecules at a relatively mild thermal treatment. The versatility in dithiocarbamate molecules brings an additional advantage with respect to solubility in different solvents, from polar to apolar. This implies that the dithiocarbamate complexes can be added to NC inks, creating a so-called hybrid ink. Next to dithiocarbamates, we successfully synthesized selenium nanoparticles using a microemulsion reaction. Interestingly, we were able to extract the nanoparticles to a polar phase, by employing sulfide or selenide salts. This is a convenient approach to both purify the nanoparticles and tune their solubility to make them compatible with CIS precursors in a polar inks, which we will use in a later stage.

Bibliography

[1] Talapin, D. V.; Lee, J.-S.; Kovalenko, M. V.; Shevchenko, E. V. Prospects of colloidal nanocrystals for electronic and optoelectronic applications. *Chemical reviews* **2010**, *110*, 389–458.

[2] Murray, C.; Norris, D.; Bawendi, M. Synthesis and characterization of nearly monodisperse CdE (E= sulfur, selenium, tellurium) semiconductor nanocrystallites. *Journal of the American Chemical Society* **1993**, *115*, 8706–8715.

[3] Brust, M.; Walker, M.; Bethell, D. Synthesis of thiol-derivatised gold nanoparticles in a two-phase liquid-liquid system. *J. Chem. Soc., Chem. Comm.* **1994**, 8071–802.

[4] C. B. Murray, C. R. K.; Bawendi, M. G. Synthesis and characterization of monodisperse nanocrystals and close-packed nanocrystal assemblies. *Annual Review of Materials Science* **2000**, *30*, 610.

[5] Chan, E. M.; Xu, C.; Mao, A. W.; Han, G.; Owen, J. S.; Cohen, B. E.; Milliron, D. J. Reproducible, high-throughput synthesis of colloidal nanocrystals for optimization in multidimensional parameter space. *Nano letters* **2010**, *10*, 1874–85.

[6] Yin, Y.; Alivisatos, a. P. Colloidal nanocrystal synthesis and the organic-inorganic interface. *Nature* **2005**, *437*, 664–70.

[7] Peng, X.; Wickham, J.; Alivisatos, A. Kinetics of II-VI and III-V colloidal semiconductor nanocrystal growth: focusing of size distributions. *Journal of the American Chemical Society* **1998**, *7863*, 5343–5344.

[8] Peng, X. An essay on synthetic chemistry of colloidal nanocrystals. *Nano Research* **2010**, *2*, 425–447.

[9] Abe, S.; Capek, R. K.; De Geyter, B.; Hens, Z. Reaction chemistry/nanocrystal property relations in the hot injection synthesis, the role of the solute solubility. *ACS nano* **2013**, *7*, 943–949.

[10] Kolny-Olesiak, J.; Weller, H. Synthesis and Application of Colloidal $CuInS_2$ Semiconductor Nanocrystals. *ACS applied materials & interfaces* **2013**, *5*, 12221–37.

[11] Xie, R.; Rutherford, M.; Peng, X. Formation of high-quality I-III-VI semiconductor nanocrystals by tuning relative reactivity of cationic precursors. *Journal of the American Chemical*

Society **2009**, *131*, 5691–7.

[12] Booth, M.; Brown, A. Determining the concentration of $CuInS_2$ quantum dots from the size-dependent molar extinction coefficient. *Chemistry of Materials* **2012**, *24*, 2064–2070.

[13] Chen, B.; Zhong, H.; Zhang, W.; Tan, Z.; Li, Y.; Yu, C.; Zhai, T.; Bando, Y.; Yang, S.; Zou, B. Highly Emissive and Color-Tunable $CuInS_2$-Based Colloidal Semiconductor Nanocrystals: Off-Stoichiometry Effects and Improved Electroluminescence Performance. *Advanced Functional Materials* **2012**, *22*, 2081–2088.

[14] Li, L.; Pandey, A.; Werder, D. J.; Khanal, B. P.; Pietryga, J. M.; Klimov, V. I. Efficient Synthesis of Highly Luminescent Copper Indium Sulfide-Based Core/Shell Nanocrystals with Surprisingly Long-Lived Emission. *Journal of the American Chemical Society* **2010**, 0–3.

[15] Kruszynska, M.; Borchert, H.; Parisi, J.; Kolny-Olesiak, J. Synthesis and shape control of $CuInS_2$ nanoparticles. *Journal of the American Chemical Society* **2010**, *132*, 15976–86.

[16] Park, J.; Dvoracek, C.; Lee, K. H.; Galloway, J. F.; Bhang, H.-E. C.; Pomper, M. G.; Searson, P. C. CuInSe/ZnS core/shell NIR quantum dots for biomedical imaging. *Small* **2011**, *7*, 3148–52.

[17] Deng, D.; Chen, Y.; Cao, J.; Tian, J. High-quality $CuInS_2$/ZnS quantum dots for in vitro and in vivo bioimaging. *Chemistry of Materials* **2012**, *24*, 3029–3037.

[18] Panthani, M.; Khan, T.; Reid, D. In Vivo Whole Animal Fluorescence Imaging of a Microparticle-Based Oral Vaccine Containing ($CuInSe_xS_{2-x}$/ZnS Core/Shell Quantum Dots. *Nano Letters* **2013**, *13*, 4294–4298.

[19] Zhang, J.; Xie, R.; Yang, W. A Simple Route for Highly Luminescent Quaternary Cu-Zn-In-S Nanocrystal Emitters. *Chemistry of Materials* **2011**, *23*, 3357–3361.

[20] Chen, B.; Zhou, Q.; Li, J.; Zhang, F.; Liu, R.; Zou, B. Red emissive $CuInS_2$ -based nanocrystals: a potential phosphor for warm white light- emitting diodes. *Optics Express* **2013**, *21*, 10105–10110.

[21] Chung, W.; Jung, H.; Lee, C. H.; Park, S. H.; Kim, J.; Kim, S. H. Synthesis and Application of Non-Toxic $ZnCuInS_2$/ZnS Nanocrystals for White LED by Hybridiza-

tion with Conjugated Polymer. *Journal of The Electrochemical Society* **2011**, *158*, 1218–1220.

[22] Panthani, M.; Stolle, C. $CuInSe_2$ Quantum Dot Solar Cells with High Open-Circuit Voltage. *The Journal of Physical Chemistry Letters* **2013**, *4*, 2030–2034.

[23] Panthani, M. G.; Akhavan, V.; Goodfellow, B.; Schmidtke, J. P.; Dunn, L.; Dodabalapur, A.; Barbara, P. F.; Korgel, B. A. Synthesis of $CuInS_2$, $CuInSe_2$, and $Cu(In_xGa_{1-x})Se_2$ (CIGS), Nanocrystal Inks for Printable Photovoltaics. *Journal of American Chemical Society* **2008**, *2*, 16770–16777.

[24] Niezgoda, J.; Yap, E.; Keene, J. Plasmonic $Cu_xIn_yS_2$ Quantum Dots Make Better Photovoltaics Than Their non-Plasmonic Counterparts. *Nano letters* **2014**, *14*, 3262–3269.

[25] Todorov, T.; Mitzi, D. B. Direct Liquid Coating of Chalcopyrite Light-Absorbing Layers for Photovoltaic Devices. *European Journal of Inorganic Chemistry* **2010**, *2010*, 17–28.

[26] Hibberd, C. J.; Chassaing, E.; Liu, W.; Mitzi, D. B.; Lincot, D.; Tiwari, a. N. Non-vacuum methods for formation of Cu(In, Ga)(Se, S)$_2$ thin film photovoltaic absorbers. *Progress in Photovoltaics: Research and Applications* **2010**, *18*, 434–452.

[27] Guo, Q.; Ford, G. G. M.; Hillhouse, H. W. H.; Agrawal, R. Sulfide nanocrystal inks for dense $Cu(In_{1-x}Ga_x)(S_{1-y}Se_y)_2$ absorber films and their photovoltaic performance. *Nano letters* **2009**, *9*, 3060–5.

[28] Guo, Q.; Ford, G. Ink formulation and low temperature incorporation of sodium to yield 12% efficient Cu(In, Ga)(S, Se)$_2$ solar cells from sulfide nanocrystal inks. *Progress in Photovoltaics: Research and Applications* **2013**, *21*, 64–71.

[29] Cho, A.; Ahn, S.; Yun, J. H.; Gwak, J.; Song, H.; Yoon, K. A hybrid ink of binary copper sulfide nanoparticles and indium precursor solution for a dense $CuInSe_2$ absorber thin film and its photovoltaic performance. *Journal of Materials Chemistry* **2012**, *22*, 17893.

[30] Wang, W.; Su, Y.-W.; Chang, C.-h. Inkjet printed chalcopyrite $CuIn_xGa_{1-x}Se_2$ thin film solar cells. *Solar Energy Materials and Solar Cells* **2011**, *95*, 2616–2620.

[31] Peña, Y.; Lugo, S.; Calixto-Rodriguez, M.; Vázquez, A.;

Gómez, I.; Elizondo, P. $CuInS_2$ thin films obtained through the annealing of chemically deposited In_2S_3-CuS thin films. *Applied Surface Science* **2011**, *257*, 2193–2196.

[32] Uhl, A. R.; Fella, C.; Chirila, A.; Kaelin, M. R.; Karvonen, L.; Weidenkaff, A.; Borca, C. N.; Grolimund, D.; Romanyuk, Y. E.; Tiwari, A. N. Non-vacuum deposition of $Cu(In,Ga)Se_2$ absorber layers from binder free, alcohol solutions. *Progress in Photovoltaics: Research and Applications* **2012**, *20*, 526–533.

[33] Moreels, I.; Lambert, K.; Muynck, D. D.; Zhao, Q.; Tomme, V.; Vanhaecke, F.; Hens, Z. Optical Properties of Zincblende Cadmium Selenide Quantum Dots. *Journal of Physical Chemistry C* **2010**, *114*, 6371–6376.

[34] Moreels, I.; Lambert, K.; De Muynck, D.; Vanhaecke, F.; Poelman, D.; Martins, J. C.; Allan, G.; Hens, Z. Composition and Size-Dependent Extinction Coefficient of Colloidal PbSe Quantum Dots. *Chemistry of Materials* **2007**, *19*, 6101–6106.

[35] Alonso, M.; Wakita, K.; Pascual, J.; Garriga, M.; Yamamoto, N. Optical functions and electronic structure of $CuInSe_2$, $CuGaSe_2$, $CuInS_2$, and $CuGaS_2$. *Physical Review B* **2001**, *63*, 1–13.

[36] Liu, X.; Wang, X.; Zhou, B.; Law, W.-C.; Cartwright, A. N.; Swihart, M. T. Size-Controlled Synthesis of $Cu_{2-x}E$ (E = S, Se) Nanocrystals with Strong Tunable Near-Infrared Localized Surface Plasmon Resonance and High Conductivity in Thin Films. *Advanced Functional Materials* **2012**, *23*, 1256–1264.

[37] Zhao, Y.; Pan, H.; Lou, Y.; Qiu, X.; Zhu, J.; Burda, C. Plasmonic $Cu_{2-x}S$ nanocrystals: optical and structural properties of copper-deficient copper(I) sulfides. *Journal of the American Chemical Society* **2009**, *131*, 4253–61.

[38] Xie, Y.; Riedinger, A.; Prato, M.; Casu, A.; Genovese, A.; Guardia, P.; Sottini, S.; Sangregorio, C.; Miszta, K.; Ghosh, S.; Pellegrino, T.; Manna, L. Copper Sulfide Nanocrystals with Tunable Composition by Reduction of Covellite Nanocrystals with Cu+ Ions. *Journal of the American Chemical Society* **2013**, *135*, 17630–17637.

[39] Zhong, H.; Wang, Z.; Bovero, E.; Lu, Z.; van Veggel, F. C. J. M.; Scholes, G. D. Colloidal $CuInSe_2$ Nanocrystals in the

Quantum Confinement Regime: Synthesis, Optical Properties, and Electroluminescence. *The Journal of Physical Chemistry C* **2011**, *115*, 12396–12402.

[40] Kar, M.; Agrawal, R.; Hillhouse, H. W. Formation pathway of CuInSe2 nanocrystals for solar cells. *Journal of the American Chemical Society* **2011**, *133*, 17239–47.

[41] Guo, Q.; Kim, S.; Kar, M.; Shafarman, W. Development of $CuInSe_2$ nanocrystal and nanoring inks for low-cost solar cells. *Nano letters* **2008**, *8*, 1–6.

[42] Wu, C.-H.; Chen, F.-S.; Lin, S.-H.; Lu, C.-H. Preparation and characterization of $CuInSe_2$ particles via the hydrothermal route for thin-film solar cells. *Journal of Alloys and Compounds* **2011**, *509*, 5783–5788.

[43] Zhong, H.; Li, Y.; Ye, M.; Zhu, Z.; Zhou, Y.; Yang, C.; Li, Y. A facile route to synthesize chalcopyrite $CuInSe_2$ nanocrystals in non-coordinating solvent. *Nanotechnology* **2007**, *18*, 025602.

[44] Flamee, S.; Cirillo, M.; Abe, S.; De Nolf, K.; Gomes, R.; Aubert, T.; Hens, Z. Fast, High Yield, and High Solid Loading Synthesis of Metal Selenide Nanocrystals. *Chemistry of Materials* **2013**, *25*, 2476–2483.

[45] Dorfs, D.; Härtling, T.; Miszta, K.; Bigall, N. C.; Kim, M. R.; Genovese, A.; Falqui, A.; Povia, M.; Manna, L. Reversible tunability of the near-infrared valence band plasmon resonance in $Cu_{2-x}Se$ nanocrystals. *Journal of the American Chemical Society* **2011**, *133*, 11175–80.

[46] Tang, J.; Hinds, S.; Kelley, S.; Sargent, E. Synthesis of Colloidal $CuGaSe_2$, $CuInSe_2$, and $Cu(InGa)Se_2$ Nanoparticles. *Chemistry of Materials* **2008**, *20*, 6906–6910.

[47] Bullen, C.; Van Embden, J.; Jasieniak, J.; Cosgriff, J. E.; Mulder, R. J.; Rizzardo, E.; Gu, M.; Raston, C. L. High activity phosphine-free selenium precursor solution for semiconductor nanocrystal growth. *Chemistry of Materials* **2010**, *22*, 4135–4143.

[48] Park, K. H.; Jang, K.; Kim, S.; Kim, H. J.; Son, S. U. Phase-controlled one-dimensional shape evolution of InSe nanocrystals. *Journal of the American Chemical Society* **2006**, *128*, 14780–1.

[49] Ning, J.; Xiao, G.; Wang, C.; Liu, B.; Zou, G.; Zou, B. Syn-

thesis of doped zinc blende-phase InSe: M (M= Fe and Co) nanocrystals for diluted magnetic semiconductor nanomaterials. *CrystEngComm* **2013**, *15*, 3734–3738.

[50] Hsiang, H.-I.; Lu, L.-H.; Chang, Y.-L.; Ray, D.; Yen, F.-S. Solvo-Thermal Synthesis and Characterization of Indium Selenide Nanocrystals. *Journal of the American Ceramic Society* **2011**, *94*, 3757–3760.

[51] Lee, E.; Park, S. J.; Cho, J. W.; Gwak, J.; Oh, M.-K.; Min, B. K. Nearly carbon-free printable CIGS thin films for solar cell applications. *Solar Energy Materials and Solar Cells* **2011**, *95*, 2928–2932.

[52] Park, M.; Ahn, S. S.; Yun, J. H.; Gwak, J.; Cho, A.; Shin, K.; Nam, D.; Cheong, H.; Yoon, K. Characteristics of Cu(In,Ga)Se_2 (CIGS) thin films deposited by a direct solution coating process. *Journal of Alloys and Compounds* **2012**, *513*, 68–74.

[53] Sharma, A. Thermal behaviour of metal-dithiocarbamates. *Thermochimica acta* **1986**, *104*, 339–372.

[54] Engels, H.; Weidenhaupt, H. Rubber, 4. Chemicals and additives. In *Ullmann's Encyclopedia of Industrial Chemistry*; Wiley Online Library, 2004; Chapter 4.

[55] Edler, M.; Rath, T.; Schenk, A.; Fischereder, A.; Haas, W.; Edler, M.; Chernev, B.; Kunert, B.; Hofer, F.; Resel, R.; Trimmel, G. Copper zinc tin sulfide layers prepared from solution processable metal dithiocarbamate precursors. *Materials Chemistry and Physics* **2012**, *136*, 582–588.

[56] Regulacio, M.; Tomson, N.; Stoll, S. Dithiocarbamate precursors for rare-earth sulfides. *Chemistry of materials* **2005**, 3114–3121.

[57] Aubert, T.; Grasset, F.; Mornet, S.; Duguet, E.; Cador, O.; Cordier, S.; Molard, Y.; Demange, V.; Mortier, M.; Haneda, H. Functional silica nanoparticles synthesized by water-in-oil microemulsion processes. *Journal of colloid and interface science* **2010**, *341*, 201–208.

Part 2: Surface chemistry of colloidal nanocrystals

Introduction

As with all colloidal nanocrystals formed by hot-injection or heating up procedures in organic solvents, CIGS NCs come with a layer of organic ligands bound to the surface of the NC. In all types of applications, the importance of post-synthetic processing of CIGS NCs can hardly be overestimated. Next to the growth of inorganic shells around the as-synthesized NCs, this concerns the tailoring of the CIGS NC surface chemistry, where the long ligands typically used during synthesis are replaced by more appropriate ligands in view of a particular application. Bio-imaging for example requires water soluble nanocrystals, while for a NC-based solar cell, charge transport between adjacent NCs in a thin film is enhanced when the NC surface is passivated by short chain moieties[1,2].

The successful tailoring of the NC surface chemistry starts from an understanding of the binding of ligands to as-synthesized NCs. Detailed studies on metal chalcogenide or pnictide nanocrystals synthesized in apolar media using hot injection or heating up approaches, including CdSe[3,4], CdTe[5], PbS[6], PbSe[7] and InP[8,9], have shown that the classification of ligands as L-type, X-type or Z-type depending on the number of electrons the NC-ligand bond takes from the NC (0, 1 and 2, respectively) to form a 2-electron bond is a convenient approach[10–12]. This is shown in the scheme in Figure 4.6, where the binding motifs are presented according to covalent bond classification method.

In combination with the need to form charge-neutral nanocrystals in apolar environments, this results in two extreme classes. The first describes NCs where the formal charge on the cations and anions is balanced - for binary NCs, this corresponds to the bulk stoichiometry - and which are passivated by L-type ligands (NC-L_n). The second are NCs that have a net formal charge that is balanced by the opposite charge on X-type ligands. Typically, this involves NCs having an excess of metal cations, stabilized by ligands

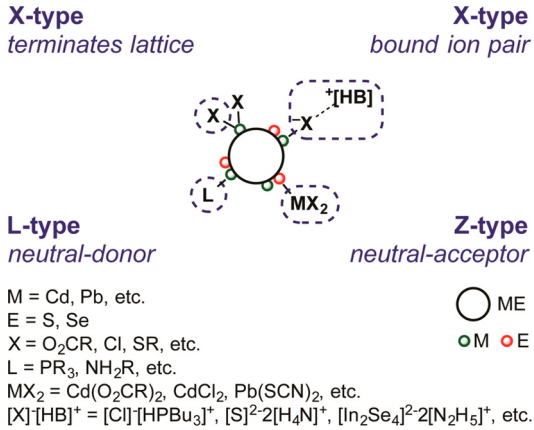

Figure 4.6: Nanocrystal ligand binding motifs according to the covalent bond classification method[1].

with a formally negative charge - denoted here as NC-$(MX_x)_n$ - although the opposite situation of an anion rich nanocrystal with positively charged ligands could also be possible. Remarkably, all detailed, quantitative studies addressing stoichiometry and ligand binding published so far showed as-synthesized and purified NCs behaving according to the NC-$(MX_x)_n$ class, where X- moieties correspond to, e.g., carboxylates or phosphonates[3,5,7]. L-type ligands such as amines or phosphines on the other hand typically exhibit a dynamic adsorption/desorption equilibrium[6,9], suggesting that the NC-L_n class results in labile NCs that do not withstand repetitive sample purification. Since L-type ligands take the 2 electrons forming the NC-ligand bond upon desorption, while X-type ligands only provide 1, both ligand types are incompatible for ligand exchange reactions, provided that the composition of the NC is to be preserved. This understanding forms the basis to design purposeful ligand exchange strategies, involving separate X-by-X and L-by-L exchange but also more involved exchange schemes such as L-type promoted Z-type displacement[10].

In spite of the growing importance of CIGS NCs, few studies, if any, have addressed the surface chemistry of as-synthesized NCs and investigated possible ligand exchange reactions. Ligand exchange is either monitored by a successful phase transfer from an apolar to a polar phase[13], or by relatively indirect techniques

[1]Adapted with permission from Anderson *et al*, *J. Am. Chem. Soc.* **2013**, 135,18536-48. Copyright 2013 American Chemical Society.

such as infrared spectroscopy and thermogravimetric analysis[13–15]. More systematic studies are, to the best of our knowledge, missing although the understanding of the binding of ligands to as-synthesized CIGS NCs is the basis for designing ligand exchange reactions and advance application development. For the formation of dense CIGS layers, for example, it has been acknowledged that partial removal of oleylamine from CIGS NCs enhances recrystallization in the NC film[16]. Solution ^{1}H Nuclear Magnetic Resonance (NMR) spectroscopy stands out as a preferred tool in the surface chemistry analysis of colloidal NCs, offering an extensive toolbox to *in-situ* identify and quantify bound ligands. This is based on general characteristics of bound ligand resonances, which shift and broaden relative to the free ligands in the 1D ^{1}H spectrum, exhibit the slow diffusion characteristic of larger nano-objects and feature strongly negative nuclear Overhauser effect crosspeaks (NOEs)[12].

In this part, we analyze the surface chemistry and explore ligand exchange reactions of $CuInS_2$ NCs (CIS in short) synthesized in the presence of amines. When using high purity octadecylamine (ODAm), we find that the formal charge of the metal cations matches that of the sulfide anions. By means of solution ^{1}H NMR, we demonstrate that such CIS/ODAm NCs have a capping of tightly bound amines. Based on the results of heating experiments monitored *in situ* in the NMR spectrometer - which gives evidence of self-desorption of ODAm - we argue that amines bind to CIS NCs as L-type ligands, making CIS/ODAm NCs a rare example of the NC-L_n class. This point is further supported by similar measurements on wurtzite CdSe NCs capped with octadecylphosphonic acid, a known example of the NC-$(MX_x)_n$ class[17], where no signature of self-desorption is observed as expected for X-type ligands and by the finding that excess ODAm directly binds to CIS NCs. In line with the classification as NC-L_n, we find that long time, high temperature exposure of CIS/ODAm to fatty acids only results in desorption of ODAm and not in binding of carboxylic acids. Thiols on the other hand can effectively replace ODAm and bind to CIS NCs as L-type ligands. Remarkably, when replacing high purity ODAm in the synthesis by technical oleylamine (OLAm), we obtain cation-rich NCs that can bind both L-type (amines, thiols) and X-type ligands (carboxylates, thiolates) to their surface. In this way, these results not only give insight in

the surface chemistry of $CuInS_2$ NCs - where a generic method to identify L-type ligands is introduced - they also show once more how often ill-controlled differences in the reagent composition can strongly influence the NC surface chemistry and subsequent ligand exchange reactions.

In a second chapter, the possibility of using inorganic chalcogenide ligands for CIS NCs is explored. We demonstrate that the exchange for OLAm on CIS for $(NH_4)_2S$ is successful in the sense that all OLAm molecules are stripped of the NC surface. Moreover, we investigate the colloidal stability of the CIS NCs capped by inorganic ligands. We find that exchange for $(NH_4)_2S$ leads to a rather poor colloidal stability, with dispersions of CIS NCs settling in solution within days. A solution is found in the use of chlorine containing salts, where we demonstrate an increased stability and a longer shelf-life. These findings provide the basics for our optimized hybrid ink which is used as a $CuInSe_2$ precursor in Chapter IX.

Chapter V

The surface chemistry of $CuInS_2$ colloidal nanocrystals, tight binding of L-type ligands

In this chapter, we present a systematic study on the surface chemistry of CIS NCs. We start from understanding and classifying the ligands on as-synthesized CIS NCs, obtained by employing high purity octadecylamine (ODAm) as the sole ligand. By understanding the surface chemistry on these NCs, possible ligand exchange strategies can be designed. We illustrate this by performing ligand exchange towards thiols and carboxylic acids, and place our results in the framework of the covalent bond classification method. NMR measurements were performed by Freya Van Den Broeck at the NMR and Structure Analysis Unit of Prof. dr. José C. Martins at Ghent University.

5.1 Experimental

Nanocrystal synthesis. CIS NCs capped with 1-octadecylamine (ODAm) or oleylamine (OLAm) were prepared in a heating-up fashion. 0.262 g of $Cu(acac)_2$ (1 mmol, $\geq$99.99 % Aldrich), 0.412 g of $In(acac)_3$ (1 mmol, $\geq$99.99 % Aldrich) and 0.065 g elemental S (2.05 mmol, 99.999 % Strem) are combined in a three-neck flask. For ODAm-capped CIS NCs, 1.632 g ODAm (6.06 mmol, for synthesis, Merck) and 14 mL 1-octadecene (ODE) are added, while 2 mL OLAm (6.06 mmol, 80-90 % Acros) and 14 mL ODE are added to obtain OLAm-capped NCs. Next, the flask is attached

to a Schlenk line and flushed with nitrogen over the course of 1 h. The mixture is then heated to 240 ℃ at 80 ℃/min using an infrared heating device while stirring vigorously. During this period, the precursors dissolve and form CIS NCs indicated by a change in color from a brown heterogeneous to a clear black mixture. After 1 h, the flask is cooled to room temperature using a water bath. Toluene and ethanol are added to wash the CIS NCs, which are then separated using a centrifuge. The resulting NC pellet after discarding the supernatant is redissolved in toluene and kept inside a water and oxygen-free glove box as a stock solution. Wurtzite CdSe NCs capped by $ODPAc^-$ and $ODPanh^{2-}$ moieties are obtained according to the procedure of Carbone *et al*[18], and were purified for NMR according to Gomes *et al*[17].

RBS measurements. Samples for Rutherford backscattering spectrometry (RBS) were prepared using CIS NCs dispersions washed twice after the synthesis. A thin film of ≈100 nm was deposited on a MgO substrate by spin-coating a CIS NC dispersion in toluene. RBS was performed by measuring backscattered He^+ ions accelerated to an energy of 1.57 MeV with an NEC 5SDH-2 Pelletron tandem accelerator with a semiconductor detector at a backscattering angle of 168°. Atomic ratios are determined from the experimental spectrum as the $1/Z^2$ weighted ratio of the energy integrated backscattering intensities - obtained by numerical integration of the raw data - where the main error results from uncertainties on the background correction. This error is estimated by comparing the integrals without any background correction and with an optimized background correction. The latter involves subtracting the average signal intensity at lower and higher energy of a given peak from the measured backscattering intensity. RBS measurements were performed by Qiang Zhao at Instituut voor Kernen Stralingsfysica of Prof. dr. André Vantomme, KU Leuven.

Ligand exchange. For a typical ligand exchange experiment to oleic acid (OAc) or 2-phenylethanethiol (PET), 2 mL of CIS NC stock solution in toluene (≈40 mg/mL) was first precipitated/redispersed twice using ethanol and chloroform. Next, the NCs are dissolved in o-dichlorobenzene, and 1.5 mL of PET (11.2 mmol, 98 % Aldrich) or 3.5 mL of OAc (11.25 mmol, 90 % Alfa Aesar) are added and the resulting solutions are stirred for 2 h inside a glovebox at 130℃. This procedure is repeated two

more times in between which the NCs are each time precipitated using ethanol and separated using centrifugation.

^{1}H NMR measurements. NMR samples with a minimal amount of impurities are prepared by washing the CIS NC dispersion at least twice after synthesis or exposure to an excess of new ligands. To avoid water contamination, the resulting pellet is dissolved in the appropriate solvent and transferred to a glovebox, where a strong nitrogen flow is used to dry the sample. The resulting dry NCs are dissolved in deuterated solvent and transferred to an NMR tube. Nuclear magnetic resonance (NMR) measurements were recorded on a Bruker Avance III Spectrometer operating at a ^{1}H frequency of 500.13 MHz and equipped with a BBI-Z probe or on a Bruker Avance II Spectrometer operating at a ^{1}H frequency of 500.13 MHz and equipped with a TXI-Z probe (channels are ^{1}H, ^{13}C, ^{31}P). The sample temperature was set to 298.2 K except when stated differently. For the high-temperature measurements, the temperature of the probe was calibrated following the method of Findeisen *et al*[19]. During temperature measurements the sample was always given sufficient time to stabilize, and parameters were optimized before measuring quantitative 1D ^{1}H measurements. One dimensional (1D) ^{1}H and 2D NOESY (nuclear Overhauser effect spectroscopy) spectra were acquired using standard pulse sequences from the Bruker library. For the quantitative 1D ^{1}H measurements, 64k data points were sampled with the spectral width set to 16 ppm and a relaxation delay of 30 s. NOESY mixing time was set to 300 ms and 2048 data points in the direct dimension for 512 data points in the indirect dimension were typically sampled, with the spectral width set to 11.5 ppm. Diffusion measurements (2D DOSY) were performed using a double stimulated echo sequence for convection compensation and with monopolar gradient pulses[20]. Smoothed rectangle gradient pulse shapes were used throughout. The gradient strength was varied linearly from 2 to 95 % of the probes maximum value (calibrated at 50.2 G/cm) in 32 or 64 steps, with the gradient pulse duration and diffusion delay optimized to ensure a final attenuation of the signal in the final increment of less than 10 % relative to the first increment. For 2D processing, the spectra were zero filled to a 4096 x 2048 real data matrix. Before Fourier transformation, the 2D spectra were multiplied with a squared cosine bell function in both dimensions, and the 1D spectra were multiplied with

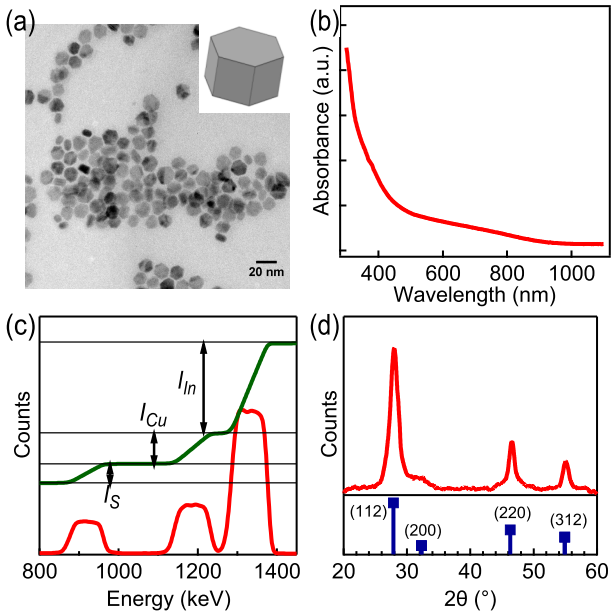

Figure 5.1: Characterization of as-synthesized CIS/ODAm NCs. (a) TEM micrograph and cartoon representation of the CIS NC morphology. (b) UV-vis absorption spectrum of a CIS/ODAm dispersion in chloroform. (c) (red) Rutherford Backscattering Spectrum (RBS) and (green) integrated backscattering intensities of a CIS NC thin film spin-coated on a MgO substrate. (d) (red) XRD pattern of a CIS NC thin film and (blue) database pattern for chalcopyrite $CuInS_2$.

an exponential window function. Concentrations were obtained using the Digital ERETIC tool in Topspin 3.0 that is based on the PULCON method[21]. The diffusion coefficients were obtained by fitting the appropriate Stejskal-Tanner equation to the signal intensity decay[22].

5.2 Results and discussion

5.2.1 Characterization of as-synthesized $CuInS_2$ nanocrystals

Figure 5.1 represents the basic characteristics of $CuInS_2$ (CIS) NCs synthesized from copper and indium acetylacetonate and elemental sulfur in a mixture of 1-octadecene (ODE) and 1-octadecylamine (ODAm), NCs we will refer to as CIS/ODAm.

As indicated in Figure 5.1a, the approach leads to anisotropic, tile-shaped CIS NCs having a hexagonal top surface with edges of 7.6±1.3 nm and a height of 6.9±0.7 nm. In line with their dimensions, these CIS NCs show an absorption onset at ≈850 nm, which is in agreement with the CIS bulk band gap of 1.45 eV. Weighting by Z^{-2}, the integrated intensities of He^+ backscattering on S, Cu, and In nuclei in the Rutherford Backscattering Spectrum shown in Figure 5.1c yield a Cu:In ratio of 0.96±0.01 and a S:In ratio of 1.97±0.03. This results in a ratio between the formal charge on the metal cations (Cu^+ and In^{3+}) and the sulfide anions (S^{2-}) of 1.00±0.02. Hence, the CIS NCs used here are slightly In-rich, yet charge neutral. Finally, X-ray diffraction (XRD) measurements on a thin film of CIS NCs confirms that the NCs have the chalcopyrite crystal structure (Figure 5.1d).

The 1D solution ^{1}H NMR spectra of ODAm and a well/purified CIS/ODAm NC dispersion in deuterated 1,2-dichlorobenzene are shown in Figure 5.2a. Apart from residual solvent resonances, the CIS/ODAm spectrum features two broadened resonances at 0.95 and 1.35 ppm. To attribute these signals, a HSQC spectrum is taken of the same dispersion. Figure 5.3 shows ^{1}H-^{13}C HSQC signals of both ODAm and CIS/ODAm NCs in deuterated 1,2-dichlorobenzene. We can attribute the peak at 0.9 ppm to the CH_3 of ODAm, since it shows a positive signal in HSQC, while negative signals are found for the large pool of CH_2 resonances between 1.2-1.4 ppm. Moreover, all discernible ^{13}C resonances of CIS/ODAm agree with ^{13}C resonances of free ODAm, which confirms the assignment of the broadened resonances to bound ODAm. Note that the two resonances in the ^{1}H NMR spectrum in Figure 5.2a are not accompanied by the narrower, shifted resonances that would be characteristic for free ligands[9]. The assignment of the resonances to bound ODAm is further confirmed by the combination of DOSY and NOESY measurements (see Figure 5.2b-c), which indicate that (1) the broadened resonances have strong and negative NOE cross peaks and (2) they are linked to species with a diffusion coefficient as low as 53.2±1.7 µm^2/s. Using the Stokes-Einstein equation for a disk moving at random, this corresponds to a top surface hydrodynamic diameter of 21.5±1.2 nm. This value closely matches twice the CIS top surface edge (7.6±1.3 nm) increased by the thickness of the ODAm capping (≈2 nm). We thus conclude that the broadened resonances in the 1D solution ^{1}H NMR spec-

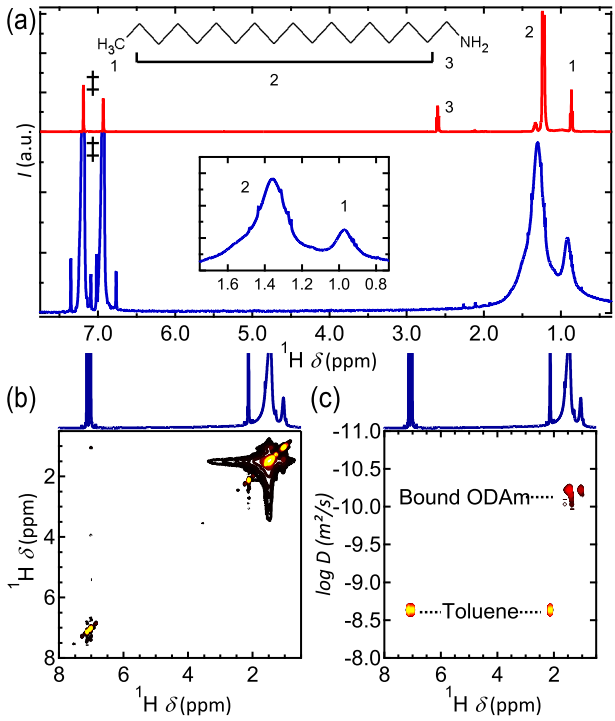

Figure 5.2: (a) 1D ^{1}H NMR spectrum of (red) ODAm and (blue) a purified CIS/ODAm dispersion in 1,2-dichlorobenzene-*d4*. Inset: zoom on the alkyl region. Resonances 1 and 2 are attributed to the CH_3 and CH_2 signals of ODAm, respectively. ‡ denotes the solvent resonances. (b) NOESY NMR spectrum of CIS/ODAm NCs capped with ODAm in toluene-*d8*. Here, only negative NOEs are shown. (c) DOSY NMR spectrum of the same solution.

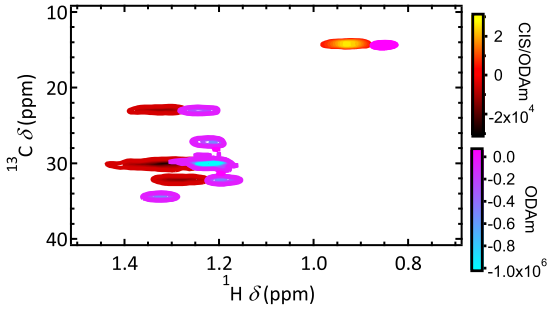

Figure 5.3: HSQC spectrum of ODAm (cyan-magenta) and CIS/ODAm (red-yellow).

trum of CIS NCs correspond to tightly bound ODAm ligands, not involved in chemical exchange with a pool of free ODAm.

By means of the quantitative 1D ^{1}H NMR spectrum shown in Figure 5.2a, the concentration of bound ODAm can be determined by integration of the CH_3 resonance. The concentration of CIS NCs is derived from the theoretical intrinsic absorption coefficient of freely rotating, prolate CIS NCs at 400 nm in chloroform [23]. For the calculation, which yields a value of 1.32 x 10^5 cm^{-1}, we used the bulk optical constants of CIS [24] and considered the actual dimensions of the NCs as given by TEM. Combined with the concentration of bound ODAm this leads to a ligand density of $3.8 \pm 0.5\,nm^{-2}$, a value which is in line with typical ligand densities derived for sterically stabilized colloidal NCs synthesized using hot injection or heating up approaches [12].

5.2.2 The $CuInS_2$/amine bond

Typically, L-type ligands such as amines or phosphine oxides are involved in a fast, dynamic adsorption/desorption equilibrium that can be shifted, for example, by diluting the dispersion [6,25,26]. In the case of CdSe and CdTe NCs, it was found that exchange rates can exceed $100\,s^{-1}$. On the other hand, X-type ligands such as carboxylates or phosphonates appear as tightly bound ligands in ^{1}H NMR spectra, not showing any indication of chemical exchange unless, e.g., a proton donor is added [3,27]. The observation of amine ligands tightly bound to CIS NCs thus raises the question as to what the binding motif of amines is in this case.

A possible way to establish the binding motif is by investigating self-desorption or self-adsorption, i.e., the breaking or forming of the ligand-NC bond, of ligands. Self-desorption of X-type ligands that bind as anionic (or cationic) moieties would result in a free anion (or cation) and a charged NC, a process that is highly unfavorable in apolar solvents due to the high solvation free energy of charged species in media with a low dielectric constant. Self-adsorption on the other hand requires a proton transfer step in the case of, e.g., carboxylate or phosphonate ligands. In the case of L-type ligands, self-desorption is not hindered by charging, which enables, for example, the fast, dynamic adsorption/desorption behaviour as discussed above. Since ODAm shows no indication of exchange at CIS NCs at room temperature, we therefore studied ligand desorption by changing the temperature of the NMR sample

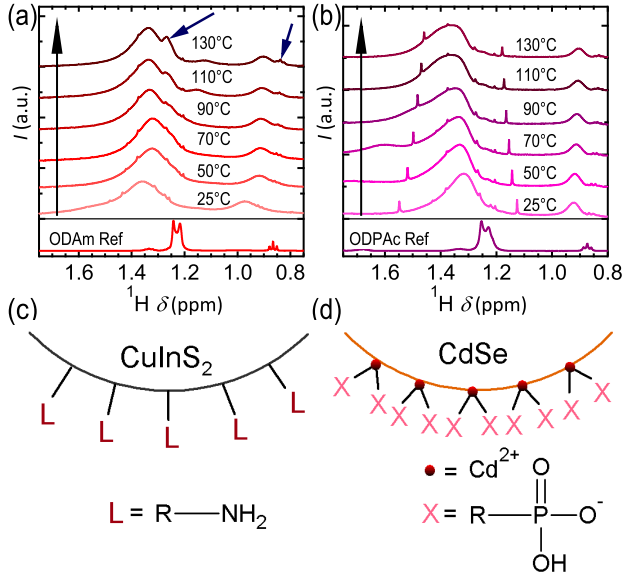

Figure 5.4: *In situ* heating-up NMR experiments in 1,2-dichlorobenzene-*d4* showing the effect of increased temperature on the alkyl region of CIS NCs capped with ODAm (a) and the alkyl region of CdSe NCs stabilized by ODPAc (b). Arrows in blue emphasize the appearance of sharper resonances. (c-d) Schematic representation of the CIS NC and CdSe NC surface. Reference (ref) spectra of both ODAm and ODPAc at 25 ℃ in 1,2-dichlorobenzene-*d4* are added on the bottom for comparison.

in situ for both CIS/ODAm dispersions and dispersions of wurtzite CdSe NCs stabilized by octadecylphosphonic acid (CdSe/ODPAc), a well-known NC-$(MX_2)_n$ system[17] that we used as a reference.

In Figure 5.4, we compare a series of zoomed in 1D ^{1}H NMR spectra recorded on CIS/ODAm (Figure 5.4a) and CdSe/ODPAc (Figure 5.4b) dispersions in 1,2-dichlorobenzene-*d4*, where both samples where heated from room temperature up to 130 ℃ in steps of 20 ℃ at temperatures above 50 ℃. Figure 5.4a shows that the broad CH_2 and CH_3 resonances of ODAm bound to CIS NCs somewhat shift and change intensity with increasing temperature. Moreover, sharper resonances with a downfield shift start to accompany both resonances at temperatures of 90 ℃ or higher. In the case of CdSe/ODPAc, on the other hand, the broad resonances of the CH_2 and CH_3 resonances merely exhibit a change in intensity, without the appearance of an additional, sharper resonance. A shifted and sharper resonance that accompanies each broad resonance of bound ligands points to the presence of a pool of free ligands that is at best in slow exchange with the bound ligands on the relevant NMR time scale. We thus conclude that ODAm, while tightly bound to the CIS surface at room temperature, shows a self-desorption at elevated temperatures that is absent in the case of CdSe/ODPAc. Whereas the latter is the expected behaviour for X-type ligands, the appearance of free ODAm in heated CIS/ODAm dispersions is a first indication that amines interact with CIS NCs as L-type ligands as depicted in the scheme given in Figure 5.4c.

A possible issue with this conclusion comes from the observation that in the case of CdSe NCs stabilized by carboxylates - again a well-established NC-$(MX_2)_n$ system - release of entire cadmium carboxylate units has been reported[10]. Similarly, ODAm could effectively desorb as octadecylammonium sulfide, which would make CIS/ODAm an example of anion rich nanocrystals with positively charged X-type ligands. For the given ligand density of $3.8\pm0.5\,nm^{-2}$ this would require a nonstoichiometry of 0.955 ± 0.006. This figure falls outside the error range of the RBS analysis, thus confirming the conclusion on L-type binding. Nevertheless, since the error of 0.02 on the RBS analysis is only half the difference between the stoichiometric (=1.00) and the expected nonstoichiometric (0.95-0.96) charge ratio, we have further investigated the idea of tight binding of ODAm to CIS

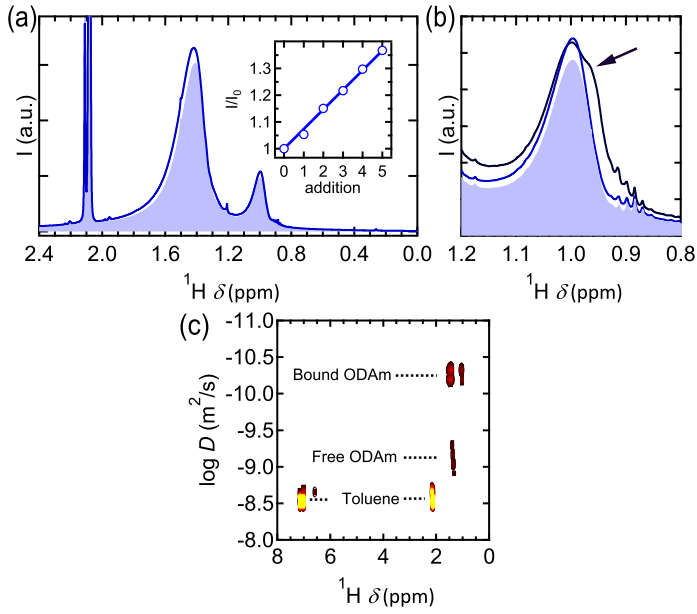

Figure 5.5: (a) Addition of ODAm to CIS/ODAm NCs in toluene-*d8*. The background shows the original spectrum with a reduced ODAm coverage, while the spectrum in blue is obtained after two additions of ODAm. Inset: plot of the signal intensity in the aliphatic region as a function of the addition of ODAm. (b) Zoom on the CH_3 region showing the spectrum of CIS/ODAm NCs after zero (background), two (blue), and five (dark blue) additions of ODAm. (c) DOSY spectrum of CIS/ODAm NCs in toluene-*d8* after the fifth addition of ODAm.

NCs by adding excess ODAm to a sample of CIS NCs with a reduced ligand coverage as obtained by purifying a sample heated at 130 °C.

The sample yields the background spectrum represented in Figure 5.5a, from which we calculate a ligand density of $2.4\pm0.3\,\mathrm{nm}^{-2}$, a number that is about 75 % of the originally measured density of $3.1\pm0.4\,\mathrm{nm}^{-2}$. Next, we added excess ODAm to this sample in steps of 7.5 % of the amount of ODAm present in the starting sample (i.e., the one with the reduced ligand coverage). The inset in Figure 5.5a confirms that the total signal intensity in the aliphatic range increases linearly with the number of additions. Moreover, by looking at the spectrum measured after the second addition shown in Figure 5.5a, it follows that

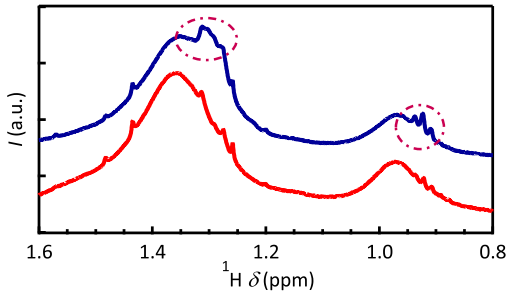

Figure 5.6: Comparison of ^{1}H NMR spectra of CIS NCs before (red) and after (blue) heating to 130 °C. Both spectra are taken at 25 °C.

the excess ODAm increases the signal intensity of the bound ODAm resonances without inducing an additional resonance. On the other hand, when the total amount of ODAm in the sample approaches the original ligand density of the NCs, a second resonance with a downfield shift gradually appears. This can be most clearly seen in Figure 5.5b, which shows a zoom on the CH_3 resonance of the initial sample and the sample after two and five additions, where the arrow indicates the additional resonance. A DOSY spectrum recorded after the fifth addition confirms that in this case ODAm species with a diffusion coefficient of both the CIS NCs and free ODAm are indeed present. Clearly, the observation that the original ligand density of CIS/ODAm NCs can be largely restored by addition of excess ODAm confirms that ODAm can self-adsorb at CIS NCs, a result that corroborates the classification of CIS/ODAm as a NC-L_n system.

An observation interesting to mention is that, even at elevated temperatures, no dynamic equilibrium exists between free and bound ODAm. After the *in situ* heating-up experiment for CIS/ODAm NCs, we measured the ^{1}H NMR spectrum of the sample after returning to room temperature. In Figure 5.6, we notice that next to the resonance of bound ODAm, an additional sharper resonance indicative for free ODAm is present. This means that not all ODAm ligands desorbed at elevated temperature readsorb on the surface of CIS NCs. This result indicates that both desorption and adsorption are thermally activated and that the room temperature stability of CIS/ODAm may be due to the activation energy for amine desorption being high rather than the amine-CIS

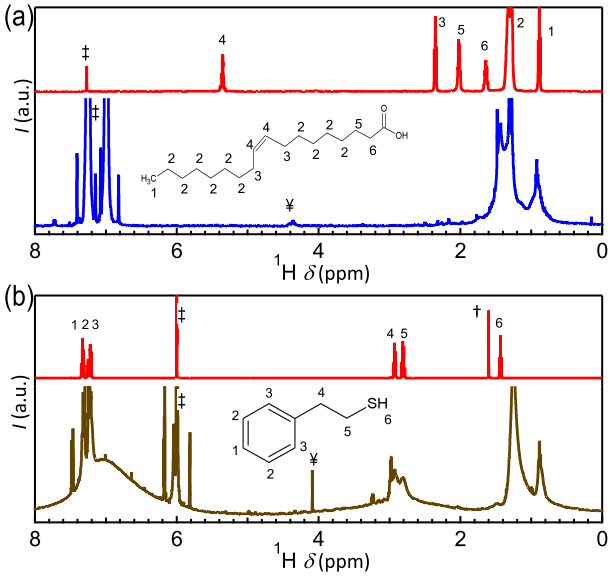

Figure 5.7: (a) ^{1}H NMR spectrum of OAc (red) and CIS NCs after performing ligand exchange procedure to OAc (blue). (b) ^{1}H NMR spectrum of PET (red) and CIS NCs after ligand exchange to PET (brown). Solvent signals are denoted by ‡, water by †, and i-propanol by ψ.

bond being unusually strong.

5.2.3 Ligand exchange reactions with $CuInS_2$ nanocrystals

The finding that CIS/ODAm nanocrystals are a NC-L_n system where the amine ligands only desorb at elevated temperature should have consequences on ligand exchange reactions and on the way they have to be executed, i.e., exchange is only expected for other L-type ligands and may require long time, high temperature exposure to the new ligand. To test this hypothesis, we studied the possible replacement of ODAm by carboxylic acids and thiols, where in particular oleic acid (OAc) and 2-phenylethanethiol (PET) were chosen since they yield resonances in the NMR spectrum well separated from those of ODAm. Both carboxylic acids and thiols are regularly used ligands in the synthesis of colloidal nanocrystals in general and $CuInS_2$ in particular and are generally reported to bind as X-type (carboxylate)[3] or as either X-type

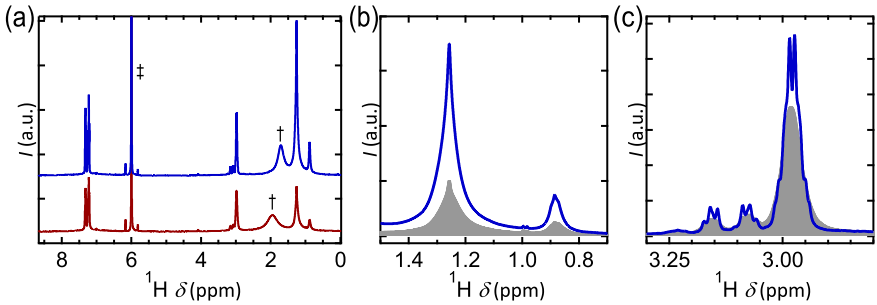

Figure 5.8: (a) ^{1}H NMR spectrum of CIS NCs stabilized by PET and ODAm before (red) and after (blue) addition of ODAm in 1,1,2,2-tetrachloroethane-*d2*. Zoom on the CH_2 and CH_3 resonances of ODAm (b) and CH_2 resonances of PET (c) with the spectrum before addition as background. Solvent signals are denoted by ‡, water by †.

(thiolate)[4] or L-type (thiol)[4]. To study possible ligand exchange reactions, well-purified dispersions of CIS NCs capped by ODAm were heated in a water- and oxygen-free atmosphere to 130 °C in the presence of a large excess of OAc or PET.

Figure 5.7 shows the 1D ^{1}H NMR spectrum of CIS NCs thus exposed to OAc in several exchange steps with NC workup in-between. Whereas a combination of broad and sharp resonances is present in the aliphatic region of the spectrum, the absence of the alkene protons of OAc - expected at around 5.5 ppm - indicates that the ligand shell hardly contains OAc moieties, if any. In contrast, two considerably broadened resonances appear in the ranges 2-4 and 6-8 ppm, respectively, in the 1D ^{1}H NMR spectrum of CIS NCs exposed to PET. Since these positions agree with the respective chemical shift of the aliphatic and aromatic protons of PET, we consider these broadened resonances as a signature of bound PET (Fig. 5.7b). Next to these broad resonances, shifted and sharper resonances are present with a chemical shift coinciding with free PET. In addition, also the broad resonances of bound ODAm at 0.9 and 1.25 ppm persist, yet the corresponding ligand density has been reduced to a mere $0.3\pm0.2\,\mathrm{nm}^{-2}$. Importantly, for a blank experiment, which involves the same heat treatment without PET exposure, the ODAm ligand density also reduces, yet is maintained at $2.2\pm0.3\,\mathrm{nm}^{-2}$.

Importantly, we show that the ligand exchange of CIS/ODAm

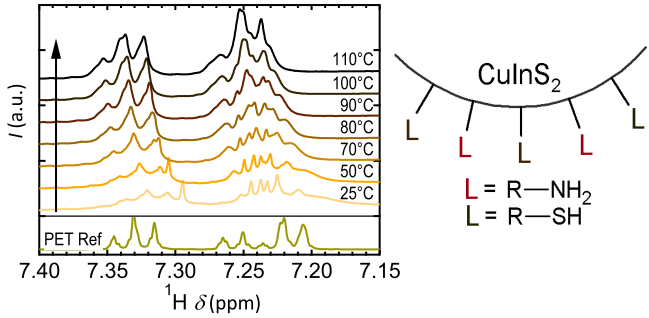

Figure 5.9: *In situ* heating-up NMR experiment on a CIS NCs dispersion stabilized by a combination of PET and ODAm in 1,1,2,2-tetrachloroethane-*d2*. The selected ppm range shows the aromatic protons of free PET superimposed on bound PET. A reference (ref) spectrum of PET in 1,1,2,2-tetrachloroethane-*d2* at 25 °C is added for comparison.

NCs to CIS/PET is reversible, by *in situ* addition of ODAm to a solution of CIS/PET NCs (Figure 5.8). Here, we used a solution of CIS/PET NCs with a residual ODAm ligand density of 0.6±0.2 nm^{-2}, and added 1 equivalent of ODAm in 1,1,2,2-tetrachloroethane-*d2*. In Figure 5.8, we notice that the signal of bound ODAm increases, indicating that ODAm binds to the surface of the NCs. Opposite from this, the CH_2 signals of free PET increase in intensity upon addition of ODAm, pointing towards a release of PET from the surface (Figure 5.8c).

To investigate the binding motif of thiols to CIS NCs, we again recorded the 1D ^{1}H NMR spectrum of a CIS NC dispersion - after exposure to PET - while raising the temperature of the sample *in situ*. Focusing on the aromatic resonances of free PET (Figure 5.9), we find that they gain intensity with increasing temperature, opposite from the general trend that signal intensities are reduced when temperature is raised. This points toward a shift of the adsorption/desorption equilibrium in the direction of desorption, which again makes clear that, in this case, thiols bind as L-type ligands to CIS NCs. Moreover, both the pronounced loss of ODAm upon exposure of CIS/ODAm to PET and the release of PET upon re-exposure to ODAm indicates that an L-by-L exchange takes place where PET and ODAm compete for the same adsorption sites. This is supported by the blank experiment, where the fraction of ODAm leaving the surface is considerably smaller than

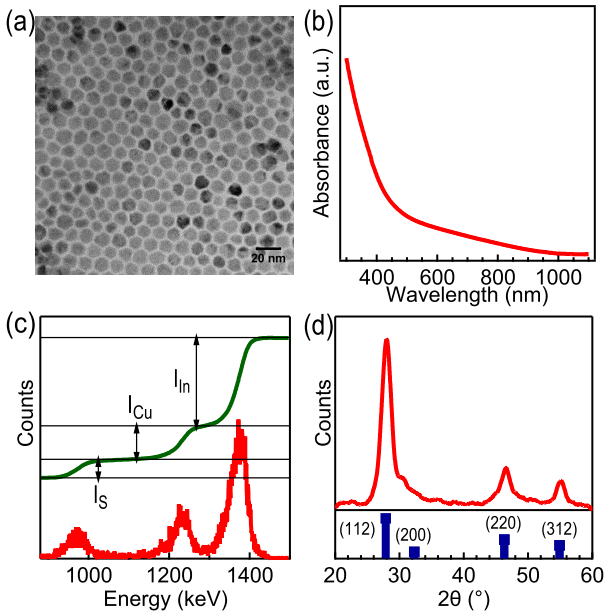

Figure 5.10: Characterization of CIS NCs synthesized using oleylamine as sole ligand. (a) TEM micrograph. (b) UV-VIS absorption spectrum. (c) RBS spectrum (red) and integrated intensities (green). (D) XRD pattern of a drop casted NC thin film.

in the case PET is added. On the other hand, the lack of bound OAc moieties after the repetitive exposure of CIS/ODAm NCs to an excess of OAc suggests that, in line with the overall stoichiometry of the nanocrystals, no X-type adsorption sites are available at the surface of CIS/ODAm NCs and that no L-by-X exchange is possible.

5.2.4 $CuInS_2$ nanocrystals synthesized with technical oleylamine

In literature, $CuInS_2$ syntheses similar to the one used here often make use of technical oleylamine (OLAm) rather than high purity octadecylamine[28–33]. As shown in Figure 5.10, replacing ODAm by OLAm results in CIS NCs that are, at first sight, similar to the ones shown in Figure 5.1. The most notable differences are the Cu:In and S:In ratios. Based on the RBS measurement, these are estimated at 1.00±0.04 and 1.54±0.12, i.e., CIS/OLAm NCs are

cation rich with a net ratio of the formal cation to anion charge of 1.30±0.10. The 1D ^{1}H NMR spectrum of a well-purified dispersion of CIS/OLAm NCs features the broadened resonances that characterize tightly bound OLAm (Figure 5.11a), a conclusion corroborated by a more detailed study using DOSY and NOESY (Figure 5.12a-b). Again, we observe strong negative NOE cross peaks and diffusion coefficient that corresponds well to that of CIS/ODAm NCs, given the similar sizes of the NC cores and the ligand shell. By performing *in situ* heating experiments, we can further confirm the similarities between OLAm and ODAm on CIS NCs (Figure 5.12c). Here, we can notice an additional, sharper resonance indicative of free OLAm when heating the sample to 130 °C. Furthermore, when staying at 130 °C for 1 h, more OLAm is being desorbed from the surface, showing that no dynamic equilibrium exists between bound and free OLAm even at elevated temperatures. After cooling down the sample, the original shape of the alkene resonance is not restored, *i.e.* not all desorbed OLAm molecules are re-adsorbed on the CIS surface. On the basis of the integration of the alkene peak at 5.6 ppm and the determination of the CIS NC concentration, we obtain a density of OLAm ligands of 3.26±0.4 nm^{-2}.

The 1D ^{1}H NMR spectrum recorded after exposing CIS/OLAm dispersions to an excess of a carboxylic acid at elevated temperature is shown in Figure 5.11b. For this experiment, 1-undecenoic acid (UDAc) was chosen since the UDAc alkene protons yield resonances well separated from those of OLAm (see Figure 5.11b, top spectrum). Opposite from CIS/ODAm, exposure of CIS/OLAm to UDAc leads to additional resonances in the 1D ^{1}H spectrum (Figure 5.11b), next to those of residual OLAm. On the basis of the correspondence with the UDAc spectrum and a DOSY study, these can be attributed to a pool of free and bound UDAc, respectively. In contrast with other ligand exchange experiments, an excess of UDAc was added to the purified CIS/OLAm dispersion just once, since subsequent steps gave rise to insufficient colloidal stability. To obtain the density of both OLAm and UDAc, we used respectively the integration of the CH_3 peak and the CH peak in the spectrum.

This leads to a ligand shell composed of 0.40±0.1 nm^{-2} UDAc and 1.1±0.2 nm^{-2} OLAm. The CIS/OLAm stoichiometry already suggests that as-synthesized CIS/OLAm NCs have in part anionic,

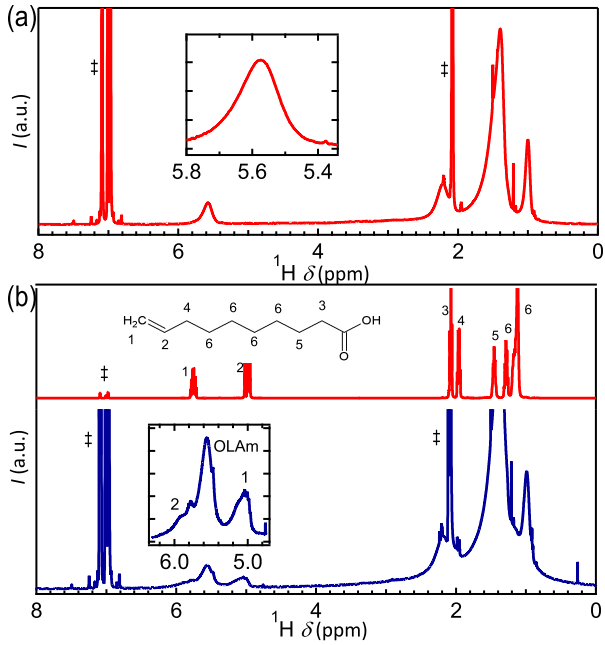

Figure 5.11: (a) ^{1}H NMR spectrum of CIS NCs capped by OLAm in toluene-*d8*. The inset zooms in on the alkene signal. (b) ^{1}H NMR spectrum of UDAc (red) and CIS NCs after performing ligand exchange to UDAc (blue) in toluene-*d8*. Inset: zoom on a region where an UDAc resonance is present, showing both bound and residual free UDAc. Solvent signals are denoted by ‡.

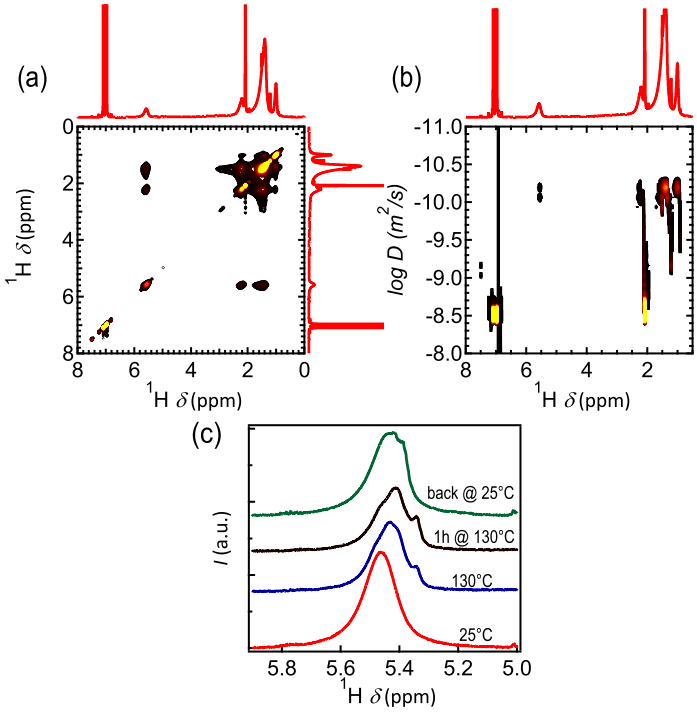

Figure 5.12: (a) NOESY NMR spectrum of CIS NCs capped with OLAm in toluene-*d8*. Here, only negative NOEs are shown. (b) DOSY NMR spectrum of the same solution. (c) ^{1}H NMR spectra taken at different stages during the heating-up experiment.

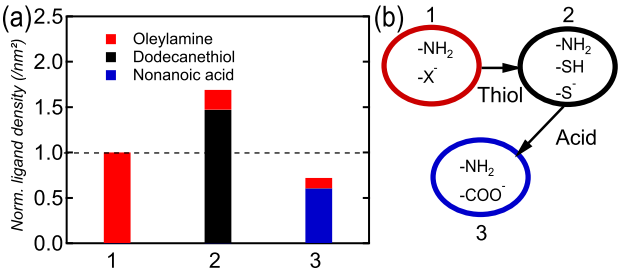

Figure 5.13: (a) Plot of normalized ligand density during successive ligand exchange steps. (b) Scheme of the experiment showing species present on the surface each step.

X-type moieties on their surface. Since they have no discernible resonances in the 1D ^{1}H spectrum, these are most likely small moieties such as OH^- or acetylacetonate, whose resonances will be excessively broadened due to the close proximity of the NC surface. Upon exposure to UDAc at high temperature, proton transfer can lead to the release of these species as H_2O or acetylacetone, two compounds easily lost by evaporation. The decrease in density of OLAm ligands can be explained by desorption at elevated temperature, followed by an incomplete readsorption and loss by purification.

To investigate the differences and similarities between CIS/ODAm and CIS/OLAm NCs in more detail, we exposed CIS/OLAm NCs in consecutive steps to dodecanethiol (DDT) and nonanoic acid (NAc) at elevated temperature and determined the ligand density after each step. In this case, the alkene resonance of OLAm and the overlapping methyl resonance of OLAm, DDT, and NAc were used to determine the amount of bound OLAm and the total amount of bound ligands, respectively. In Figure 5.13a, we plot the thus determined normalized ligand density, i.e., the actual ligand density relative to the initial one, after each exchange step, where 1 corresponds to as-synthesized OLAm, 2 to CIS NCs after exposure to DDT, and 3 to CIS NCs after exposure to NAc. In line with the results of CIS/OLAm after exposure to PET, one sees that, after exposure to DDT, most of the OLAm is lost. On the other hand, the total ligand density rises by more than 60 %. Subsequent exposure to NAc further reduces the amount of OLAm but also brings down the total ligand density to about 60 % of the original density. These observations can be interpreted starting

again from the assumption that as-synthesized CIS/OLAm NCs accommodate next to L-type OLAm ligands also X-type moieties on their surface. While we were not able to identify these X-type moieties, we attribute the difference in surface chemistry between CIS/ODAm and CIS/OLAm NCs to the impurities present in technical OLAm, rather than the OLAm itself, since it is shown that OLAm provides a similar L-type ligand as ODAm for CIS NCs. The considerable increase of ligand density after exposure to DDT indicates that, in this case, DDT not only replaces OLAm as an L-type ligand - similar to CIS/ODAm - but also binds to the X-type sites as dodecanethiolate (DDT^-). During the exposure to NAc, the L-type DDT ligands are lost by desorption and the X-type DDT^- is replaced by NAc^-. In line with this reasoning, the ligand loss after NAc exposure indeed corresponds to the original density of L-type ligands. To summarize the results obtained in the characterization and ligand exchange procedures of CIS/OLAm NCs, we illustrate their behaviour by the following reaction equations:

$$\mathrm{X{-}NC{-}(NH_2R)_x} \xrightarrow{\Delta} \mathrm{X{-}NC{-}(NH_2R)_{x-y}} + \mathrm{yRNH_2} \quad (5.1)$$

$$\mathrm{X{-}NC{-}NH_2R + RSH} \xrightarrow{\Delta} \mathrm{RS{-}NC{-}SHR + RNH_2 + HX\uparrow} \quad (5.2)$$

$$\mathrm{RS{-}NC{-}SHR + RCOOH} \xrightarrow{\Delta} \mathrm{RCOO{-}NC{-}SHR + RSH} \quad (5.3)$$

In equation 5.1, we depict the partial release of L-type OLAm induced by heating the CIS/OLAm NC solution. This equation denotes the results presented in Figure 5.12c, and is similar for CIS/ODAm NCs with the exception of the X-type impurity present on the CIS/OLAm NCs. Heating CIS/OLAm NCs in the presence of an excess of thiols induces the release of both X-type impurities and L-type OLAm, according to equation 5.2. Note that for simplicity's sake we assume the ligand exchange reactions to be complete, even though we clearly measure residual OLAm after several exchange steps (Figure 5.13). We assume the exchange of X-type impurity towards X-type thiol (RS^-) is accompanied by a proton transfer of the thiol towards the impurity,

most likely resulting in the impurity released as a gas. Exchanging thiol-capped CIS NCs towards acids results in a proton transfer from the acid to the X-type bound thiol, without acid-induced exchange of the L-type bound thiol (equation 5.3).

5.3 Conclusions

We analyzed the surface chemistry of CIS NCs synthesized using amines and explored possible ligand exchange strategies. By employing the solution NMR toolbox for nanocrystal surface chemistry analysis, which includes 1D ^{1}H NMR, NOESY, and DOSY in combination with *in situ* heating up experiments, we concluded that the surface of as-synthesized CIS NCs consists of L-type, tightly bound amines. This is in contrast with the dynamic stabilization of amines typically found in other NC systems. Importantly, by giving a first example of stoichiometric nanocrystals stabilized by L-type ligands, these results complete the picture that has emerged on the surface chemistry of semiconductor nanocrystals in apolar environments. Moreover, a relatively straightforward approach to distinguish L-type from X-type binding by combining *in situ* heating up with solution NMR spectroscopy is introduced. The strong binding of L-type ligands has the consequence that exchanging the original amine ligands for others ligands requires relatively high temperatures and successive exchange steps, along with the ability of the new ligand to bind as L-type. We have demonstrated this by performing ligand exchange reactions toward acids and thiols, where only thiols could be found on the NC surface after several ligand exchange steps. Additionally, we highlight that the use of technical grade OLAm, which is widely used in CIS NC synthesis, leads to nonstoichiometric NCs capped by a combination of L-type OLAm and X-type impurities. This finding stresses the importance of a careful analysis of the surface chemistry of as-synthesized NCs in general, in order to rationalize ligand exchange strategies.

Chapter VI

Stabilizing colloidal nanocrystals with inorganic ligands

The layer of organic ligands around the surface of colloidal nanocrystals originating from the synthesis determines their solubility. For applications where, more often than not, dried nanocrystal solids are required -*e.g.* a thin film- these organic ligands can hinder the performance since the length of typically used hydrocarbon molecules is in the order of magnitude of the NC core diameter[34–36]. This includes charge transport between adjacent nanocrystals and the incomplete loss upon annealing. Therefore, an interesting concept to investigate with respect to sintering CIGS NCs is the post-synthesis ligand exchange to inorganic ligands (scheme in Figure 6.1). The method of exchanging organic ligands on colloidal NCs for inorganic ligands is based on the work of Nag *et al*[37]. The authors have shown that a wide variety of colloidal NCs can be stabilized by anions such as S^{2-}, Se^{2-} and OH^{-}, while retaining the optical and structural properties of the NCs. Moreover, they have shown that coupling between adjacent NCs in a NC solid is greatly enhanced due to reduced inter particle spacing.

In this chapter, we adapt the method of Nag *et al* and apply it to ternary and binary NCs of the $CuInS(e)_2$ system, using sulfide and selenide ligands. We optimize these methods and verify the exchange and colloidal stability of the resulting dispersions. In a later stage (see Part 3), the annealing behaviour of thin films

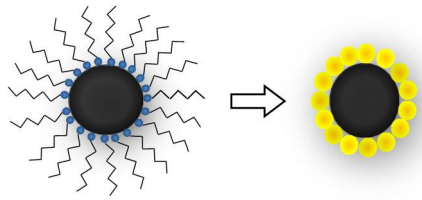

Figure 6.1: Schematic representation of a NC with conventional organic ligands (left) and inorganic ligands (right).

resulting from these dispersions is analyzed, where we also pay attention to the removal of these inorganic ligands with respect to residual impurities in the semiconductor thin film.

6.1 Experimental

S^{2-} exchange. We employ $(NH_4)_2S$ as a sulfur source, rather than Na_2S/K_2S[37] which could introduce Na and K in the final thin film after annealing. For a typical ligand exchange to sulfide anions, we used 250 µL of a stock solution of CIS NCs (synthesis described in section 2.1.1) with a concentration of 20 µM. The NCs were precipitated with ethanol and redispersed in toluene twice. After the last centrifugation step, the CIS NCs were dispersed in 2 mL of toluene. Next, 2 mL of formamide and 100 µL of $(NH_4)_2S$ (20 w% in H_2O) are added and the resulting 2-phase system is stirred vigorously at room temperature. *Caution: Hydrazine -even as an aqueous solution- is toxic and should be handled using appropriate protective equipment!*. After 10 min, the black CIS NCs have transferred to the bottom formamide phase. Both phases are separated, and toluene is added to the CIS NCs in formamide. This is meant to extract remaining OLAm molecules in the formamide phase. The resulting mixture is stirred and the extraction with toluene is repeated 4 times. The CIS NCs in formamide are precipitated using i-PrOH, and collected by centrifugation. The resulting pellet can then be redispersed in formamide or DMSO.

HSe^-/Se^{2-} exchange. In order to cap CIS NCs with selenide anions, we developed a novel method. Rather than using expensive/hazardous salts such as Na_2Se or $(NH_4)_2Se$, we prepare selenide anions by a reduction from elemental selenium. Two strategies are explored, namely the reduction by $NaBH_4$ and hydrazine

hydrate, as shown in equation 6.1 and 6.2, respectively.

$$4\mathrm{NaBH_4} + 2\,\mathrm{Se} \longrightarrow 2\,\mathrm{NaHSe} + 2\,\mathrm{B_2H_6}\uparrow + \mathrm{H_2}\uparrow \tag{6.1}$$

$$5\,\mathrm{N_2H_4 \cdot H_2O} + 2\,\mathrm{Se} \longrightarrow 2\,(\mathrm{N_2H_5})_2\mathrm{Se} + 5\,\mathrm{H_2O} + \mathrm{N_2}\uparrow \tag{6.2}$$

For NaHSe, 0.25 mmol (0.020 g) elemental Se powder is combined with 0.50 mmol (0.019 g) $NaBH_4$ in 2.5 mL DMSO in a nitrogen-filled glove box. The resulting solution is stirred until the Se powder disappears (±15 min) and a colorless solution is formed. To produce hydrazinium selenide, 1 mmol Se (0.079 g) is combined with 2.5 mmol $N_2H_4 \cdot H_2O$ (130 µL, 65 % N_2H_4) in 1.87 mL DMSO. The mixture is now stirred for 10 min at room temperature and a dark red solution is obtained.

The exchange for selenide ligands is performed as following. A solution of purified CIS NCs is prepared as described above, dissolved in 2 mL hexane and added to 2 mL DMSO. 75 µL of $(N_2H_5)_2Se$ solution or 300 µL of NaHSe is added to initiate the ligand exchange. The purification and seperation of CIS NCs is done as described above.

^{1}H NMR analysis. NMR samples are made of the purified dispersion of CIS NCs in toluene by drying them with a strong nitrogen flow and redispersing them in toluene-*d8*. During the 2-phase exchange, all toluene phases are collected, dried and dissolved in toluene-*d8* to obtain an NMR sample. The NMR sample of the CIS NCs after the transfer to formamide is made by precipitation with i-PrOH, and drying the resulting pellet in vacuum, followed by dispersing it in DMSO-*d6*. NMR measurements are performed as described in section V.

ζ-potential and DLS measurements. For Dynamic Light Scattering (DLS) and ζ-potential measurements a Malvern Nano ZS was used in backscattering mode (173°).

6.2 Results and discussion

6.2.1 Verification of ligand exchange

To demonstrate the successful transfer from an apolar solvent to a polar solvent after exchanging OLAm ligands for inorganic li-

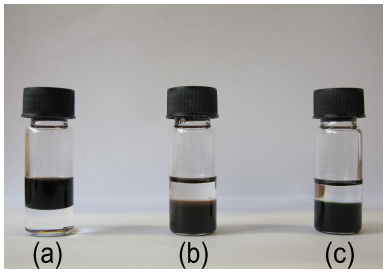

Figure 6.2: (a) CIS/OLAm NCs dissolved in toluene. After ligand exchange for $(N_2H_5)_2Se$ (CIS NCs) (b) and $(NH_4)_2S$ (CuS NCs) (c). Each vial holds a toluene (top) and formamide (bottom) phase.

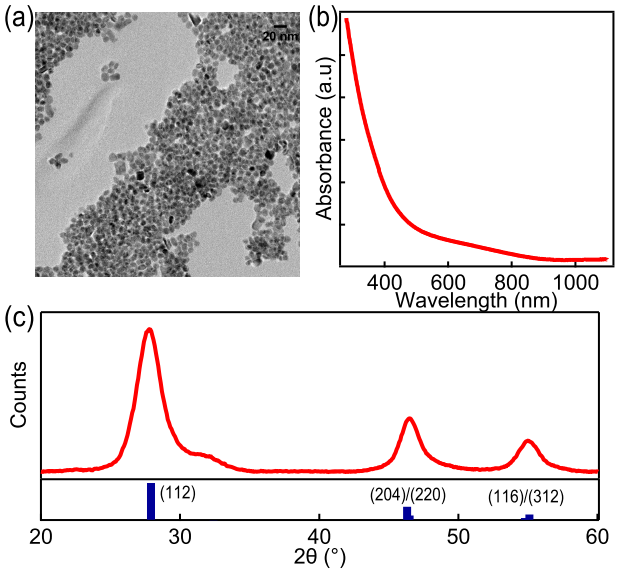

Figure 6.3: Characterization of CIS NCs with $(NH_4)_2S$ ligands. (a) TEM image. (b) UV-VIS absorption spectrum in DMSO. (c) XRD pattern of a drop casted thin film.

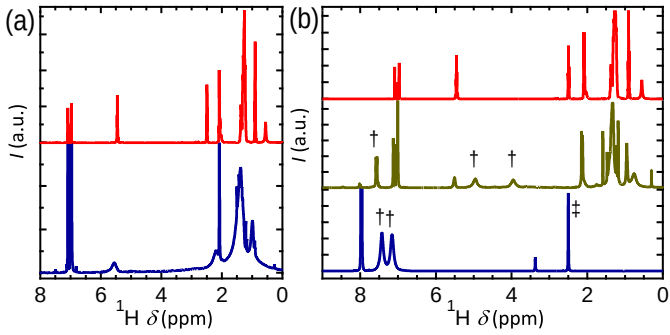

Figure 6.4: ^{1}H NMR analysis of the ligand exchange process. (a) Comparison of OLAm (top) and CIS NCs with OLAm (bottom) in toluene-*d8*. (b) Toluene phase after transfer of CIS NCs (middle) and formamide phase holding CIS NCs (bottom) in DMSO-*d6*. Again, the ^{1}H NMR spectrum of OLAm (top) is added for comparison. Formamide peaks are denoted by †, and the DMSO peak by ‡.

gands, Figure 6.2 shows vials containing NCs and both toluene (top phase) and formamide (bottom phase). We found that an exchange of OLAm for sulfide or selenide salts is possible in the case of ternary $CuInS(e)_2$ NCs and binary sulfides. The addition of these salts to binary selenide NCs on the other hand leads to the dissolution of the NCs. In addition, we noted that the synthesis of selenide anions requires an inert atmosphere, since they are prone to oxidation in air.

In Figure 6.3, we show the characterization of purified CIS NCs after a ligand exchange for $(NH_4)_2S$. The results in terms of particle morphology, UV-VIS absorption and crystal structure coincides with as-synthesized CIS NCs (see 2.1.2). Based on the TEM micrograph, we notice a reduced inter particle spacing which we attribute to the decreased length of $(NH_4)_2S$ compared to OLAm.

We monitored the ligand exchange process using ^{1}H solution NMR. The NMR spectrum of as-synthesized and purified CIS NCs is shown and compared with the spectrum of OLAm in Figure 6.4a. We notice the typical broadening and chemical shift of the ligands bound to CIS NCs compared to free ligands. An interesting resonance is the alkene resonance of the OLA molecules, since it is well-separated from other signals (5.55 ppm). For these 8 nm CIS NCs, we measured a ligand density of 2.9 nm^{-2}. During the ligand exchange procedure from the toluene phase to a formamide

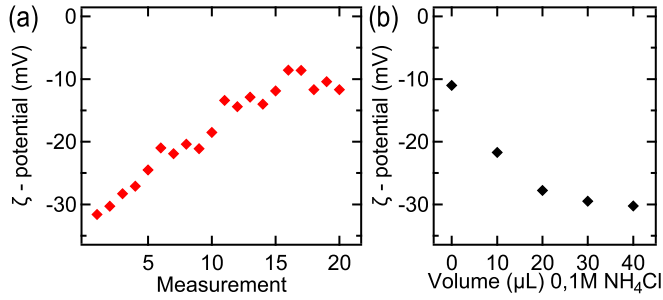

Figure 6.5: (a) Evolution of ζ-potential over time of a CIS NC solution capped with $(NH_4)_2S$ in DMSO. The average time of each measurement is 5 min.(b) Evolution of ζ-potential by addition of NH_4Cl.

phase, we collected and dried all toluene phases. The resulting product was dissolved in toluene-*d8*, and the corresponding NMR spectrum is shown in Figure 6.4b (middle). We assigned the resonances in this spectrum to toluene, OLAm and formamide. Importantly, the ^{1}H NMR spectrum of the CIS NCs in the formamide phase (measured in DMSO-*d6*) shows no signs of OLAm. Here, we can distinguish peaks from DMSO, i-PrOH and formamide. We can conclude that during the phase transfer executed as described above, the original OLAm ligands are completely stripped off the NCs.

6.2.2 Colloidal stability

By exchanging native organic ligands for inorganic ligands, the original stabilization of the NC dispersion by sterical hindrance is replaced by a stabilization by charge. In that case, colloidal stability originates from the repulsion between equally charged nanocrystals. This type of stability is typically characterized by the ζ-potential, which is the difference between the electrostatic potential at the slip plane between the nanocrystal and the solution and the potential at infinity, *i.e.*, in the bulk of the solution[38]. Several literature reports mention an absolute value of the ζ-potential as 30 mV to be critical[39,40] at room temperature, above which colloids are considered stable. This value should be seen as an indication rather as a threshold, since often other parameters have their independent influence on the stability (particle size/shape, concentration,..).

Figure 6.5a shows the evolution of the ζ-potential of a 5 µM CIS NC solution stabilized by $(NH_4)_2S$ in DMSO as a function of time. Here, the ζ-potential of the sample is measured in consecutive scans with an average measurement time of 5 min. Right after the ligand exchange, a negative ζ-potential of -32 mV is found, indicating that the surface is enriched in negative charges that originate most likely from adsorbed sulfide anions. However, as shown in the graph, the absolute value of the ζ-potential decreases over time, which reflects a decrease of colloidal stability. We suspect that this is due the loss of $(NH_4)_2S$:

$$(NH_4)_2S \longrightarrow NH_3\uparrow + H_2S\uparrow \tag{6.3}$$

A reduction of the overall $(NH_4)_2S$ concentration will indeed induce a steady release of sulfide anions from the NC surface, thus reducing the ζ-potential. When kept in a closed vial, this process is slowed down, yet even then, we find that NCs settle out from solution approximately a day after ligand exchange for $(NH_4)_2S$. While this is inconvenient from a practical perspective, we noticed that the intermediate colloidal stability of NCs capped with $(NH_4)_2S$ has an impact on the morphology of an as-deposited layer, as they are much more prone to cracking compared to NCs with organic ligands.

We managed to increase the colloidal lifetime of CIS and CuS NCs by addition of chloride salts. As shown in Figure 6.5b, addition of NH_4Cl to a relatively unstable solution of CIS NCs in DMSO - starting at a ζ-potential of -11 mV - leads to an increasingly more negative ζ-potential. This indicates that the surface of the CIS NCs are enriched in negative charges, which means that in this case Cl^- ions are in close proximity of the surface of the NCs, leading to increased colloidal stability. Note that we discuss the removal of chlorine, and its possible impact on the semiconductor properties of the final layer in Chapter IX;

Taking into account the increased stability of CIS NCs by addition of Cl^- ions, we developed a hybrid ink in which the salt $InCl_3$ serves as source of In and Cl^-. The ink is composed of $CuInS_2$ NCs, CuS NCs and $InCl_3$, making the stoichiometry of the final layer easily adjustable. The aim of using CuS NCs is to make the sintering during thermal processing more reactive, as described in Part 3. In Figure 6.6, we compare the stability of two inks of $CuInS_2$ and CuS NCs with $(NH_4)_2S$ ligands in DMSO in which

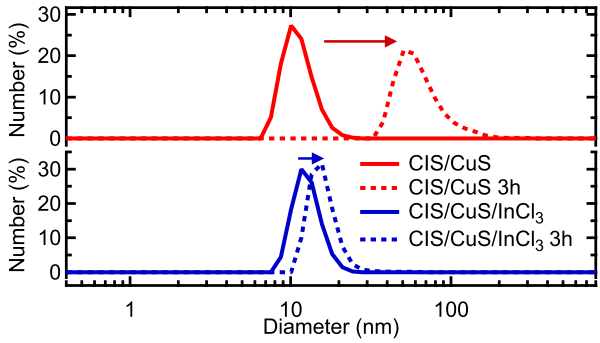

Figure 6.6: DLS measurements of a mixture of $CuInS_2$ and CuS NCs capped with $(NH_4)_2S$ (top) and the same mixture with addition of $InCl_3$ (bottom).

one contains $InCl_3$. We see that the measurement of the fresh inks give rise to a distribution of sizes in agreement with the NCs used in this work. After 2 h, as was indicated by the decreased absolute values for ζ-potential (Figure 6.5), the distribution is shifted to larger values. In contrast, the ink that contains $InCl_3$ shows a much lower shift in the same time frame. We attribute this to the increased stabilization by Cl^- anions, as was demonstrated in Figure 6.5.

6.3 Conclusions

In this chapter, we explored the ability to exchange organic ligands to inorganic ligands on CIS NCs. The inorganic ligands were chosen by keeping the application in mind: the formation of dense CIGS layers by annealing of nanocrystal precursors. Therefore, our focus is put on sulfide and selenide salts with counter ions which provide no additional impurities by anticipating them to be volatile at relatively low temperatures - which is investigated in part 3. We demonstrated a successful exchange, by measuring a complete removal of organics on the surface of NCs. We investigated the colloidal stability of CIS NCs capped by $(NH_4)_2S$ by means of ζ-potential and DLS measurements. Here, we show that these colloids exhibit a rather poor stability, which we attribute to the decomposable $(NH_4)_2S$ salt. A possible solution that substantially prolongs their stability is found in the use of chlorine salts, which can be easily added to these polar dispersions. Given

by increased negative ζ-potential values, we conclude that chlorine binds to the nanocrystal surface providing increased stability. DLS measurements confirm that this leads to a longer shelf-life of these mixtures of NCs and salts. The addition of chlorine salts in the form of $InCl_3$ can be used to easily tune the stoichiometry and can have a positive impact on the morphology of an as-deposited precursor layer.

Bibliography

[1] Klem, E. J. D.; Shukla, H.; Hinds, S.; MacNeil, D. D.; Levina, L.; Sargent, E. H. Impact of dithiol treatment and air annealing on the conductivity, mobility, and hole density in PbS colloidal quantum dot solids. *Applied Physics Letters* **2008**, *92*, 212105.

[2] Zarghami, M. H.; Liu, Y.; Gibbs, M.; Gebremichael, E.; Webster, C.; Law, M. p-Type PbSe and PbS quantum dot solids prepared with short-chain acids and diacids. *ACS nano* **2010**, *4*, 2475–85.

[3] Fritzinger, B.; Capek, R. K.; Lambert, K.; Martins, J. C.; Hens, Z. Utilizing self-exchange to address the binding of carboxylic acid ligands to CdSe quantum dots. *Journal of the American Chemical Society* **2010**, *132*, 10195–201.

[4] Owen, J. S.; Park, J.; Trudeau, P.-E.; Alivisatos, a. P. Reaction chemistry and ligand exchange at cadmium-selenide nanocrystal surfaces. *Journal of the American Chemical Society* **2008**, *130*, 12279–81.

[5] Hassinen, A.; Gomes, R.; De Nolf, K.; Zhao, Q.; Vantomme, A.; Martins, J. C.; Hens, Z. Surface Chemistry of CdTe Quantum Dots Synthesized in Mixtures of Phosphonic Acids and Amines: Formation of a Mixed Ligand Shell. *The Journal of Physical Chemistry C* **2013**, *117*, 13936–13943.

[6] Moreels, I.; Justo, Y.; Geyter, B. D. Size-tunable, bright, and stable PbS quantum dots: a surface chemistry study. *Acs Nano* **2011**, 2004–2012.

[7] Moreels, I.; Fritzinger, B.; Martins, J. C.; Hens, Z. Surface chemistry of colloidal PbSe nanocrystals. *Journal of the American Chemical Society* **2008**, *130*, 15081–6.

[8] Cros-Gagneux, A.; Delpech, F.; Nayral, C.; Cornejo, A.; Coppel, Y.; Chaudret, B. Surface chemistry of InP quantum dots: a comprehensive study. *Journal of the American Chemical Society* **2010**, *132*, 18147–57.

[9] Moreels, I.; Martins, J. C.; Hens, Z. Ligand adsorption/desorption on sterically stabilized InP colloidal nanocrystals: observation and thermodynamic analysis. *Chemphyschem : a European journal of chemical physics and physical chemistry* **2006**, *7*, 1028–31.

[10] Anderson, N. C.; Hendricks, M. P.; Choi, J. J.; Owen, J. S. Ligand exchange and the stoichiometry of metal chalcogenide nanocrystals: spectroscopic observation of facile metal-carboxylate displacement and binding. *Journal of the American Chemical Society* **2013**, *135*, 18536–48.

[11] Anderson, N.; Owen, J. Soluble, Chloride-Terminated CdSe Nanocrystals: Ligand Exchange Monitored by ^{1}H and ^{3}1P NMR Spectroscopy. *Chemistry of Materials* **2012**, *25*, 69–76.

[12] Hens, Z.; Martins, J. A solution NMR toolbox for characterizing the surface chemistry of colloidal nanocrystals. *Chemistry of Materials* **2013**, *25*, 1211–1221.

[13] Yao, R.-Y.; Zhou, Z.-J.; Hou, Z.-L.; Wang, X.; Zhou, W.-H.; Wu, S.-X. Surfactant-free $CuInS_2$ nanocrystals: an alternative counter-electrode material for dye-sensitized solar cells. *ACS applied materials & interfaces* **2013**, *5*, 3143–8.

[14] Lauth, J.; Marbach, J.; Meyer, A.; Dogan, S.; Klinke, C.; Kornowski, A.; Weller, H. Virtually Bare Nanocrystal Surfaces: Significantly Enhanced Electrical Transport in $CuInSe_2$ and $CuIn_{1-x}Ga_2Se_2$ Thin Films upon Ligand Exchange with Thermally Degradable 1-Ethyl-5-Thiotetrazole. *Advanced Functional Materials* **2013**, *24*, 1081–1088.

[15] Stolle, C. J.; Panthani, M. G.; Harvey, T. B.; Akhavan, V. a.; Korgel, B. a. Comparison of the photovoltaic response of oleylamine and inorganic ligand-capped $CuInSe_2$ nanocrystals. *ACS applied materials & interfaces* **2012**, *4*, 2757–61.

[16] Guo, Q.; Ford, G. Ink formulation and low temperature incorporation of sodium to yield 12% efficient Cu(In, Ga)(S, $Se)_2$ solar cells from sulfide nanocrystal inks. *Progress in Photovoltaics: Research and Applications* **2013**, *21*, 64–71.

[17] Gomes, R.; Hassinen, A.; Szczygiel, A.; Zhao, Q.; Vantomme, A.; Martins, J. C.; Hens, Z. Binding of Phosphonic Acids to CdSe Quantum Dots: A Solution NMR Study. *The Journal of Physical Chemistry Letters* **2011**, *2*, 145–152.

[18] Carbone, L. et al. Synthesis and micrometer-scale assembly of colloidal CdSe/CdS nanorods prepared by a seeded growth approach. *Nano letters* **2007**, *7*, 2942–50.

[19] Findeisen, M.; Brand, T.; Berger, S. A 1 H-NMR thermometer suitable for cryoprobes. *Magnetic resonance in Chemistry* **2007**, *45*, 175–178.

[20] Connell, M. a.; Bowyer, P. J.; Adam Bone, P.; Davis, A. L.; Swanson, A. G.; Nilsson, M.; Morris, G. a. Improving the accuracy of pulsed field gradient NMR diffusion experiments: Correction for gradient non-uniformity. *Journal of magnetic resonance* **2009**, *198*, 121–31.

[21] Wider, G.; Dreier, L. Measuring protein concentrations by NMR spectroscopy. *Journal of the American Chemical Society* **2006**, *128*, 2571–2576.

[22] Sinnaeve, D. The Stejskal-Tanner equation generalized for any gradient shape - an overview of most pulse sequences measuring free diffusion. *Concepts in Magnetic Resonance Part A* **2012**, *2*, 39–65.

[23] D. Ricard, M. Ghanassi, M. S.-K. Dielectric confinement and the linear and nonlinear optical properties of semiconductor-doped glasses. *Optics Communications* **1994**, *108*, 311–318.

[24] Alonso, M.; Wakita, K.; Pascual, J.; Garriga, M.; Yamamoto, N. Optical functions and electronic structure of $CuInSe_2$, $CuGaSe_2$, $CuInS_2$, and $CuGaS_2$. *Physical Review B* **2001**, *63*, 1–13.

[25] Fritzinger, B.; Moreels, I.; Lommens, P.; Koole, R.; Hens, Z. In Situ Observation of Rapid Ligand Exchange in Colloidal Nanocrystal Suspensions Using Transfer NOE Nuclear. *Journal of the American Chemical Society* **2009**, *131*, 3024–3032.

[26] Hassinen, A.; Moreels, I.; de Mello Donegaa, C.; Martins, J. C.; Hens, Z. Nuclear Magnetic Resonance Spectroscopy Demonstrating Dynamic Stabilization of CdSe Quantum Dots by Alkylamines. *The Journal of Physical Chemistry Letters* **2010**, *1*, 2577–2581.

[27] Hassinen, A.; Moreels, I.; De Nolf, K.; Smet, P. F.; Martins, J. C.; Hens, Z. Short-chain alcohols strip X-type ligands and quench the luminescence of PbSe and CdSe quantum dots, acetonitrile does not. *Journal of the American Chemical Society* **2012**, *134*, 20705–12.

[28] Chung, W.; Jung, H.; Lee, C. H.; Park, S. H.; Kim, J.; Kim, S. H. Synthesis and Application of Non-Toxic $ZnCuInS_2$/ZnS Nanocrystals for White LED by Hybridization with Conjugated Polymer. *Journal of The Electrochemical Society* **2011**, *158*, 1218–1220.

[29] Guo, Q.; Kim, S.; Kar, M.; Shafarman, W. Development

of $CuInSe_2$ nanocrystal and nanoring inks for low-cost solar cells. *Nano letters* **2008**, *8*, 1–6.

[30] Guo, Q.; Ford, G. G. M.; Hillhouse, H. W. H.; Agrawal, R. Sulfide nanocrystal inks for dense $Cu(In_{1-x}Ga_x)(S_{1-y}Se_y)_2$ absorber films and their photovoltaic performance. *Nano letters* **2009**, *9*, 3060–5.

[31] Panthani, M. G.; Akhavan, V.; Goodfellow, B.; Schmidtke, J. P.; Dunn, L.; Dodabalapur, A.; Barbara, P. F.; Korgel, B. A. Synthesis of $CuInS_2$, $CuInSe_2$, and $Cu(In_xGa_{1-x})Se_2$ (CIGS), Nanocrystal Inks for Printable Photovoltaics. *Journal of American Chemical Society* **2008**, *2*, 16770–16777.

[32] Tang, J.; Hinds, S.; Kelley, S.; Sargent, E. Synthesis of Colloidal $CuGaSe_2$, $CuInSe_2$, and $Cu(InGa)Se_2$ Nanoparticles. *Chemistry of Materials* **2008**, *20*, 6906–6910.

[33] Kruszynska, M.; Borchert, H.; Parisi, J.; Kolny-Olesiak, J. Synthesis and shape control of $CuInS_2$ nanoparticles. *Journal of the American Chemical Society* **2010**, *132*, 15976–86.

[34] Johnston, K. W.; Pattantyus-Abraham, A. G.; Clifford, J. P.; Myrskog, S. H.; MacNeil, D. D.; Levina, L.; Sargent, E. H. Schottky-quantum dot photovoltaics for efficient infrared power conversion. *Applied Physics Letters* **2008**, *92*, 151115.

[35] Peng, X. An essay on synthetic chemistry of colloidal nanocrystals. *Nano Research* **2010**, *2*, 425–447.

[36] Deka, S.; Genovese, A.; Zhang, Y.; Miszta, K.; Bertoni, G.; Krahne, R.; Giannini, C.; Manna, L. Phosphine-free synthesis of p-type copper(I) selenide nanocrystals in hot coordinating solvents. *Journal of the American Chemical Society* **2010**, *132*, 8912–4.

[37] Nag, A.; Kovalenko, M. V.; Lee, J.-S.; Liu, W.; Spokoyny, B.; Talapin, D. V. Metal-free inorganic ligands for colloidal nanocrystals: S^{2-}, HS^-, Se^{2-}, HSe^-, Te^{2-}, HTe^-, $TeS_3{}^{2-}$, OH^-, and $NH_2{}^-$ as surface ligands. *Journal of the American Chemical Society* **2011**, *133*, 10612–20.

[38] Keck, C. M. *PhD Thesis*, Freie Universität Berlin, 2006.

[39] Müller, R. H.; Jacobs, C. Buparvaquone mucoadhesive nanosuspension: Preparation, optimisation and long-term stability. *International Journal of Pharmaceutics* **2002**, *237*, 151–161.

[40] Sharma, P.; Brown, S.; Walter, G.; Santra, S.; Moudgil, B. Nanoparticles for bioimaging. *Advances in Colloid and Interface Science* **2006**, *123-126*, 471–485.

Part 3: Film formation and transformation in dense CIS layers

Introduction

Colloidal NCs offer a distinct way to form semiconductor thin films compared to conventional vacuum based deposition. This film can be either one of the active parts in the final device - used for light absorption or charge carrier transport - or it can be an intermediate step in the formation of a dense, semiconductor thin film. In the former case, the long chain organic ligands originating from the synthesis make up insulating barriers that separate adjacent NCs and hinder the transport of charge carriers. Typical approaches to enhance charge carrier mobilities in NC thin films or hybrid composite devices make use of a post-synthesis ligand exchange step to decrease inter particle spacing. By using short chain ligands[1–4] or bridging ligands[2–8], one is able to improve the performance of NC based solar cells, photodetectors or transistors. Next to ligand exchange, an annealing step is meant to remove unwanted compounds. However, since the NC properties must be preserved during annealing, this requires the use of thermally labile ligands that decompose at relatively low temperatures, where NC sintering does not yet occur.

When the final goal is the formation of a dense thin film on the other hand, annealing is indispensable to induce sintering. Typical examples here are found in the field of thin-film photovoltaics. Apart from the aforementioned use for CIGS absorber layers, this approach has been used for $Cu_2ZnSn(S,Se)_4$ (CZT(S,Se))[9,10] and CdTe[11]. In the case of CIGS and CZT(S,Se) films, a possible strategy to increase the reactivity of the system during annealing is the use of binary NCs. Here, mixtures of binary NCs transform towards the (qua)ternary compound instead of sintering, while the composition of the final film can be easily adjusted. A complication in the transformation of NCs to dense thin films lies again in the surface chemistry of the NCs. The long chain organic ligands can hamper the transformation since they induce a sig-

nificant weight loss upon annealing resulting in cracks, possibly combined with undesired carbon deposits[12].

To avoid these issues, a possible alternative is the use of colloidal NCs stabilized with short chain or thermally labile ligands by means of a post-synthesis ligand exchange step. In the case of metal sulfide or metal selenide semiconductors, a more straightforward approach seems the use of NCs stabilized by chalcogenide ligands, such as S^{2-} or Se^{2-}, as recently introduced by Nag et al[13]. These ligands occupy a smaller volume and should prevent any contamination with elements foreign to the final semiconductor compound. In the case of CIGS and CZT(S,Se), NC stabilization with chalcogenide ligands would have the additional advantage of creating an excess of chalcogen species in a NC layer prior to annealing. This could possibly be exploited to avoid the cumbersome gas-phase sulfurization or selenization step that is typically required for grain growth and thus device integration in a highly efficient CIGS-CZTSSe solar cell[14].

In this part, we explore the formation of dense CISe thin films obtained by selenization of ternary and mixtures of binary NCs. We compare the differences in reactivities between the precursor systems with respect to composition in terms of crystal growth. Next, the focus is put on the relation between the surface chemistry of the NCs and the transformation behaviour. Here, we highlight the importance of leftover impurities in the final semiconductor layer and explore the transformation behaviour of CIS NCs with inorganic sulfide ligands. In a final chapter, we discuss strategies to improve the morphology of as-deposited NC layers and use molecular precursors as an approach towards absorber-quality CISe layers. We demonstrate the potential of our precursors for $CuInSe_2$ thin film solar cells. Additionally, we discuss the option to include an excess of selenium in the precursor ink in an attempt to circumvent the need for gas-phase selenization.

Chapter VII

Comparison of precursor systems

In this chapter, we compare the annealing behaviour of the various ternary and binary colloidal NCs of the CIGS system synthesized in Part 1. NC thin films are annealed or selenized towards dense $CuInSe_2$ layers and the reactivity of the NCs is evaluated by the degree of sintering. As mentioned before, large CIGS crystals are preferred in a photovoltaic device. The characterization by *in situ* XRD and the analysis of the patterns is performed by Boris Capon, supervised by Prof. Dr. Christophe Detavernier at the Departement of Solid-State Sciences at Ghent University. Next to comparing the reactivity of the different NC systems, we analyze and design strategies to reduce the amount of impurities originating from the ligands. This is realized by comparing different ligands on one precursor system, namely $CuInS_2$ NCs, and we establish a strong link between the degree of sintering and the type of ligands initially present on the NC surface. We show that this approach can be extended to Cu_2ZnSnS_4 NCs. Finally, we demonstrate a $CuInSe_2$ solar cell device formed by the selenization of $CuInS_2$ NCs. This is realized by a collaboration with Armin Esmaeil Zaghi and Dr. Marie Buffiere at KU Leuven (MTM) and Imec, supervised by Dr. Marc Meuris and Prof. Dr. Jef Vleugels.

7.1 Experimental

Nanocrystal synthesis. $CuInS_2$, CuS, In_2S_3, $CuInSe_2$, Cu_2Se and In_2Se_3 NCs were obtained as described in chapters II and

III. For the synthesis of Cu_2ZnSnS_4 NCs, 4 mmol S is dissolved in 4 mL OLAm by stirring at 80 °C. Next, $Cu(acac)_2$ (2 mmol), $Zn(OAc)_2$ (1 mmol) and $SnCl_4 \cdot 5\,H_2O$ are dissolved in OLAm (10 mL) while flushing using a Schlenk line with nitrogen flow during 1 h at 100 °C. After flushing, the temperature is raised to 250 °C and the S precursor is injected in the reaction mixture. The reaction is now held at 240 °C for 10 min. During this peroid, the color gradually changes from brown to black. The reaction is stopped by cooling down to room temperature using a water bath. The resulting CZTS NCs are collected by adding toluene and EtOH. After centrifugation and discarding the dark brown supernatant, CZTS NCs are dissolved in toluene and kept in the fridge as a stock solution.

Nanocrystal processing. Thin films of different nanocrystal precursor combinations of approximately 1 µm thickness were deposited on silicon substrates for the analysis of annealing conditions. The as-synthesized nanocrystals are washed first and dispersed in chloroform. Their approximate concentration was measured and calculated by UV-VIS-NIR spectroscopy as described in 2.1.2. All thin films were drop casted from chloroform solutions and dried in air at room temperature. The ligand exchange of CIS NCs to hexanethiol is carried out by dissolving the NC pellet after centrifugation in hexanethiol, using a volume adjusted to create an approximate excess of 10000:1 hexanethiol:OLAm. This solution is stirred in an oxygen and water free atmosphere inside a glovebox at 120 °C for 1 h. After precipitation, this procedure is repeated up to 6 times. The obtained NCs are afterwards dissolved in chloroform for further processing. The ligand exchange of CZTS NCs to octanethiol is conducted in a similar fashion. $(NH_4)_2S$ capped CIS and CZTS NCs are obtained according to the procedure described in 6.1. NMR samples are obtained by drying the CIS NC solutions using a nitrogen gun, and dissolving them in $CDCl_3$.

***In situ* XRD and selenization**. Annealing processes were performed in an experimental stainless steel heating chamber, mounted in a Bruker D8 Discover, dedicated for *in situ* x-ray diffraction. Cu K alpha radiation ($\lambda = 0.15406$ nm) was used as x-ray source, while a linear detector monitored the crystallinity of the films. Selenization was carried out in a heated graphite box which could be inserted into the stainless steel heating chamber.

The samples were placed in this graphite box together with 0.1 g selenium powder (Aldrich, 99.5 %) that was put in a well a few centimeters away from the sample. The sample inside the box rested onto a seperately controlled heater, allowing independent control of the sample temperature (if higher than the graphite box temperature). After filling the outer chamber with helium the box was heated to 400℃ creating Se vapor inside the graphite box. Subsequently the sample was annealed to 550 ℃ with a ramp rate of 0.5 ℃/s. Helium gas is used as an inert gas rather than N_2 or Ar to reduce the scattering of x-rays hence increasing the quality of the data.

Characterization and analysis. Before and after annealing the crystalline phases they were characterized using XRD (Bruker D8 Discover). The crystallite size of the nanoparticles has been estimated from the FWHM of the (112) diffraction peak using the Scherrer formula: $D = 0.9\lambda/\beta cos\theta$ where β (in radians) is the linewidth at an angle 2θ (in radians) and λ is the X-ray wavelength, 1.5406 Å. Instrumental effects have been taken into account by using lanthanum hexaboride to calibrate instrumental broadening of the diffraction peaks. It should be noted that the obtained values are merely a qualitative estimate used to observe the evolution of the grain growth rather than very accurate values. The morphology and composition of the films were determined by scanning electron microscopy (SEM) and energy dispersive X-ray spectroscopy (EDX), respectively using a FEI Quanta 200F FEGSEM.

Solar cell processing and characterization. The thin film solar cell structure was completed according to standard procedures for CIGS solar cells. The substrate consists of molybdenum-coated glass, on which the precursors were coated and dried. After selenization of the NC precursors, the layers were etched with KCN, followed by chemical bath deposition of a thin n-type CdS buffer layer. Next, intrinsic ZnO was deposited by AC-sputtering(60 nm) followed by 350 nm of highly Al-doped ZnO. The top contact was formed by evaporating a 50 nm Ni-1 µm Al finger grid pattern through a shadow mask. Cells were isolated by needle scribing, making the solar cells 1 cm^2. The electrical characterization of the solar cell devices were performed by light and dark current-

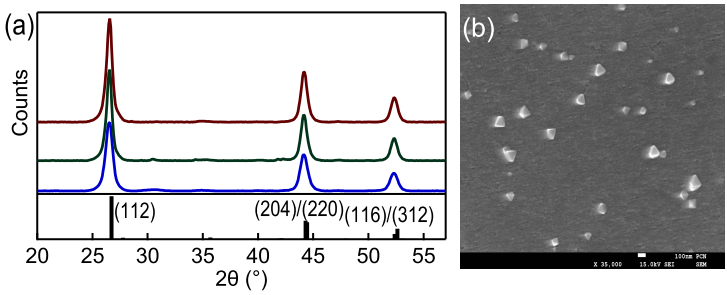

Figure 7.1: Annealing and selenization of $CuInSe_2$ NCs. (a) XRD patterns of as-synthesized $CuInSe_2$ NCs (blue), after annealing in He (green) and after selenization (red). (b) Top-view SEM image of a $CuInSe_2$ thin film after selenization.

voltage (I-V) measurements using an Oriel solar simulator using an AM1.5D spectrum with an illumination density of 1000 W/m^2 and a Keithley 2600 Sourcemeter for curve tracing.

7.2 Results and Discussion

7.2.1 $CuInSe_2$ nanocrystals

Figure 7.1a shows the XRD pattern of the as-deposited precursor film consisting of ternary selenide NCs. For the as-synthesized NCs, the characteristic XRD peaks around 26.6°, 44.6° and 52.8° are observed corresponding to the (112), (220/204), and (116/312) planes of $CuInSe_2$. These NCs have an average diameter of 16 nm as calculated using the Scherrer equation. No secondary phases could be detected indicating the formation of pure chalcopyrite NCs. EDX measurements showed a slightly In-rich composition with a Cu/In ratio of 0.9 for the precursor film.

The XRD pattern of these films after anneal in a helium atmosphere are shown in Figure 7.1a. The films of ternary selenide NCs were heated in helium for 10 min at 550 °C using a ramp rate of 0.5 °C/s. In addition to the increase in intensity of the main CISe peaks other smaller characteristic peaks of the chalcopyrite structure are also observed. It demonstrates that the crystalline quality of the structure is improved by the thermal treatment. Nevertheless the crystallite size after anneal only increased up to 27 nm indicating minor grain growth occurred. After anneal in helium also some additional peaks related to a Cu_xIn_y alloy are

present in the film. It is likely that these secondary phases are due to the loss of some selenium during the thermal treatment.

Figure 7.1a also shows the XRD pattern of these films of ternary selenide NCs after anneal in a selenium atmosphere. The same temperature profile was used during selenization as for the inert anneal while the selenium source was kept at 400 °C. Similarly to the inert anneal the crystalline quality enhances after selenization but the crystallite size only increases up to 32 nm. In contrast to the inert anneal no peaks related to a Cu_xIn_y alloy are observed for the selenized sample as the loss of selenium is suppressed during selenization.

Overall thermal treatment of ternary selenide NCs in either helium or selenium atmosphere only leads to a very limited grain growth. The crystallite sizes as calculated from XRD data is doubled at most. The sintering of these ternary nanocrystals proves to be difficult most likely due to their high melting point. This results in limited growth and densification even at a temperature of 550 °C. Incomplete removal of organic ligands and possible inefficient packing of the NCs may also contribute to the observed poor sintering.

The insert in Figure 7.1b shows a planar SEM view of the sample selenized at 550 °C. The selenization resulted in the growth of CISe particles up to 100 nanometers in size spread troughout the surface of the layer. Also some small cracks can be observed probably due to the decomposition of the organic ligands upon heating.

7.2.2 $CuInS_2$ nanocrystals

In a first attempt to introduce more reactivity to the sintering process, $CuInS_2$ NCs were used as precursor material. The exchange reaction between S and Se during selenization could stimulate grain growth and densification. The XRD pattern for the as-deposited film of $CuInS_2$ nanocrystals is shown in Figure 7.2a. The peaks at 27.9°, 46.2° and 55.1° 2θ agree well with the crystal structure for $CuInS_2$. The as-synthesized NCs have an average diameter of 5 nm as calculated using the Scherrer equation. EDX measurements show that the NCs have again a slightly In-rich composition. Selenization of these CIS NC thin films was performed at 550 °C for 10 min with the selenium source at 400 °C. Exposure to the selenium vapour caused a nearly complete ex-

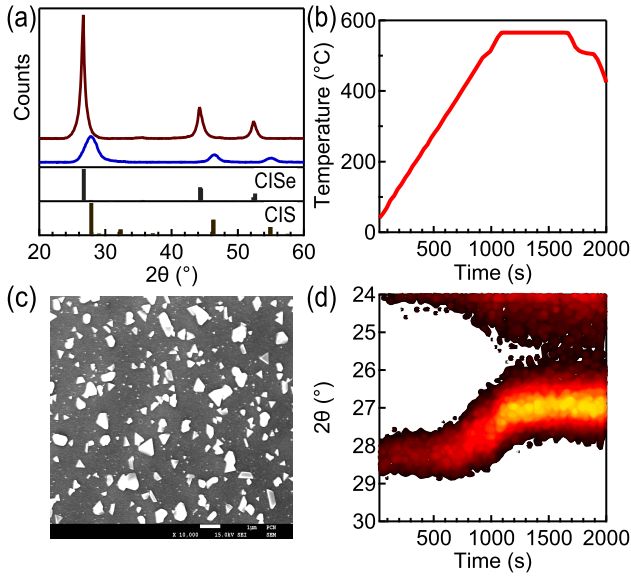

Figure 7.2: Selenization of $CuInS_2$ NCs. (a) XRD patterns of as-synthesized $CuInSe_2$ NCs (blue) and after selenization (red). (b) Temperature profile of the substrate during selenization. (c) Top-view SEM image of a $CuInS_2$ thin film after selenization. (d) *In situ* XRD pattern of $CuInS_2$ NCs during the selenization process.

change of sulfur by selenium. The XRD pattern of the film after selenization is shown in Figure 7.2a and corresponds well with the structure of chalcopyrite CISe. The selenized film shows no signs of secondary phases and according to EDX less than 5 at% sulfur remains in the final film. Note that the assumption of the non-existence of secondary phases in this work is made within the limits of detection of the equipment.

To investigate the S to Se exchange in more detail *in situ* XRD was used during the anneal. Figure 7.2d shows the variations in XRD peak position, width and intensity for the (112) reflection as a function of time. Between 300 °C and 400 °C the intensity of the peak becomes more intense and the (112) peak position starts to shift towards lower 2θ values. It is clear from Figure 7.2d that $CuInS_2$ gradually transforms into CISe as indicated by the gradual shift in the position of this peak. The (112) peak continues to move to a lower position when the substrate temperature further increases. The gradual incorporation of the larger selenium atoms

into the crystal lattice induces a lattice expansion and hence a shift towards a smaller diffraction angle for the (112) peak. The lack of reduction in peak width indicates that no significant grain growth is occurring during the exchange reaction. Around 540 °C the $CuInS_2$ film is fully converted to $CuInSe_2$. The subsequent sharpening of the (112) peak indicates that most grain growth takes place once the transformation to CISe has been completed. The crystallite size after selenization as calculated from XRD data is 27 nm which corresponds to a fourfold increase.

The surface of the selenized film is characterized by large grained $CuInSe_2$ as can be seen in Figure 7.2c. In comparison to the ternary selenide NCs, selenization of the ternary sulfide NCs results in much bigger grains with sizes ranging from 100 nm up to 1 µm. This is in agreement with the more manifest increase of the average crystallite sizes as observed in XRD.

7.2.3 Binary metal sulfides

In a second attempt to introduce additional reactivity NCs of binary metal sulfides were used as precursors. Figure 7.3a shows the XRD pattern of an as-deposited film consisting of CuS and In_2S_3 NCs. The films were intentionally deposited into two groups, Cu-rich and Cu-poor precursor films, with a Cu/In ratio of 1.2 and 0.8, respectively. The XRD patterns of the two precursor films are very similar and hence only the Cu-rich film is shown here. For the as-deposited layer only some weak and broad peaks assigned to the CuS phase can be detected.

Annealing this mixture of binary sulfides in a selenium atmosphere (selenium source at 400 °C) increases the crystallinity as well as the morphology of the obtained film. Both a Cu-poor and Cu-rich precursor film were investigated and the *in situ* XRD data is shown in Figure 7.3b. The (112) peak of the ternary $CuInS_2$ phase appears for both compositions around 325 °C. At higher temperatures the sulfur becomes exchanged for selenium and the (112) peak starts to shift towards the corresponding peak position of CISe as was the case for the ternary sulfide particles. It seems that the solid-state reaction between the binary compounds takes places before any reaction with the selenium occurs.

For the Cu-poor sample, the crystallite size as determined by a Scherrer analysis is only 7 nm after the anneal which is comparable to the original precursor compounds. During the seleniza-

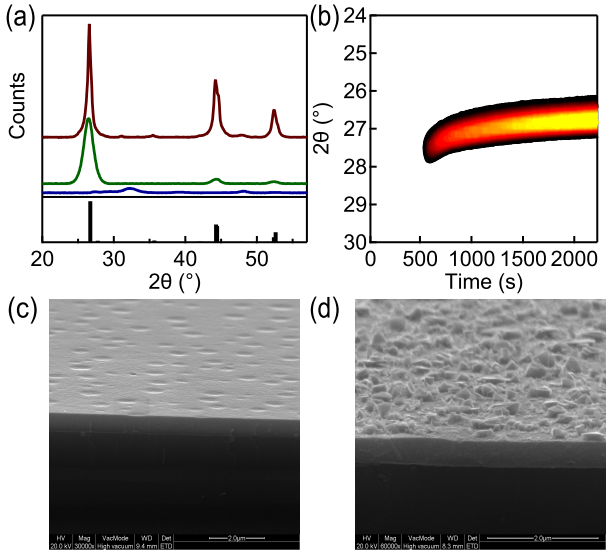

Figure 7.3: Selenization of binary sulfide NCs. (a) XRD patterns of a combination of CuS and In_2S_3 NCs (blue) and after selenization of the Cu-poor precursor (green) and the Cu-rich precursor (red). The database pattern for $CuInSe_2$ is shown as black bars. (b) *In situ* XRD pattern taken during the selenization of the Cu-rich precursor. (c) Cross-section SEM image of the $CuInSe_2$ thin film after selenization of the Cu-poor precursor. (d) Cross-section SEM image of the $CuInSe_2$ thin film after selenization of the Cu-rich precursor.

tion process almost no sharpening of the (112) peak is observed. In contrast for the Cu-rich sample the XRD intensity increased continuously and the sample exhibited significant grain growth resulting in a crystallite size of 50 nm. It shows that a Cu-rich composition is strongly favored in terms of grain growth. It is believed that during this step copper selenide is formed which can act as a fluxing agent[15,16]. In this study no clear evidence of any secondary phases could be detected during *in situ* XRD though. However SEM-EDX has revealed the presence of copper selenide crystals on the surface indicating that the presence of this phase clearly influences the grain growth but that the formation on the surface is rather localized. In the case of Cu-poor films the formation of these large crystals was not observed as shown in Figure 7.3c.

The position of the (112) peak for these binary metal sulfides

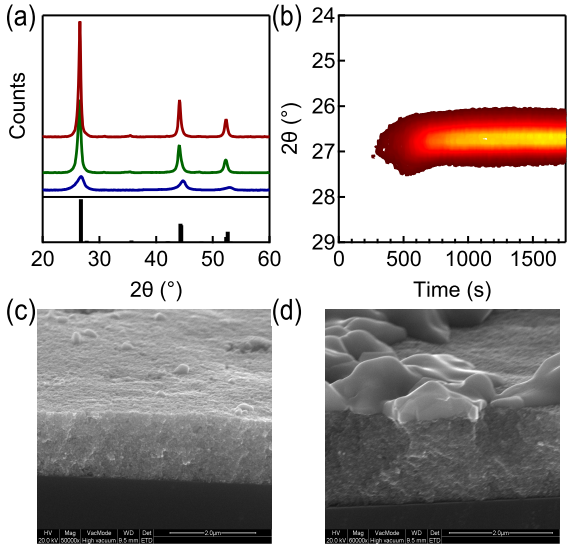

Figure 7.4: Annealing and selenization of binary selenide NCs. (a) XRD patterns of a combination of Cu_2Se and In_2Se_3 NCs (blue) and after annealing in helium (green) and selenization (red). (b) *In situ* XRD pattern taken during the selenization of binary selenide NCs. (c) Cross-section SEM image of the $CuInSe_2$ thin film after annealing in He. (d) Cross-section SEM image of the $CuInSe_2$ thin film after selenization.

is slightly higher than for the ternary compounds. This indicates that the transformation is not fully complete and that some sulfur is still present in the crystal lattice. EDX measurements confirmed that for both films about 10 at% of sulfur remained in the final film whereas for the $CuInS_2$ based films nearly sulfur-free films could be obtained.

7.2.4 Binary metal selenides

Besides binary sulfides, we consider binary selenide NCs as a precursor system. The films show intense and sharp peaks after anneal, both in helium and selenium atmosphere (Figure 7.4a). Besides the (112) peak also (103) and (211) planes of the CISe phase are observed. The high intensity and sharpness of the (112) peak compared to that of the films consisting of ternary selenide particles indicates that the reaction between these binary selenides results in layers with much improved crystallinity.

Figure 7.4 shows the *in situ* XRD for the anneal in a selenium atmosphere. Already at a temperature of 300 °C the CISe phase starts to form and a decrease of the FWHM is observed up to 400 °C but almost no additional grain growth occurs for higher temperatures. In contrast to the anneal in helium, giving rise to 25 nm crystallites, selenization causes additional grain growth resulting in an average crystallite size of 55 nm. This additional improvement in the crystalline quality and grain growth is supported by the supply of fresh selenium from the gas phase. Possibly also copper selenide compounds are formed which can act as a fluxing agent to assist the atom diffusion for grain growth. The selenium evaporation from the mixed compounds and a lack of copper selenide compounds result in a smaller crystallite size and less densification of the layer. It should however be noted that the more dense and large-grained morphology is only obtained in the top of the layer as shown in the cross-section SEM in Figure 7.4d.

7.3 The effect of ligand chain length on sintering and impurities

Up to now, precursor systems have been investigated with respect to sintering starting from a very similar surface chemistry - OLAm is applied as the sole ligand in all the NC synthesis while no adjustments were made prior to deposition. A second analysis we perform in this section is the comparison of different types of ligands on $CuInS_2$ and Cu_2ZnSnS_4 NCs, with a focus on the amount of carbon left after sintering. Therefore, we first describe the NCs and the extend of the ligand exchange towards these new ligands.

7.3.1 Altering the surface chemistry

The CIS NC synthesis as described in 2.1.1 produces polydisperse, quasi-spherical NCs in the range of 6-10 nm as shown in Figure 7.5a. The XRD diffractogram of a thin film of CIS NCs (Figure 7.5c) shows peaks corresponding to chalcopyrite CIS represented by black bars. Our CZTS synthesis produces NCs of various sizes and shapes (Figure 7.5c), whereas the diffraction pattern in Figure 7.5d confirms the kesterite crystal structure.

Measuring a solution of as-synthesized and purified CIS NCs using ^{1}H NMR spectroscopy produces a spectrum shown in Fig-

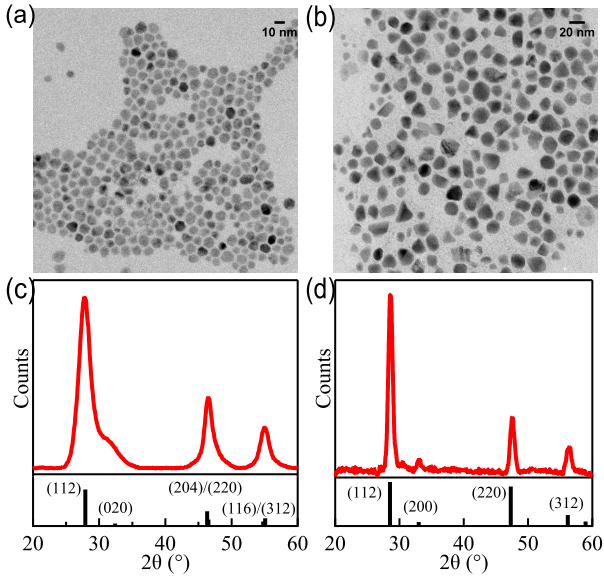

Figure 7.5: Characterization of as-synthesized NCs. TEM micrographs of (a) CIS NCs and (b) CZTS NCs. XRD diffractogram of a thin film of (a) CIS NCs and (b) CZTS NCs.

ure 7.6a. Apart from the $CHCl_3$ peak at 7.3 ppm, all the signals corresponds to hydrogens of OLAm molecules interacting with the NC surface, as indicated by the broadening of the peaks due to relaxation effects. The peak at 5.36 ppm corresponds to 2 hydrogens attached to carbons forming the alkene function of the OLAm molecule. This well-separated signal is convenient to measure the ligand density and to monitor during our ligand exchange procedures. For as-synthesized CIS NCs we calculated a ligand density of 2.85 nm^{-2}. After performing the intense ligand exchange to hexanethiol (Figure 7.6b), OLAm is still present indicated by the peak at 5.36 ppm. The ligand density of the leftover OLAm is quantified as 0.15 nm^{-2}, meaning that our ligand exchange procedure removes up to 95 % of the original OLAm molecules. An intense ligand exchange procedure is needed since OLAm is strongly bound to the CIS surface, as described in chapter V. As shown in Chapter VI, all organic molecules can be removed from the surface by performing the ligand exchange to $(NH_4)_2S$.

We monitored the ligand exchange of CZTS NCs to octanethiol in a similar fashion (Figure 7.6b). Here, we notice a similar

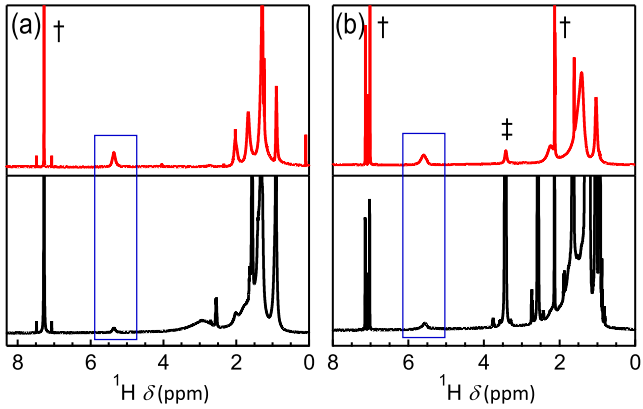

Figure 7.6: ^{1}H NMR spectra of CIS (a) and CZTS (b) NC dispersions in respectively $CDCl_3$ and toluene-*d8*. Red spectra corresponds to as-synthesized and purified NCs, while black spectra are obtained after ligand exchange to thiols. Solvent signals are denoted by (†), and ethanol is marked by (‡).

binding behavior of OLAm on the surface of CTZS NCs. After the exchange to octanethiol, we calculated that OLAm coverage has reduced by 70 %. Along with resonances corresponding to bound OLAm and octanethiol, the sample also consists of free octanethiol.

7.3.2 Sintering and elemental analysis

To show the effect of sintering on CIS NCs, a thin film of approximately 1 µm was heated containing different ligand cappings using the same temperature profile and measured by *in situ* XRD (Figure 7.7). All samples received a ramp of 1 °C/s to 450 °C in He and are kept at this temperature for 30 min. As shown in Figure 7.7b-c the difference between peak sharpening and thus crystal growth in a NC layer capped with OLAm and hexanethiol is significant, giving rise to larger crystallites when the amount of carbon surrounding the NCs is lowered going from a C18 ligand to a C6 ligand. We presume that the difference in boiling points between OLAm (360 °C) and hexanethiol (150 °C) are responsible for the easier removal of the latter ligand, with a better sintering as a consequence. A second, related, explanation is that CIS NCs are more closely packed when surrounded by hexanethiol compared to OLAm, making it easier to sinter due to the closer proximity

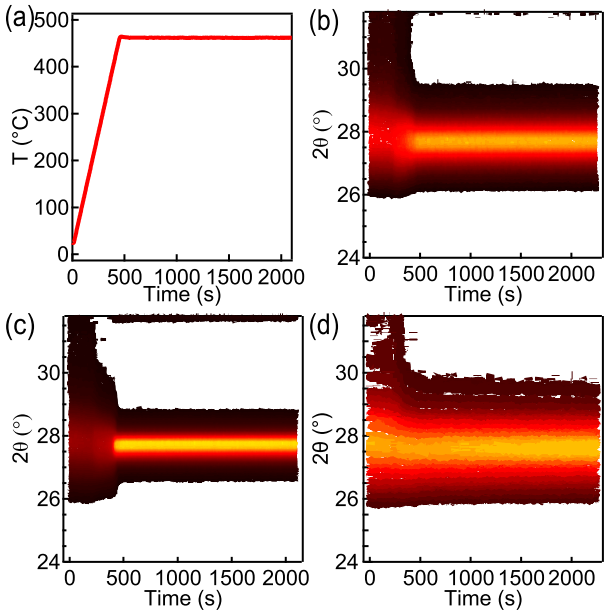

Figure 7.7: *In situ* XRD diffractograms following the (112) reflection of CIS as a function of time during annealing in He. (a) Temperature profile. (b-c) CIS NCs stabilized by OLAm and hexanethiol, respectively. (d) CIS NCs stabilized by $(NH_4)_2S$.

Ligands	Crystallite sizes (nm)	
	$CuInS_2$	Cu_2ZnSnS_4
Non-annealed	3.90	10.52
Oleylamine	8.18	31.29
Thiol	19.38	34.20
$(NH_4)_2S$ in He	5.66	13.69

Table 7.1: Scherrer calculations

of the adjacent NCs. CIS NCs stabilized by $(NH_4)_2S$ show little to no sintering at 450 °C in a helium atmosphere (Figure 7.7d). From the diffraction patterns obtained after each treatment, we calculated crystallite sizes using the Scherrer equation for both CIS and CZTS NCs (Table 7.1). While the trend we observe for CIS NCs is more pronounced than CZTS NCs, we can conclude that shorter ligand chain lengths give rise to a larger sintering effect, while for $(NH_4)_2S$ the absence of carbon does not give the expected increase in sintering, an interesting observation that we investigate thoroughly in chapter VIII.

After annealing CIS and CZTS NCs, we measured the carbon content using two different techniques. In Figure 7.8a, an XPS depth profile is shown on a thin film of CIS NCs containing different ligands initially stabilizing the NCs. Prior to sputtering, the carbon signal is high by contamination on the surface of the sample. The signals from inside the layer show a significant amount of carbon left in the case of OLAm. Using hexanethiol to initially cap the NCs, the signal is lowered by a large amount. $(NH_4)_2S$ as ligand on the NCs lowers the carbon impurities after annealing to a minimum. For both CIS and CZTS powders obtained after annealing, we measured the carbon and nitrogen concentration using a CHNS analyzer (Figure 7.8b-c), where the sample is burned in an oxygen containing plasma, and CO_2, H_2O, NO_x and SO_x can be separated using gas chromatography. Quantifying these signals gives the same trend for both CIS and CZTS NCs. The remaining amount of carbon (Figure 7.8b) is lowered substantially going from OLAm to hexanethiol/octanethiol to $(NH_4)_2S$ after annealing. The larger concentration of both carbon and nitrogen in CZTS can be related to a higher ligand density, or the easier removal of ligands both during the purification of the dispersions and the annealing itself. Even though the temperature is well above the boiling point of the OLAm or thiol molecules, carbon

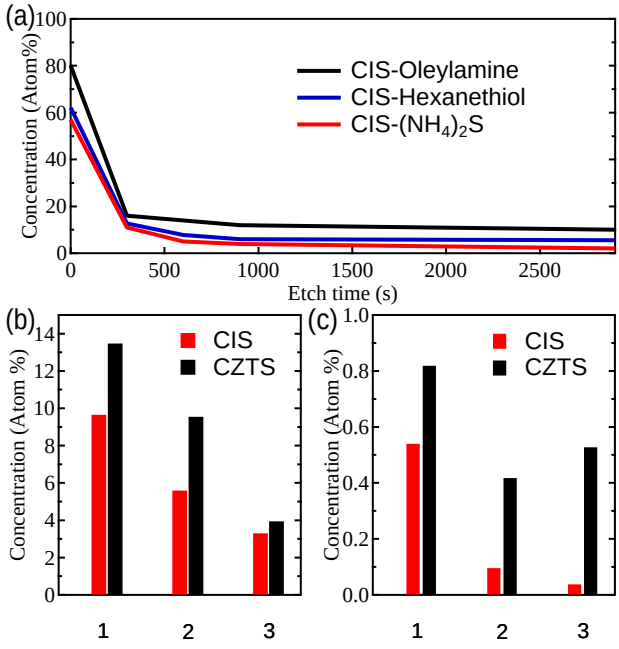

Figure 7.8: (a) XPS carbon depth profile of thin film of CIS NCs after annealing. (b) Carbon and (c) nitrogen analysis on powders of CIS and CZTS NCs containing different initial ligands: 1 = Oleylamine, 2 = Hexane/Octanethiol (CIS/CZTS), 3 = $(NH_4)_2S$.

- either as hydrocarbon molecules or amorphous - is not fully removed. Nitrogen contamination from OLAm is much lower and thus less relevant, but confirms that the replacement of amines to thiols was successful (Figure 7.8c).

7.4 Solar cell demonstration

In a trial towards thin film solar cells, we tested $CuInSe_2$ layers with a standard glass/Mo/$CuInSe_2$/CdS/ZnO/AZO structure. These layers were formed by selenization of $CuInS_2$ NCs with hexanethiol ligands, as described above. CIS/hexanethiol NCs were dissolved in hexanethiol and casted on a Mo-coated soda-lime glass substrates. The depositions of the ink was repeated up to 5 times with a short anneal at 150 °C on a hot plate in between. The final layers are crack-free, as shown in Figure 7.2a. We selenized the CIS NCs by employing H_2Se (500 °C 15 min) and Se (500 °C 60 min). The cross-section SEM images of the final solar cell structures is shown in Figure 7.2b-c, respectively. We notice that the use of H_2Se leads to a denser $CuInSe_2$ layer, pointing towards a better recrystallization process. The I-V curves of the solar cells are shown in Figure 7.2, with the solar cell parameters outlined in the table below. For this trial, we demonstrate a total area efficiency on 1 cm^2 of 1.38 % and 0.85 % for the process using H_2Se and Se, respectively. We note that the $CuInSe_2$ layers can be further optimized. First, the thickness of the layer could be increased to a minimum of 1 µm. Additionally, the selenization process can be improved to yield larger crystal sizes. Guo *et al*[17] presented fully recrystallized $CuInSe_2$ layers starting from $CuInS_2$ NCs with oleylamine ligands. This makes us conclude that harsher selenization conditions should be used to transform this precursor.

7.5 Conclusions

We investigated the differences in thermal annealing behaviour of ternary and mixtures of binary colloidal NCs. The focus is put on the reactivity of the annealing/sintering process towards $CuInSe_2$, with a similar surface chemistry and thermal profile used for all systems. Between the ternary $CuInSe_2$ and $CuInS_2$ NCs, the selenization of the latter is clearly more reactive likely owing to the exchange of sulfur for selenium. During the selenization of binary

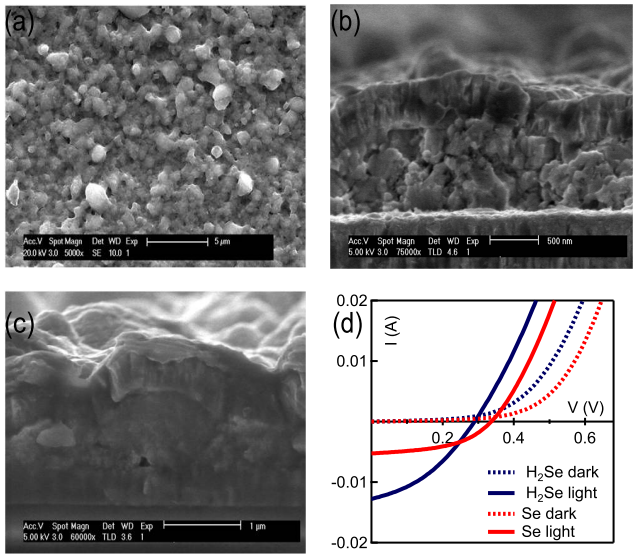

Process	J_{sc} (mA/cm^2)	V_{oc} (mV)	FF (%)	η (%)	R_{sh} (Ω/cm^2)	R_s (Ω/cm^2)
H_2Se	12.74	289.1	37.5	1.38	69.83	8.53
Se	5.26	336.0	48.2	0.85	308.0	0.57

Table 7.2: (a) CIS/hexanethiol precursor as-deposited. (b) After selenization using H_2Se at 500 °C for 15 min and completion of solar cell. (c) After selenization using Se at 500 °C for 60 min. (d) I-V curves. The analysis of solar cells is shown in the table (cell area = 1 cm^2).

sulfides, we found that the reactivity greatly depends on the stoichiometry, tuned by the relative amounts of CuS NCs to In_2S_3 NCs. A Cu-rich stoichiometry is clearly preferred during transformation, giving rise to larger $CuInSe_2$ crystallite sizes. Using binary selenides, we confirmed that selenization has a positive impact on the transformation compared to inert atmosphere. These binary selenides are preferred over ternary selenides, and provide the largest final crystallite sizes. Considering all precursor systems, large micrometer-sized crystals, if any, were only observed on top of the layer after selenization.

By comparing different ligand types on CIS and CZTS NCs, we were able to establish a strong link between the amount of carbon present in a CIS and CZTS NC precursor ink, the sin-

tering behaviour and the contamination of residual carbon in the final layer. Using ^{1}H NMR spectroscopy, we were able to quantify the amount of ligands stabilizing the NCs in the ink, and confirming the ligand exchange processes from the original ligand to short thiols. By following the diffraction patterns as a function of time during the thermal treatment, we observe that different ligand capping give rise to significant differences in degree of sintering between NCs. We attribute this to the ease of removing capping ligands during the heating process, where ligands with a lower boiling point are easier to remove. This is illustrated by our measurements of the remaining amount of carbon after the process, which is an unwanted contamination in a CIS or CZTS absorber layer. We conclude that tailoring the surface of colloidal NCs prior to a sintering process has a large impact, and should be optimized with respect to the application. In a final section, we have demonstrated the potential of selenization of CIS NCs towards $CuInSe_2$ thin film solar cells. With room for optimization, a cell efficiency of 1.38 % is presented. This shows that the use of NC precursors for CIGS solar cells is promising.

Chapter VIII

Annealing of sulfide stabilized colloidal nanocrystals

The observation that CIS NCs capped by $(NH_4)_2S$ show little to no sintering in a thin film when annealing in an inert atmosphere provides the basis for this chapter. It is remarkable that $(NH_4)_2S$ - a compound which is easily decomposed at relatively low temperatures - blocks the sintering of NCs compared to long, organic ligands. Since we have shown that, with respect to keeping carbon impurities to a minimum, capping with inorganic ligands is clearly preferred, this provides a challenge. However, for applications that require the NCs to keep their size-dependent properties, this is an opportunity to withstand sintering at elevated temperatures. Here, we aim to understand the origin of this effect. This analysis is done in collaboration with Hasselt University, Inorganic and Physical Chemistry lead by Prof. Dr. Marlies van Bael and Prof. Dr. An Hardy and IMEC, division IMOMEC. The TGA-MS measurements in this department were performed and analyzed by Hanne Damm. XRD measurements were performed by Boris Capon, supervised by Prof. Dr. Christophe Detavernier at the Department of Solid-State Sciences of Ghent University.

8.1 Experimental

Materials. $Cu(acac)_2$ (Aldrich, 99.99 %), $In(acac)_3$ (Aldrich, 99.99 %), Sulfur (Merck, 99.999 %), Oleylamine (Acros, Tech. 80-90 %), 1-Octadecene (Alfa Aesar, Tech. 90 %), $(NH_4)_2S$ (Aldrich, 20 w % in H_2O) and formamide (Fluka, $\geq$98 %) were used without

additional purification.

Nanocrystal synthesis. CIS NCs were obtained according to the procedure at 180 ℃ as described in 2.1.1.

Nanocrystal processing. As-synthesized CIS NCs with oleylamine ligands were exchanged to $(NH_4)_2S$ as described in 6.1. The resulting solution in formamide is used to deposit CIS NC thin films, by drop casting an amount corresponding to a dry thin film of approximately 1 µm onto a silicon substrate, on a heating plate at 60 ℃.

Characterization. To determine the mean diameter of the NCs used in this work, and the effect of heating in vacuum, we used bright-field TEM images recorded with a JEM-2200FS transmission electron microscope. These samples were prepared by dipping a TEM grid in a dilute NC solution. XRD and *in situ* XRD patterns were recorded using a Bruker D8 Discover. Cu K alpha radiation was used as an x-ray source, while a linear Vantec detector monitored the crystallinity of the thin films. TGA-MS measurements were performed on NCs obtained after precipitation with i-PrOH and subsequent drying of the pellet after centrifugation using vacuum. Approximately 7 mg of this powder was analyzed with a TA Instruments TGA Q5000 coupled with a Pfeiffer Vacuum ThermoStar^{TM} MS. The thermal decomposition has been carried out in a 5% H_2/Ar or a He flow. For 5% H_2/Ar flow, settings of nitrogen have been used. More detailed analyses of the fragments formed during ionization of the evolving gas molecules has been done scanning specific m/e signals that were chosen after a wide m/e (5-145) scan to obtain a better signal-to-noise ratio. XPS analysis was performed using a S-probe spectrometer with an Al-source (monochromatized Al-radiation: 1486 eV). The measured surface was 250 µm by 1000 µm. The flood gun of 3 eV was used. Experimental data were processed using the software package CasaXPS. Prior to analysis the peak of adventitious carbon was calibrated towards 284.6 eV. XPS measurements were performed by Dr. Els Bruneel, Physical and Inorganic Chemistry at Ghent University.

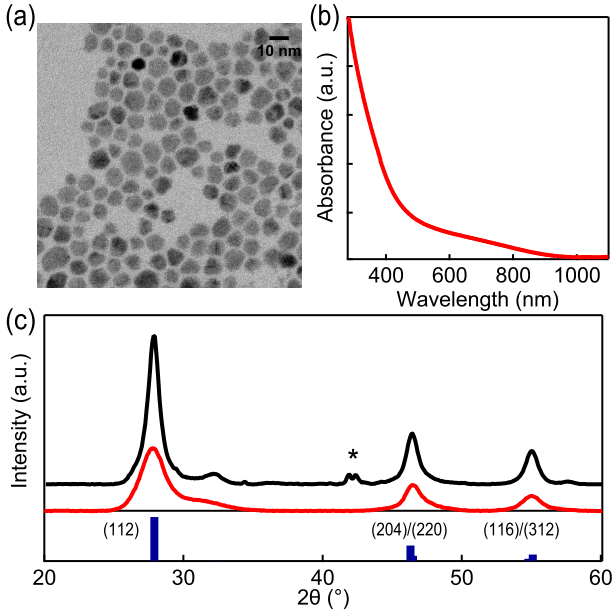

Figure 8.1: Characterization of as-synthesized CIS NCs. (a) TEM micrograph. (b) UV-Vis spectrum of a NC solution in $CHCl_3$. (c) XRD pattern of a NC thin film (red) before and (black) after annealing in helium. The expected reflections of chalcopyrite $CuInS_2$ are shown as blue bars.

8.2 Results and discussion

Figure 8.1a shows a representative TEM micrograph of the CIS NCs used in this study. The NCs appear as quasi-spherical with a mean diameter of $\approx 8\,\text{nm}$ and a size dispersion of $\approx 15\%$. According to the XRD pattern, chalcopyrite NCs are obtained with no secondary phases present, while the UV-Vis absorption spectrum (Figure 8.1b) shows an absorption onset around the band gap of bulk CIS (1.54 eV). Annealing a 1 µm thin film of these as-synthesized CIS NCs to 450 °C at a rate of 1 °C/s in a helium atmosphere results in a sharpening of the CIS reflections as shown in the upper XRD diffractogram in Figure 8.1c. According to the Scherrer equation, this sharpening of the peaks reflects crystal growth during the heat treatment. We could identify the secondary phases present in the annealed sample, indicated by (*) in Figure 8.1c, as a Cu_xIn_y alloy. This likely results from a loss of sulfur upon annealing.

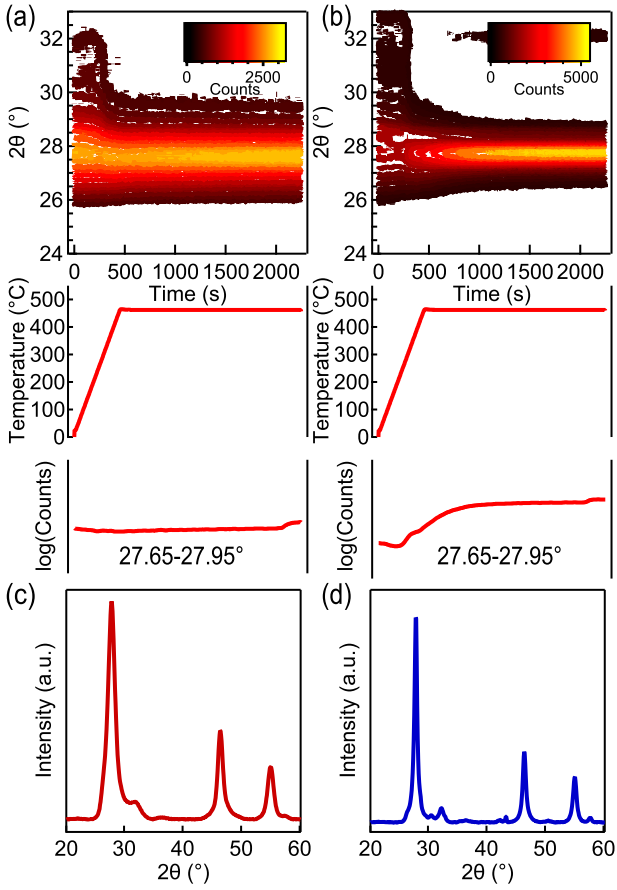

Figure 8.2: Comparison of annealing behaviour of CIS NCs capped with $(NH_4)_2S$. (a-b) *In situ* XRD following the (112) peak during the heating process in (left) helium and (right) forming gas. (c-d) Temperature profile of the *in situ* XRD measurements. (e-f) Integrated peak intensity as a function of time, (dashed line) indication of onset of sintering. (g-h) XRD pattern recorded after completing the thermal treatment.

After synthesis and purification, the original steric stabilization by oleylamine ligands can be replaced by charge stabilization using $(NH_4)_2S$ in a two-phase exchange reaction[13]. In chapter VI, we show that, apart from the nanocrystals being closer together on the TEM grid, the basic characteristics of the CIS NCs are not different from the results shown in Figure 8.1. The thus obtained particles can be dispersed in formamide and deposited by drop-casting as a thin film as well. Even though CIS NCs capped by $(NH_4)_2S$ are stable in formamide for up to 2 days, we deposited the thin films right after the ligand exchange to prevent further changes in surface chemistry prior to annealing. Using *in situ* XRD, we followed the effect of annealing on a thus formed thin film of $(NH_4)_2S$ stabilized CIS NCs. Figure 8.2a shows the evolution of the signal intensity in the 2θ region around the CIS (112) peak as a function of time during a thermal treatment in helium following the indicated temperature profile in Figure 8.2c. Most notably, no significant peak sharpening is observed, pointing towards an inhibition of sintering by $(NH_4)_2S$ ligands as compared to long chain organic ligands (see Figure 8.1c). On the other hand, we found that the sintering of CIS NCs with $(NH_4)_2S$ ligands can be triggered using forming gas during the process (5 % H_2 in He). In this case (Figure 8.2b), the (112) peak sharpens throughout the process, indicating growth of the CIS NCs. For comparison, XRD patterns are shown after the annealing in helium (Figure 8.2g) and forming gas (Figure 8.2h). Taking a closer look at the diffracted intensity in the 27.65-27.95 2θ range as a function of temperature, we find that it remains constant under inert atmosphere, while it starts increasing from $\approx$ 300 °C on under reducing conditions.

To further confirm the difference in annealing behaviour between OLA capped and $(NH_4)_2S$ stabilized CIS NCs, we compared their behaviour using *in situ* TEM. Dip coated layers were heated to 550 °C in vacuum, as shown in Figure 3. As expected, CIS NCs capped with oleylamine sinter in the range of 450-500 °C (Figure 8.3a-b), even showing the formation of large crystallites with dimensions exceeding 100 nm and inter particle adhesion. This behavior is not observed in CIS NCs with $(NH_4)_2S$ ligands (Figure 8.3c-d) subjected to the same treatment. In this case, the CIS NC size and shape is preserved throughout the heating process. While it is difficult to set an exact temperature during *in situ* TEM studies, the difference between both samples is obvious and

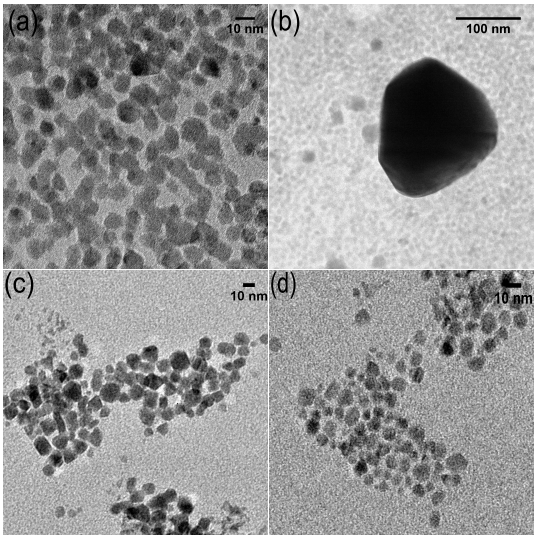

Figure 8.3: TEM images of (a-b) CIS NCs with oleylamine ligands and (c-d) $(NH_4)_2S$ ligands at an estimated temperature of 450 °C.

concurs with the observations from the *in situ* XRD measurement in Figure 8.2a.

In order to identify the species leaving the nanocrystal-ligand system upon annealing, TGA-MS measurements were carried out on a powder of CIS NCs capped with $(NH_4)_2S$ in both inert and reducing atmosphere. Figure 8.4 shows the TGA-DTG signal when both samples were heated up to 600 °C at 10 °C/min. In TGA, we observe an overall similar, step wise weight loss up to a temperature of 600 °C amounting to $\approx 30\,\%$ of the original mass. Nevertheless, the DTG signal shows a clear difference between both samples in the temperature range 400-600 °C, where the sample annealed in an inert atmosphere loses extra mass. The DTG signal also emphasizes the step wise decomposition process.

Using mass spectrometry coupled in-line with the TGA, gaseous species evolving from both samples were detected *in situ*. As summarized in Table 8.1, this involves species which we suspect to originate from both $(NH_4)_2S$ and formamide. While the powder used for the TGA-MS measurements appeared to be dry, fragments originating from the decomposition of the solvent used, i.e., formamide, can clearly be distinguished. The response for all the fragments in Table 8.1 is shown as a function of tem-

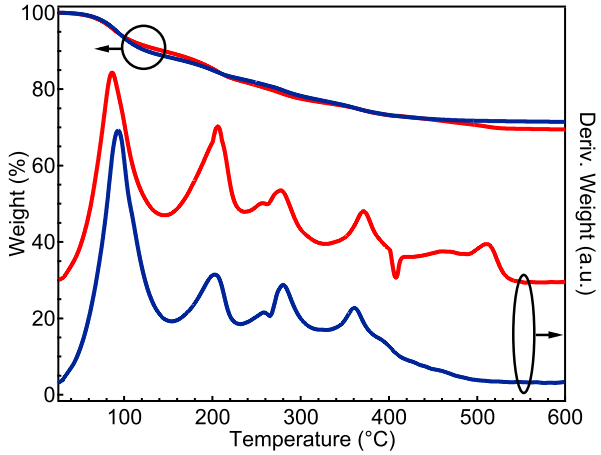

Figure 8.4: TGA-DTG spectra of CIS-$(NH_4)_2S$ NCs in (blue) Ar/H_2 (5 % H_2) and (red) He.

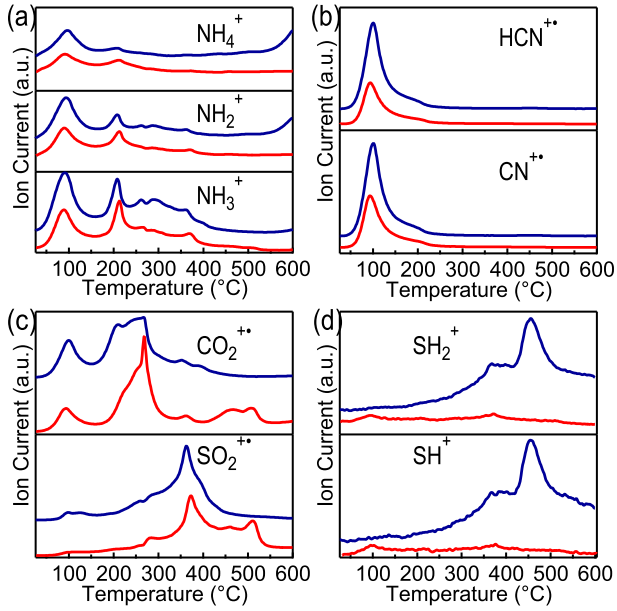

Figure 8.5: Detected signals in mass spectrometry as a function of temperature during the TGA-MS experiment. Red and blue lines represent signals for samples heated in inert respectively reducing atmosphere.

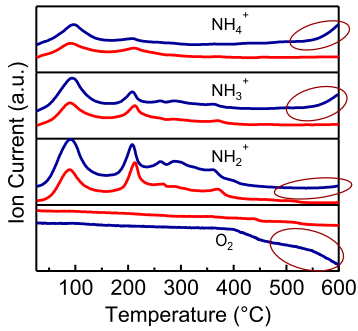

Figure 8.6: Explanation of the additional increase of NH_2^+, NH_3^+ and NH_4^+ species at higher temperatures. The blue and red curves show the TGA-MS signals in reducing and inert atmosphere, respectively. The red circles indicate the formation of H_2O by the reaction with O_2, leading to an increased signal for H_2O fragments coinciding with NH_x^+ species.

m/e	Species	Proposed source
16	NH_2^+	$(NH_4)_2S$/$HCONH_2$
17	NH_3^+	$(NH_4)_2S$/$HCONH_2$
18	NH_4^+	$(NH_4)_2S$/$HCONH_2$
26	CN^+	$HCONH_2$
27	$HCN^{+\cdot}$	$HCONH_2$
33	SH^+	$(NH_4)_2S$
34	SH_2^+	$(NH_4)_2S$
44	$CO_2^{+\cdot}$	$HCONH_2$
64	$SO_2^{+\cdot}$	$(NH_4)_2S$

Table 8.1: List of m/e values detected in TGA-MS.

perature in Figure 8.5. At 100 °C, the largest mass loss originates from HCN/CN and CO_2 fragments, and this is similar for both annealing conditions. We identify species with m/e values of 16, 17 and 18 as NH_2^+, NH_3^+ and NH_4^+ species, originating from either $(NH_4)_2S$ or formamide. Under H_2/N_2 atmosphere, the corresponding signals (Figure 8.5a) show an increase at high temperatures, which we attribute to the formation of H_2O - which leads to fragments with the same m/e - by the reaction between H_2 and residual O_2, an interpretation corroborated by the reduction of the residual O_2 signal at m/e=32 (Figure 8.6).

Next, at 250 °C, another set of CO_2 fragments is released, followed by the release of SO_2. Importantly, fragments with an m/e ratio of 33 and 34, corresponding to SH^+ and SH_2^+, respectively,

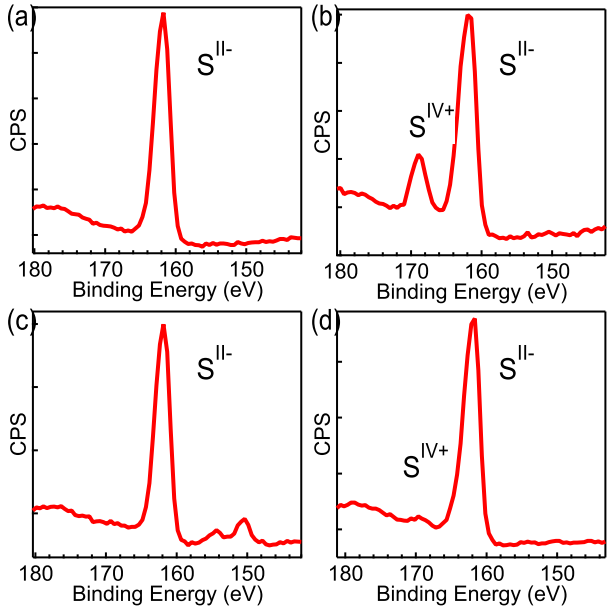

Figure 8.7: XPS spectra of $CuInS_2$ layers capped by $(NH_4)_2S$ on Si: As-deposited (a), after 3 weeks in ambient conditions (b), after following the standard thermal treatment in H_2/N_2 (c) and after heating to 300 °C in N_2 (d).

are detected from 300 °C onwards in the case of a reducing atmosphere, and are absent under inert conditions, These fragments are typical of H_2S, indicating its formation only in the case of H_2/Ar and their appearance coincides with the onset of sintering in the CIS nanocrystal film. Interestingly, CO_2 and SO_2 are detected in both conditions. We attribute CO_2 to the decomposition of formamide, and we suspect that this coincides with the oxidation of S^{2-} from $(NH_4)_2S$ - the species stabilizing the NCs in formamide - to SO_2 (*cf. infra*). In Figure 8.5c, we can also observe the species responsible for the difference in DTG signals (Figure 8.4). At 500 °C, compared to annealing in reducing atmosphere, an excess amount of CO_2 and SO_2 leaves the sample. Since we base our annealing results in *in situ* XRD on thermal treatments that do not exceed 450 °C, it appears that the presence of this species is related to the inhibition of the sintering of NCs. In the case of hydrogen containing atmosphere, this oxidized compound can be reduced to H_2S, leaving the surface.

To confirm the presence of oxidized sulfur in films of CIS NCs

originally stabilized by $(NH_4)_2S$, we analyzed various films using XPS. Figure 8.7a shows an XPS spectrum recorded on a layer of as-deposited NCs stabilized by $(NH_4)_2S$. The spectrum shows a single peak related to S at 161 eV, which is typically attributed to a relatively weakly bonding 2p state of S^{2-}. We stress that no oxidized sulfur species are found prior to annealing, which is in any case carried out as soon as possible after deposition. After keeping this layer under ambient conditions for 3 weeks, a second feature emerges at higher binding energy (Figure 8.7b), which can be related to S species in a higher oxidation state[18](i.e., S^{4+} or higher). We thus conclude that all sulfur in the system is initially present as S^{2-} ($CuInS_2$ and $(NH_4)_2S$), while the sulfide at the CIS surface progressively oxidizes to form SO_2, SO_3^{2-} and/or SO_4^{2-}. Since we found that NC sintering is inhibited under inert atmosphere for layers composed of solely S^{2-} as well, we measured an XPS spectrum of these fresh layers after annealing in H_2/Ar (Figure 8.7c) and N_2 (Figure 8.7d). Only in the latter case, a slight contribution of oxidized sulfur is discernible. This shows that the oxidation of sulfide species occurs during annealing under inert conditions, probably related to the decomposition of leftover solvent.

In conclusion, we find that observed sintering under reducing conditions is related to the release of sulfide as H_2S, whereas under inert conditions, the sulfide remains in the film, being oxidized to SO_2, SO_3^{2-} and/or SO_4^{2-} and thereby inhibiting sintering. The observation that sintering of NCs stabilized by $(NH_4)_2S$ is inhibited up to relatively high temperatures was further tested for two different NC systems. In figure 8.8, we compare the annealing behavior of CZTSe and CdSe NCs processed in the same way as the CIS NCs. By following the (112) peak of kesterite CZTSe during heating in helium (Figure 8.8a) and H_2/Ar (Figure 8.87), we can conclude that a similar difference in sintering behavior is present. Moreover, in the case of CdSe NCs, the same difference in degree of sintering between helium (Figure 8.87) and H_2/Ar (Figure 8.87) atmosphere can be found. We suspect that the oxidation of $(NH_4)_2S$ is again responsible for the difference in annealing behaviour of these NCs systems, meaning that the effects we measured for CIS NCs apply to other semiconductor NCs as well.

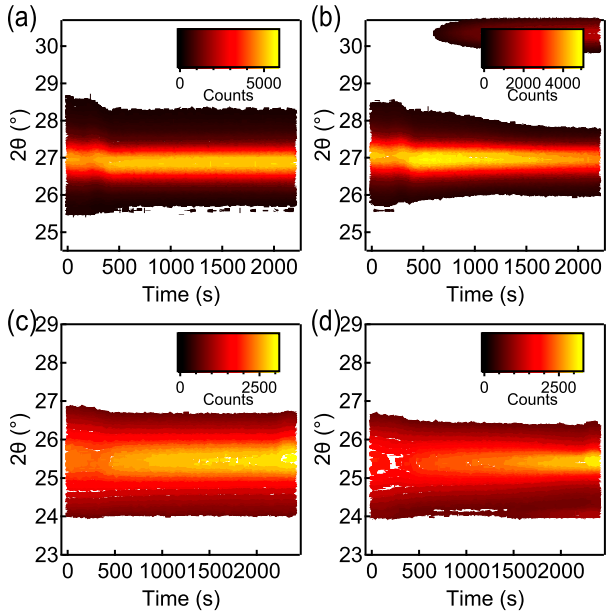

Figure 8.8: Comparison of annealing behavior of (a-b) CZTSe NCs and (c-d) CdSe NCs capped by $(NH_4)_2S$. (a-c) Annealing in helium. (b-d) Annealing in H_2/Ar.

8.3 Conclusions

In summary, annealing treatments of layers of CIS NCs stabilized by inorganic $(NH_4)_2S$ moieties were investigated. Under inert conditions, the NCs show little sintering at temperatures up to 450 °C. This contrasts with the clear NC grain growth observed upon annealing in the presence of gaseous hydrogen. We attribute the difference between both to the behaviour of the S^{2-} species. Under reducing atmosphere, the onset of sintering concurs with the release of H_2S, while under inert atmosphere, sulfide is retained in the film and oxidized, thereby inhibiting sintering. Importantly, the oxidized sulfur compounds can originate either from exposure to air or from the decomposition of solvent molecules during the annealing process itself. Similar findings apply to CZTSe and CdSe NCs, where nanocrystal sintering was equally inhibited under inert atmosphere. While the NC stabilization by $(NH_4)_2S$ moieties provides a way to stabilize CIS NCs in polar solvents while decreasing the carbon content and the inter particle distance in a NC thin film to a minimum, this lack of sintering is a considerable drawback for applications such as thin film photovoltaics that require dense thin films made from large crystallites. Annealing in a reducing atmosphere solves this problem only partially, since the crystal sizes obtained can compete with NCs stabilized by long, organic ligands. On the other hand, the inhibition of sintering by surface oxidation provides the opportunity to preserve nanocrystal properties throughout a high temperature annealing step. This can be of use for devices that rely on thin films of close packed nanocrystals, such as quantum dot - based solar cells and photodetectors.

Chapter IX

Towards absorber-quality CIS layers

In this final chapter, we develop and optimize CIGS precursor inks which ideally meet the following requirements:

- The precursor ink should keep a relatively long colloidal stability. This includes that compounds present in the ink are not altered as a function of time, and are stable under atmospheric conditions.
- The deposition of the ink should yield homogeneous, crack-free layers upon drying. Additionally, a single deposition step to reach the required thickness (µm range) is preferred.
- Annealing and/or selenization should transform the precursor to a dense, crack-free CIGS thin film with preferably large crystallites while keeping contamination to a minimum.

To reach these goals, we lean upon the results gathered in the precursor and ligand screening. First, we show that the formation of a homogeneous, crack-free layers is not as straightforward as one might suspect. Next, we demonstrate that additional grain growth during selenization can be achieved by addition of CuS NCs to $CuInS_2$ NCs. By inclusion of In salts, we aim to preserve this effect while adjusting the stoichiometry. Next to this, we show that we can also directly introduce Se in the ink as alternative to gas-phase selenization, which provides another approach to further reduce the costs of the process. Additionally, we present a $CuInSe_2$ thin film solar cells based on the use of our optimized precursors.

9.1 Experimental

Nanocrystal synthesis. CIS NCs were obtained according to the procedure described in 2.1.1 with the reaction temperature set at 240 ℃.

Nanocrystal processing. As-synthesized CIS and CuS NCs with oleylamine ligands were exchanged to $(NH_4)_2S$ as described in 6.1. The resulting solution in DMSO is used to deposit CIS NC thin films, by drop casting an amount corresponding to a dry thin film of approximately 1 µm onto a silicon substrate, on a heating plate at 60 ℃. Indium dithiocarbamate ($In(H_2N_2CS_2)_3$) is synthesized as described in chapter IV. Commercially available $InCl_3$ (Aldrich, 99.999 %) is used as such. Se nanoparticles are prepared according to the procedure in chapter IV, while NaHSe and $(N_2H_5)_2Se$ salts are obtained as described in chapter VI.

Characterization. (*in situ*) XRD and SEM-EDX measurements were performed according to the procedures described in chapter VII, performed by by Boris Capon, supervised by Prof. Dr. Christophe Detavernier at the Department of Solid-State Sciences of Ghent University.

Solar cell processing and characterization. Processing and characterization is done as described in chapter VII.

9.2 Morphology and reactivity enhancement

9.2.1 Thickness and composition

The solution-based processing of CIGS absorber layers for photovoltaic applications involves the deposition of a liquid onto a substrate. Along with the advantages including efficient material use and deposition under ambient conditions, this also gives rise to distinct problems compared to conventional co-evaporation methods. Typically, CIGS absorber layers are about 1-2 μm in thickness, and it is required that this layer is continuous over a large surface area. When the ink is deposited onto the substrate, the solvent evaporates while the precursor settles. The process of volume reduction during drying has been known to create stress

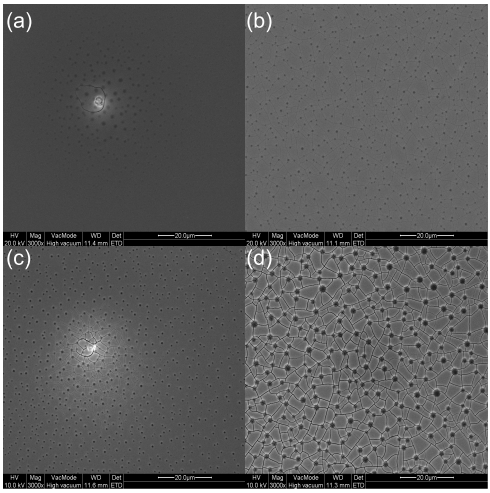

Figure 9.1: Top-view SEM images of dried thin films of $CuInS_2$ nanocrystals with hexanethiol ligands. As-deposited layer of 100 nm (a) and 500 nm (b). 100 nm (a) and 500 nm layers after annealing for 30 min at 200 °C.

in the thin film possibly resulting in crack formation [19–21]. Cracking, delamination and crystallization are processes that should be avoided during drying of any solution based precursor - nanoparticles, salts or mixtures of these. Moreover, a similar behaviour is possible during the subsequent annealing step. Here, volume reduction is realized by the evaporation or decomposition of any compound intolerable to the predominant conditions.

The conditions for NC solids to show cracks in an as-deposited thin film are dependent on a wide array of parameters. Among these are the NC size and the thickness of the thin film [22]. We illustrate this with $CuInS_2$ NCs deposited by drop casting. Here, as-synthesized CIS NCs with OLAm ligands were exchanged to hexanethiol ligands and dispersed in hexanethiol. The resulting inks were deposited on a Si substrate placed on a hot plate and a beaker was placed over the sample to slow down the drying. Dried, as-deposited thin films of CIS NCs are shown in Figure 9.1 with a thickness of 100 nm (a) and 500 nm (b). Both films appear smooth, while small cracks are spread throughout the entire range in the thicker film absent in the film of 100 nm. The problem with the formation of relatively thick, crack-free NC thin films have lead researchers to use layer-by-layer depositions approaches [5,11,23]. Here,

thin layers of NCs are deposited with a passivation of the layer in between subsequent deposition steps. This is meant to avoid the dissolution of the dried NC film during the next deposition and can be realized by annealing or ligand extraction. Layer-by-layer approaches are however a time consuming task and limited to lab scale demonstrations of devices.

As mentioned above, the removal of ligands from the dried NC film can also give rise to cracks. This is shown in Figure 9.1c-d, where the films in Figure9.1a-b were annealed at 200 °C for 30 min. Subsequently, both films show a drastic change in morphology, with the thickest film showing the widest cracks. It is clear that in an ideal case, crack-free CIGS precursor films could be deposited in a single deposition step, and the inevitable annealing and/or selenization step should give rise to crystal growth while removal of species should be kept to a minimum. In this way, by the combination of volume expansion and the limitation of volatile species, crack-free layers can be obtained.

9.2.2 $CuInS_2$-CuS NC inks

The stabilization of NCs with inorganic sulfide ligands, as described in chapter VI, offers a possible solution to keep contamination and volume reduction to a minimum in the formation of $CuInSe_2$ thin films. By the comparison of precursor systems in chapter VII, we learned that selenization is indispensable to achieve crystal growth, and the process of exchanging sulfur for selenium when starting from sulfide NC precursors induces lattice expansion. Cu-rich precursors are favored in terms of crystal growth during selenization.

We found that the combination of $CuInS_2$ and CuS NCs, stabilized by $(NH_4)_2S$, is a promising precursor in this regard. As shown in Figure 9.2b, selenization for 20 min at 550 °C gives rise to narrow XRD peaks conceding with chalcopyrite $CuInSe_2$. The *in situ* XRD in Figure 9.2a shows that crystal growth happens both during the ramping up period of the temperature and the dwell time. In Figure 9.2c, a top-view SEM image of the layer is presented after selenization. This clearly shown signs of a more reactive transformation behaviour compared to the precursors screened in chapter VII, as the layer is completely covered in large crystallites. However, from the cross-section SEM image in Figure 9.2d it appears that a bi-layer structure is formed, where only the top

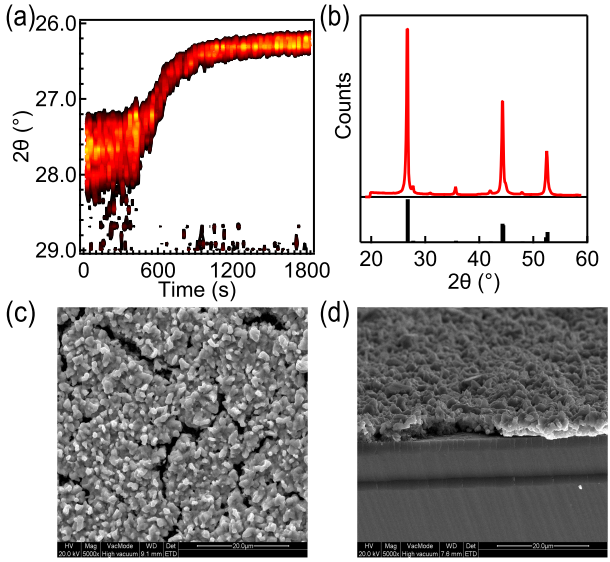

Figure 9.2: (a) *In situ* XRD pattern of a thin film during selenization of a combination of $cuins_2$ and CuS NCs. (b) XRD after selenization. Top view (c) and cross-section (d) SEM image of the obtained thin film.

layer is recrystallized. EDX measurements confirmed the absence of carbon and sulfur, and that the film has an excess of Cu as the Cu/In ratio was determined as 1.4.

In the processing of CIGS absorber layers by conventional co-evaporation methods, it has been demonstrated that Cu-rich conditions leads to additional grain growth, explained by the existence of a liquid Cu_xSe phase acting as a fluxing agent[16,24–26]. However, champion CIGS devices are overall Cu-poor, with a Cu/III ratio between 0.8-0.9.[27,28] While this is still a matter of debate, one explanation is the lack of Cu vacancies in Cu-rich devices, which are believed to be responsible for the p-type character of the CIGS absorber layer.

9.2.3 Stoichiometric hybrid inks

In order to compensate for the Cu-excess while maintaining the $CuInS_2$-CuS NC system as precursor, we choose to add indium containing salts to our precursor solutions. Since the NCs are dispersible in highly polar solvents like formamide and DMSO

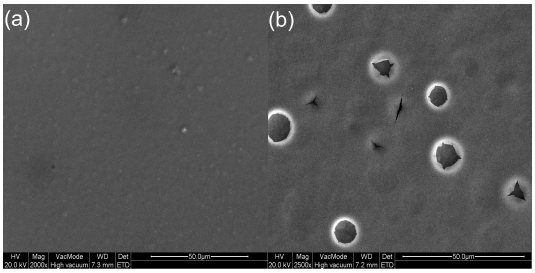

Figure 9.3: 1 µm thin films of as-deposited and dried precursors. (a) $CuInS_2$, CuS and $InCl_3$. (b) $CuInS_2$, CuS and In-dithiocarbamate.

due to the $(NH_4)_2S$ ligands, this is rather straightforward. Moreover, as demonstrated in chapter VI, addition of chloride anions to solutions of NCs increases the absolute value of the ζ-potential, hence increasing the colloidal stability. This translates into the formation of smooth, crack-free thin films as shown in Figure 9.3. Here, indium salts are added to solutions of $CuInS_2$ and CuS NCs capped with $(NH_4)_2S$ in DMSO, adjusted to a slightly total indium-rich composition. Besides $InCl_3$, we tested the use of In-dithiocarbamate ($In(H_2N_2CS_2)_3$). By drop casting the inks on Mo coated glass substrates and heating them in air on a hot plate at 70 °C 1 µm crack-free thin films could deposited in a single step. The morphology of the thin films containing the chloride precursor is superior to the dithiocarbamate precursor (Figure 9.3b).

We investigated the transformation behaviour of a precursor film consisting of $CuInS_2$, CuS and $InCl_3$, mixed in a molar ratio of 1:0.5:0.7. As shown in Figure 9.4a, two different thermal profiles were used, where one uses a faster ramping rate and a shorter dwell time compared to the other. In Figure 9.4b, XRD patterns are presented of the selenized films. The variation in thermal profile has a rather large consequence, since the film exposed to a longer ramp up and dwell time clearly shows the formation of $MoSe_2$, indicating that the Mo back contact is damaged by the selenium vapour. Moreover, the faster ramping and shorter dwell time leads to sharper XRD peaks, implying more crystal growth. The *in situ* XRD pattern presented in Figure 9.4c shows the transformation of the precursor during selenization using the prolonged thermal profile. We notice that a $CuInS_2$ phase is formed prior to the incorporation of selenium leading to $CuInSe_2$, and that the $MoSe_2$

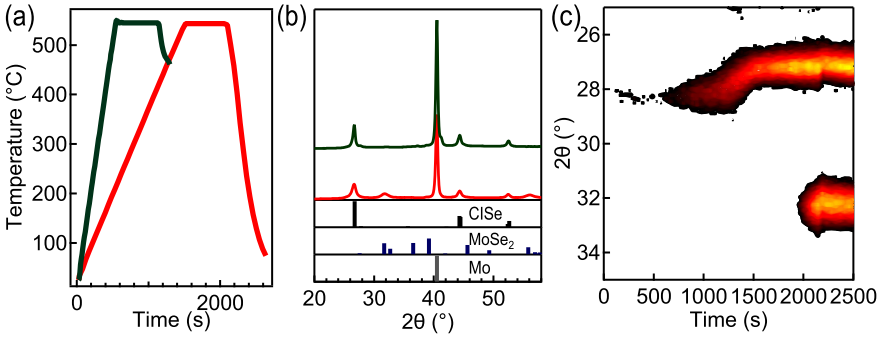

Figure 9.4: Selenization of the hybrid precursor $CuInS_2$, CuS and $InCl_3$. (a) Temperature profiles. (b) XRD patterns taken after selenization. The colours corresponds to the temperature profiles in (a). The database patterns for $CuInS_2$, $CuInSe_2$ and $MoSe_2$ are shown for comparison. (c) *in situ* XRD pattern of the film with the longest temperature profile showing the formation of $MoSe_2$.

phase appears during the last stage of the dwell time.

The use of $InCl_3$ leads to improved morphology of as-deposited thin films, while preserving the promising transformation properties of the $CuInS_2$/CuS NC system. At the same time, the Cu/In ratio, a crucial parameter towards the optical properties of the final layer, can be easily adjusted. Concurrently, chlorine is introduced in the system, which has possible impacts on the quality of the absorber layer. It is believed that incorporation of chlorine in $CuInSe_2$ layers increases the concentration of acceptors in the material slightly[29]. Guo *et al* stated that close to 1 at% chlorine is present in their $CuInSe_2$ absorbers[17], which originates from the salts used to synthesize the $CuInS_2$ NCs used in their work. This lead them to investigate the effect of different salts used in $CuInS_2$ NC synthesis on the efficiency of the final device[30]. Here, they found no significant difference in efficiency of $CuInSe_2$ absorbers with or without chlorine present.

In Table 9.1, EDX measurements are provided on a layer of as-deposited precursor. With respect to Cu, In and S, Cl represent 14.6 at% of the atoms present. The EDX analysis on a selenized layer reveals the complete disappearance of chlorine within the detection limits of EDX. Also, the complete exchange of sulfur for selenium is confirmed as expected from the shift in the XRD peak positions. Nevertheless, we investigated the effect of performing

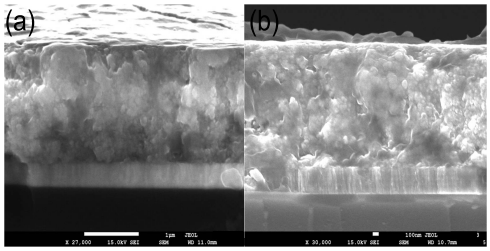

	Cu	In	S	Se	Cl
As-deposited	19.3	20.6	45.5	/	14.6
Selenized	24.2	25.8	/	50.1	/

Table 9.1: SEM-EDX analysis $CuInSe_2$ layers obtained by selenization of $CuInS_2$, CuS and $InCl_3$. (a) Cross-section SEM image of a selenized thin film. (b) Cross-section SEM image of a thin film annealed in N_2 followed by selenization. EDX values for the as-deposited precursor film and the selenized film are given in the table.

an annealing step prior to selenization. This step was carrier out at 200 °C in a nitrogen atmosphere, meant to remove volatile compounds prior to the actual transformation step. Figures a-b in Table 9.1 compare the cross-section SEM images of a layer without and with this pre-annealing step, respectively. The morphology and composition gathered by EDX analysis are equal in these 2 layers. However, the XRD patterns reveals that the layer with the pre-annealing step has superior crystallite size, as the FWHM of the (112) is 0.55° compared to 0.67°. This indicates that the annealing in nitrogen has a positive effect on the crystal growth during the selenization, possibly by densifying the precursor and removing volatile components.

9.3 Solar cell demonstration

Using the $CuInS_2$/CuS/$InCl_3$ precursor system, we managed to form a $CuInSe_2$ solar cell using a standard CIGS configuration (See experimental part). The precursor is deposited in a single deposition by drop casting, and the transformation to $CuInSe_2$ is carried out in a graphite box using elemental Se (500 °C 15 min). The precursor layer is shown in Figure 9.2a. As discussed above, one of the advantages of this hybrid ink is the smooth, micrometer-

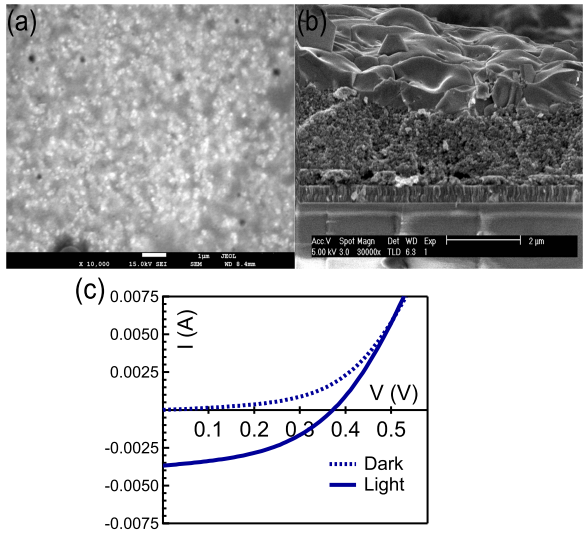

Area (cm^2)	J_{sc} (mA/cm^2)	V_{oc} (mV)	FF (%)	η (%)	R_{sh} (Ω/cm^2)	R_s (Ω/cm^2)
0.25	14.69	371.88	43.2	2.38	410.08	4.46

Table 9.2: (a) Top-view SEM image of the $CuInS_2/CuS/InCl_3$ precursor layer. (b) Cross-section SEM image of the selenized precursor. (c) I-V measurements obtained after finishing the solar cell device. The solar cell parameters obtained on a 0.25 cm^2 area are outlined in the table.

thick layers that can be formed using a single deposition step. A cross-section SEM image of the glass/Mo/$CuInSe_2$ structure is shown in Figure 9.2b. Here, we notice that only the top layer is recrystallized, while the bottom layer shows a rather porous structure. The total $CuInSe_2$ thickness is about 2 µm, and the Cu:In ratio was measured as 1.1 by EDX. The I-V curves of this layer are presented in Figure 9.2c, with the solar cell parameters outlined in the table below. We calculated a total area efficiency of 2.38 % on a 0.25 cm^2 area. Also here, the $CuInSe_2$ layer can still be further optimized, by for instance pre-annealing to enhance the crystal growth during selenization, adjusting the stoichiometry towards Cu-poor (as Cu-rich CIGS layers are typically inferior in terms of efficiency[16,26]), and the use of harsher selenization conditions.

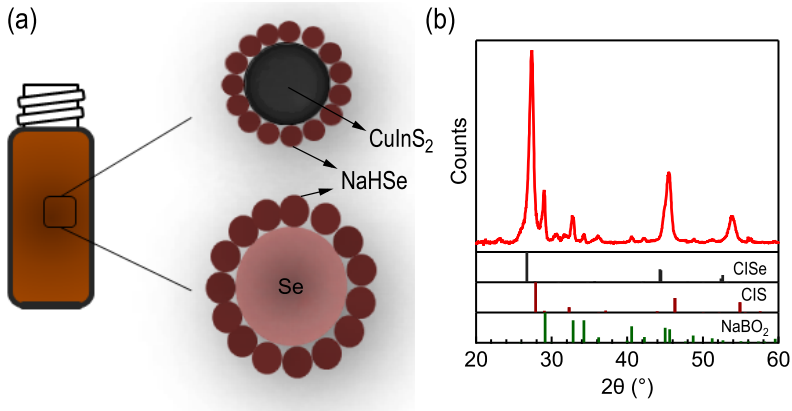

Figure 9.5: (a) Scheme of the contents of the ink/thin film. (b) XRD pattern taken after annealing in He. The database patterns for $NaBO_2$ and chalcopyrite $CuInS_2$/$CuInSe_2$ are added for comparison.

9.4 Se-containing inks

In the past chapters, it has become clear that gas-phase selenization is indispensable to achieve crystal growth during the transformation of solution-based precursors. In fact, few reports have shown decent CIGS layers obtained without using this step. Most notably, Todorov *et al*[31] describes the best CIGS solar cell (15.2 %) up to date using a solution-based approach. Here, metal sulfides and selenides are dissolved in pure hydrazine along with additional sulfur and selenium. The CIGS layer is built up by spin-coating this solution and annealing at 540 °C in between subsequent coatings inside a nitrogen filled glove box. The major downside of this approach is the use of pure hydrazine, which is an extremely hazardous chemical, along with the need of subsequent annealing steps in between coatings.

Our approach to include an excess of selenium in the ink and, consequently, in the precursor thin film is twofold. First, we are able to synthesize selenium nanoparticles (NPs) and make them compatible with polar inks (chapter IV). Also, we described a convenient preparation of selenium-containing salts starting from elemental selenium (Chapter VI). Both $CuInS_2$ NCs and Se NPs can be stabilized using the aforementioned salts and therefore combined in a single solvent. In this exploratory analysis, we aim to

find out if the selenium-containing salts and nanoparticles can act as a source of selenium similar to conventional gas-phase selenization. Therefore, we combine $CuInS_2$ NCs with Se anions and Se NPs and anneal this hybrid precursor in an inert atmosphere.

In a first attempt to selenize $CuInS_2$ NCs with the use of Se incorporated in the ink, we stabilized both CIS NCs and Se NPs using NaHSe. By determining the volume fraction of CIS in the ink, we were able to calculate the total amount of sulfur. By elemental analysis using XRF, we combined inks of CIS NCs and Se NPs to achieve a S/Se ratio of 1/5 in the precursor film. The amount of selenium originating from the Se NPs is estimated at 10 % of the total amount of Se. The combination of inks is schematically presented in Figure 9.5a. Annealing this thin film for 30 min at 450 ℃ in a helium flow results in a partially selenized $CuIn(S,Se)_2$ phase as shown in Figure 9.5b. We notice that Se is incorporated in $CuInS_2$ by the partial shift to lower 2θ values - hence, lattice expansion - from the $CuInS_2$ NC phase to $CuInSe_2$. Furthermore, we notice peaks in the XRD pattern that we can assign to a $NaBO_2$ phase (most notably at 29.0° and 32.8°). We conclude that the use of NaHSe as a selenium source, although providing a selenization effect, is not ideal as secondary phases are formed.

Besides NaHSe, a second option is the use of $(N_2H_5)_2Se$ to stabilize both CIS NCs and Se NPs. This system is comparable to the precursor ink in Figure 9.5a where NaHSe is substituted by $(N_2H_5)_2Se$. Furthermore, we evaluate the addition of Se NPS by also annealing thin films with $(N_2H_5)_2Se$ as sole selenium source. Figure 9.3a shows an *in situ* XRD pattern of a thin film consisting of solely CIS NCs, stabilized by $(N_2H_5)_2Se$, with an extra amount of $(N_2H_5)_2Se$ added to achieve a 1/5 S/Se ratio. Here, the film is heated under a nitrogen flow in a tube furnace. We notice that the $CuInS_2$ NC peak (27.9°) completely shifts to $CuInSe_2$ (26.7°) already during the heating period, while prolonged heating gives rise to sharpening of the (112) peak. After annealing, an XRD pattern is shown in Figure 9.3b (red). We notice that the peaks indeed coincide with chalcopyrite $CuInSe_2$, and an additional In_2O_3 phase is formed. This can be observed in the *in situ* pattern. From 1250 s onward, a peak starts to appear at 31° while gradually the intensity of the (112) peak of $CuInSe_2$ decreases. We were able to prevent the appearance of this oxide phase by employing a 5 % H_2/Ar atmosphere rather than an inert atmosphere to anneal

the same precursor with the same thermal program (Figure 9.3b, blue pattern). This leads to not only a pure $CuInSe_2$ phase from $CuInS_2$ NCs, it also shows additional sharpening and thus crystal growth.

Next, we examine the addition of Se/$(N_2H_5)_2$Se NPs to the CIS/$(N_2H_5)_2$Se NC system. Shown in the inset in Figure 9.3b is the (112) peak of samples after annealing in H_2/Ar, where the same excess of selenium is present in the precursor system with respect to sulfur. Again, the amount of selenium originating from the NPs is estimated at 10 %. We notice that although both system give rise to a full exchange of sulfur to selenium during annealing, crystal growth is enhanced when part of the selenium is present as selenium NPs. An overview of crystal sizes obtained from Scherrer analysis is given in Table 9.3. Despite the fact that the selenium in the Se NPs present a small amount compared to the total amount, it clearly has a positive influence on the crystal growth during the transformation both in inert and reducing atmosphere.

Based on our initial attempts and analysis, we suggest a number of possible actions to optimize this precursor system.

- SEM-EDX analysis of both the precursor layer and the transformed $CuIn(S,Se)_2$ layer. This should provide further knowledge and conformation of the stoichiometry, more specifically the S/Se ratio in both systems. Moreover, the morphology and thickness could be evaluated and optimized.

- Our best results are obtained using a tube furnace with an inert or reducing gas flow. Even though this shows the potential of selenization without a selenium atmosphere, we hypothesize that a partial or complete encapsulation would enhance the sintering/selenization because it could prevent selenium evaporation and loss in the gas flow.

- The use of optimized precursor systems, which provide additional reactivity as shown in the $CuInS_2$/CuS(/$InCl_3$) precursor.

Our conclusion from this preliminary study is that a full selenization effect can be established by inclusion of selenium in the precursor ink, by using Se NPs and selenium-containing salts. The resulting thin films show promising crystal growth, which can be

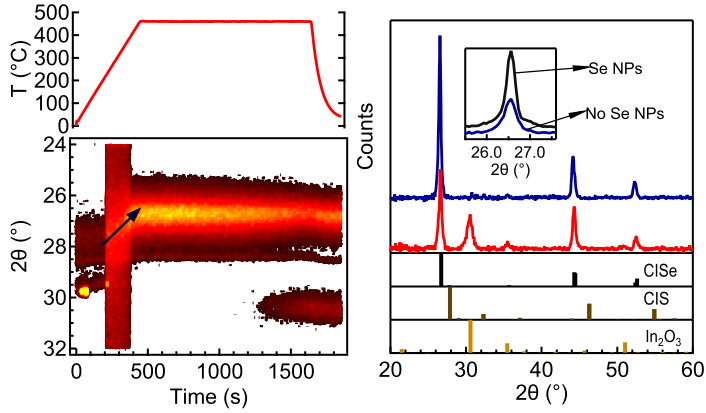

System	Atmosphere	Crystal size (nm)
CIS/Se	He	24.0
	H_2	26.4
CIS/Se + Se/Se	He	28.2
	H_2	31.4

Table 9.3: Annealing of CIS/$(N_2H_5)_2$Se. (a) Thermal profile and *in situ* XRD pattern of CIS/$(N_2H_5)_2$Se in He. (b) XRD patterns taken of CIS/$(N_2H_5)_2$Se after annealing in He (red) and H_2/Ar (blue). Database patterns for $CuInS_2$, $CuInSe_2$ and In_2O_3 are added for comparison. Inset in (b): zoom on (112) peak of annealed samples of CIS/$(N_2H_5)_2$Se (blue) and CIS/$(N_2H_5)_2$Se + Se/$(N_2H_5)_2$Se in H_2/Ar.

further enhanced by employing a reducing atmosphere and possibly adjusting the amount of selenium originating from nanoparticles and salts.

9.5 Conclusions

In this final chapter, we have combined our results from the synthesis, analysis of surface chemistry and transformation of CIGS precursors to present solutions for common problems encountered in the solution-based deposition of CIGS absorber layers. We were able to introduce reactivity during the selenization by the addition of binary CuS NCs, and compensate for the stoichiometry by the addition of indium salts. These indium salts provide easy tuning of the stoichiometry and are compatible with the polar solvents

used in the processing of NCs capped by inorganic anions. Moreover, we have shown that the anions of the indium containing salts provide additional colloidal stabilization to the NCs, leading to an improved morphology of the as-deposited layer which can be deposited in a thickness above 1 µm in a single deposition step. The combination of NCs with salts leads to a hybrid precursor, showing full transformation towards $CuInSe_2$ in relatively mild selenization conditions. The crystal growth during selenization is promising, and can be further enhanced by applying a pre-annealing step. In this way, the hybrid precursor we present in this chapter resolves most issues with solution-based deposition with respect to contamination and deposition. We managed to demonstrate a thin film solar cell device starting from this precursor showing a promising efficiency of 2.38 %, and stress that there is room for optimization.

Apart from this, we explored the inclusion of selenium in the precursor ink in an attempt to bypass the need for gas-phase selenization and consequently simplifying the process from precursor to dense layer. Our study clearly shows that the addition of selenium to $CuInS_2$ NCs creates a selenization effect during annealing in a selenium-free atmosphere. We were able to eliminate secondary phases and enhance the crystal growth during this process. In this exploratory study, we have provided suggestions to improve this type of selenization. We conclude that the addition of selenium both in the form of Se NPs and selenium-containing salts is very promising to mimic the cumbersome gas-phase selenization step employed in most solution-based approaches.

Bibliography

[1] Johnston, K. W.; Pattantyus-Abraham, A. G.; Clifford, J. P.; Myrskog, S. H.; MacNeil, D. D.; Levina, L.; Sargent, E. H. Schottky-quantum dot photovoltaics for efficient infrared power conversion. *Applied Physics Letters* **2008**, *92*, 151115.

[2] Seo, J.; Kim, S. J.; Kim, W. J.; Singh, R.; Samoc, M.; Cartwright, A. N.; Prasad, P. N. Enhancement of the photovoltaic performance in PbS nanocrystal:P3HT hybrid composite devices by post-treatment-driven ligand exchange. *Nanotechnology* **2009**, *20*, 095202.

[3] Kuo, C.-Y.; Su, M.-S.; Ku, C.-S.; Wang, S.-M.; Lee, H.-Y.; Wei, K.-H. Ligands affect the crystal structure and photovoltaic performance of thin films of PbSe quantum dots. *Journal of Materials Chemistry* **2011**, *21*, 11605.

[4] Zarghami, M. H.; Liu, Y.; Gibbs, M.; Gebremichael, E.; Webster, C.; Law, M. p-Type PbSe and PbS quantum dot solids prepared with short-chain acids and diacids. *ACS nano* **2010**, *4*, 2475–85.

[5] Luther, J. M.; Law, M.; Song, Q.; Perkins, C. L.; Beard, M. C.; Nozik, A. J. Structural, optical, and electrical properties of self-assembled films of PbSe nanocrystals treated with 1,2-ethanedithiol. *ACS nano* **2008**, *2*, 271–80.

[6] Klem, E. J. D.; Shukla, H.; Hinds, S.; MacNeil, D. D.; Levina, L.; Sargent, E. H. Impact of dithiol treatment and air annealing on the conductivity, mobility, and hole density in PbS colloidal quantum dot solids. *Applied Physics Letters* **2008**, *92*, 212105.

[7] Porter, V.; Geyer, S. Photoconduction in annealed and chemically treated CdSe/ZnS inorganic nanocrystal films. *The Journal of Physical Chemistry C* **2008**, *112*, 2308–2316.

[8] Webber, D. H.; Brutchey, R. L. Ligand exchange on colloidal CdSe nanocrystals using thermally labile tert-butylthiol for improved photocurrent in nanocrystal films. *Journal of the American Chemical Society* **2012**, *134*, 1085–92.

[9] Guo, Q.; Ford, G. M.; Yang, W.-C.; Walker, B. C.; Stach, E. a.; Hillhouse, H. W.; Agrawal, R. Fabrication of 7.2% Efficient CZTSSe Solar Cells Using CZTS Nanocrystals. *Journal of the American Chemical Society* **2010**, *132*, 17384–17386.

[10] Cao, Y.; Denny, M. S.; Caspar, J. V.; Farneth, W. E.; Guo, Q.; Ionkin, A. S.; Johnson, L. K.; Lu, M.; Malajovich, I.; Radu, D.; Rosenfeld, H. D.; Choudhury, K. R.; Wu, W. High-Efficiency Solution-Processed $Cu_2ZnSn(S,Se)_4$ Thin-Film Solar Cells Prepared from Binary and Ternary Nanoparticles. *Journal of the American Chemical Society* **2012**, *134*, 15644–7.

[11] Jasieniak, J.; MacDonald, B. I.; Watkins, S. E.; Mulvaney, P. Solution-processed sintered nanocrystal solar cells via layer-by-layer assembly. *Nano letters* **2011**, *11*, 2856–64.

[12] Drndic, M.; Jarosz, M. V.; Morgan, N. Y.; Kastner, M. a.; Bawendi, M. G. Transport properties of annealed CdSe colloidal nanocrystal solids. *Journal of Applied Physics* **2002**, *92*, 7498.

[13] Nag, A.; Kovalenko, M. V.; Lee, J.-S.; Liu, W.; Spokoyny, B.; Talapin, D. V. Metal-free inorganic ligands for colloidal nanocrystals: S^{2-}, HS^-, Se^{2-}, HSe^-, Te^{2-}, HTe^-, $TeS_3{}^{2-}$, OH^-, and $NH_2{}^-$ as surface ligands. *Journal of the American Chemical Society* **2011**, *133*, 10612–20.

[14] Hibberd, C. J.; Chassaing, E.; Liu, W.; Mitzi, D. B.; Lincot, D.; Tiwari, a. N. Non-vacuum methods for formation of Cu(In, Ga)(Se, S)$_2$ thin film photovoltaic absorbers. *Progress in Photovoltaics: Research and Applications* **2010**, *18*, 434–452.

[15] Brummer, a.; Honkimäki, V.; Berwian, P.; Probst, V.; Palm, J.; Hock, R. Formation of $CuInSe_2$ by the annealing of stacked elemental layers-analysis by in situ high-energy powder diffraction. *Thin Solid Films* **2003**, *437*, 297–307.

[16] Larsen, J. K.; Gutay, L.; Siebentritt, S. Influence of secondary phase Cu_2Se on the optoelectronic quality of chalcopyrite thin films. *Applied Physics Letters* **2011**, *98*, 201910.

[17] Guo, Q.; Ford, G. G. M.; Hillhouse, H. W. H.; Agrawal, R. Sulfide nanocrystal inks for dense $Cu(In_{1-x}Ga_x)(S_{1-y}Se_y)_2$ absorber films and their photovoltaic performance. *Nano letters* **2009**, *9*, 3060–5.

[18] *NIST Standard Reference Database, Version 4.1*; Technical Report.

[19] Hillhouse, H. W.; Beard, M. C. Solar cells from colloidal nanocrystals: Fundamentals, materials, devices, and economics.

Current Opinion in Colloid & Interface Science **2009**, *14*, 245–259.

[20] Talapin, D. V.; Lee, J.-S.; Kovalenko, M. V.; Shevchenko, E. V. Prospects of colloidal nanocrystals for electronic and optoelectronic applications. *Chemical reviews* **2010**, *110*, 389–458.

[21] Todorov, T.; Mitzi, D. B. Direct Liquid Coating of Chalcopyrite Light-Absorbing Layers for Photovoltaic Devices. *European Journal of Inorganic Chemistry* **2010**, *2010*, 17–28.

[22] Singh, K.; Tirumkudulu, M. Cracking in Drying Colloidal Films. *Physical Review Letters* **2007**, *98*, 1–4.

[23] Tang, J.; Kemp, K. W.; Hoogland, S.; Jeong, K. S.; Liu, H.; Levina, L.; Furukawa, M.; Wang, X.; Debnath, R.; Cha, D.; Chou, K. W.; Fischer, A.; Amassian, A.; Asbury, J. B.; Sargent, E. H. Colloidal-quantum-dot photovoltaics using atomic-ligand passivation. *Nature materials* **2011**, *10*, 765–71.

[24] Siebentritt, S.; Igalson, M.; Persson, C.; Lany, S. The electronic structure of chalcopyrites-bands, point defects and grain boundaries. *Progress in Photovoltaics: Research and Applications* **2010**, *18*, 390–410.

[25] Witte, W.; Kniese, R.; Powalla, M. Raman investigations of $Cu(In,Ga)Se_2$ thin films with various copper contents. *Thin Solid Films* **2008**, *517*, 867–869.

[26] Hsieh, T.-P.; Chuang, C.-C.; Wu, C.-S.; Chang, J.-C.; Guo, J.-W.; Chen, W.-C. Effects of residual copper selenide on $CuInGaSe_2$ solar cells. *Solid-State Electronics* **2011**, *56*, 175–178.

[27] Repins, I.; Contreras, M. A.; Egaas, B.; DeHart, C.; Scharf, J.; Perkins, C. L.; To, B.; Noufi, R. 19.9%-efficient $ZnO/CdS/CuInGaSe_2$ solar cell with 81.2% fill factor. *Progress in Photovoltaics: Research and Applications* **2008**, *16*, 235–239.

[28] Jackson, P.; Hariskos, D. New world record efficiency for $Cu(In,Ga)Se_2$ thin-film solar cells beyond 20%. *Progress in Photovoltaics: Research and Applications* **2011**, *19*, 894–897.

[29] Kauk, M.; Altosaar, M.; Raudoja, J.; Timmo, K.; Varema, T.; Danilson, M.; Grossberg, M.; Mellikov, E. The influence of doping with donor type impurities on the properties of

CuInSe2. *Physica Status Solidi (C) Current Topics in Solid State Physics* **2008**, *5*, 609–611.

[30] Ford, G. M.; Guo, Q.; Agrawal, R.; Hillhouse, H. W. $CuIn(S,Se)_2$ thin film solar cells from nanocrystal inks: Effect of nanocrystal precursors. *Thin Solid Films* **2011**, *520*, 523–528.

[31] Todorov, T. K.; Gunawan, O.; Gokmen, T.; Mitzi, D. B. Solution-processed $Cu(In,Ga)(S,Se)_2$ absorber yielding a 15.2% efficient solar cell. *Progress in Photovoltaics: Research and Applications* **2012**, *21*, 82–87.

English Summary

Solution-based deposition of Cu(In,Ga)(S,Se)$_2$ (CIGS) absorber layers offers a promising approach to substantially lower the cost of the production of CIGS thin film solar cells, provided the solar cell efficiency is not drastically lowered compared to conventional, vacuum-based methods. The inks used in solution-based processing consists of nanoparticles, salts and/or molecules. By employing a thermal annealing step, these precursors are transformed towards dense CIGS absorber layers. In this thesis, we explore the rich chemistry of these inks, with a focus on colloidal nanocrystals (NCs) as precursors. Both the synthesis and surface chemistry is closely examined with the goal to optimize both with respect to the application. Later, we screen the transformation of these precursors and investigate the relation between the transformation and the surface chemistry and demonstrate thin film solar cells based on our optimized procedures.

9.6 Precursor synthesis

In chapter II, we use a heating-up method to synthesize $CuInS_2$ (CIS), CuS and In_2S_3 NCs. We gain insight in the reaction pathway of ternary NCs trough elemental analysis of the reaction development. Here, we demonstrate that CIS NC formation is preceded by nucleation of Cu_xS NCs followed by gradual incorporation of In in the existing NCs. The reaction yield is optimized and we present routes to obtain different sizes and shapes of CIS NCs. Furthermore, our optimized heating-up procedure allows us to obtain CIS NCs at full yield within minutes after mixing the precursors.

Compared to sulfides, binary and ternary selenides of the $CuInSe_2$ (CISe) system are more challenging NCs to synthesize. Chapter III presents a novel approach which is based on the hot

injection of elemental selenium powder, heterogeneously dispersed in a carrier liquid, to a solution of cation precursors in oleylamine (OLAm). Compared to existing synthesis procedures that make use of elemental selenium, e.g., to form CISe and $Cu_{2-x}Se$ NCs, this leads to a fast and close to full yield conversion of precursors into NCs. In addition, the method can be extended to the formation of In_2Se_3 NCs - a material for which little or no low-cost routes have been described - which again results in a fast and close to full yield reaction.

Apart from colloidal NCs, we consider metal dithiocarbamates as precursors for CIGS. In chapter IV, we synthesize Cu and In dithiocarbamate complexes with a simple, inexpensive and up scalable precipitation reaction in water. The resulting complexes are characterized with respect to transformation and we demonstrate their decomposition towards metal sulfide thin films. In addition, the synthesis of selenium nanoparticles (NPs) by a microemulsion process is presented. We developed a procedure to extract the organics from the NP and replace them by sulfide of selenide salts. In this way, a chalcogen excess can be added to our precursor inks without introducing additional contamination.

9.7 Surface chemistry

With organic ligands as inherent parts of as-synthesized colloidal nanocrystals, the aim of this part is to understand and tune the unexplored surface chemistry of CIS NCs. In chapter V, we start by examining CIS NCs synthesized using amines by employing the Nuclear Magnetic Resonance (NMR) toolbox for nanocrystal surface chemistry analysis. It is found that as-synthesized CIS NCs provide a first example of stoichiometric NCs with tightly bound, L-type amines, in contrast with the dynamic stabilization typically found in other NC systems. Our results are put in the framework of the covalent bond classification method. Moreover, a relatively straightforward approach to distinguish L-type from X-type binding by combining *in situ* heating up with solution NMR spectroscopy is introduced. The strong binding of L-type ligands has the consequence that exchanging the original amine ligands for others ligands requires relatively high temperatures and successive exchange steps, along with the ability of the new ligand to bind as L-type. This is demonstrated by performing ligand ex-

change reaction towards thiols and acids, where only thiols could be found on the NC surface after several exchange steps. In addition, we demonstrate that the use of technical grade OLAm, which is widely used in colloidal NC synthesis, leads to nonstoichiometric CIS NCs capped by a combination of L-type OLAm and X-type impurities. Here, we believe that impurities present in technical grade OLAm are responsible for the difference in surface chemistry compared to NCs synthesized using ODAm.

A drastically distinct way to stabilize colloidal NCs is by using inorganic ligands, a strategy which has recently gained interest. In chapter VI, we apply this to colloidal NCs of the CIGS system and present novel methods to synthesize these ligands. The synthesis of these salts uses a milder chemistry compared to established methods using pure hydrazine. The ligand exchange process of organic to inorganic ligands is analyzed using NMR spectroscopy, demonstrating a successful exchange. We pay attention to the colloidal stability of the obtained solutions and introduce the addition of chloride salts to drastically improve the shelf-life of these colloidal NCs.

9.8 Film formation and transformation

The step from precursor thin film towards a dense $CuInSe_2$ absorber layer is the focus in the last part. Chapter VII provides an investigation on the differences in thermal annealing behaviour of ternary and mixtures of binary colloidal NCs. Here, we compare the reactivity of the annealing/sintering process towards $CuInSe_2$. Between the ternary $CuInSe_2$ and $CuInS_2$ NCs, the selenization of the latter is clearly more reactive likely owing to the exchange of sulfur for selenium. It is shown that during the selenization of binary sulfides, the reactivity greatly depends on the stoichiometry, and can be easily tuned by the relative amounts of CuS NCs to In_2S_3 NCs. A Cu-rich stoichiometry is clearly preferred during transformation, giving rise to larger $CuInSe_2$ crystallite sizes. Using binary selenides as a precursor system, we confirmed that selenization has a positive impact on the transformation compared to an inert atmosphere. These binary selenides are preferred over ternary selenides, and provide the largest final crystallite sizes. Next, we alter the surface chemistry on CIS NCs to establish a relation between the amount of carbon surrounding the NCs in

the precursor ink, the sintering behaviour and the contamination present in the final layer. We observed that different ligand capping give rise to significant differences in the degree of sintering. Additionally, we have demonstrated the potential of selenization of CIS NCs towards $CuInSe_2$ thin film solar cells. With room for optimization, a cell efficiency of 1.38 % is presented.

The observation that inorganic sulfide ligands prevent the sintering of CIS NCs compared to long organic ligands provides the starting point for Chapter VIII. Under inert conditions, the NCs show little sintering at temperatures up to 450 °C. This contrasts with the clear NC grain growth observed upon annealing in the presence of gaseous hydrogen. We thoroughly investigate this difference and attribute it to the behaviour of the S^{2-} species present on the surface of the CIS NCs. Under reducing atmosphere, the onset of sintering concurs with the release of H_2S, while under inert atmosphere, sulfide is retained in the film and oxidized, thereby inhibiting sintering. Oxidized sulfur compounds can both originate from exposure to air or from the decomposition of remaining solvent molecules during the annealing process itself. We expose that the same findings apply to other NC systems as well, which provides a challenge when the aim is to sinter the NCs, yet an opportunity when the NC properties should be preserved at elevated temperatures.

In the final chapter IX, we have combined our results from the synthesis, analysis of surface chemistry and transformation of CIGS precursors to present solutions for common problems encountered in the solution-based deposition of CIGS absorber layers. Additional reactivity during selenization of CIS NCs is introduced by employing CuS NCs. To preserve an optimal stoichiometry, we propose the use of indium salts, which also provide additional colloidal stabilization leading to crack-free, smooth thin films. This combined precursor - so-called *hybrid precursor* - leads to full transformation during selenization towards $CuInSe_2$ employing relatively mild selenization conditions. We show that the crystal growth can be further enhanced by applying a pre-annealing step. We managed to demonstrate a thin film solar cell device starting from this precursor showing a promising efficiency of 2.38 %, and stress that there is room for optimization. Next to this, we explored the inclusion of selenium in the precursor ink in an attempt to bypass the need for gas-phase selenization and

consequently simplifying the process from precursor to dense layer. Our preliminary results in this respect clearly shows that selenium addition to $CuInS_2$ creates a selenization effect during the annealing in a selenium-free atmosphere. We conclude that the addition of selenium both in the form of Se NPs and selenium-containing salts is very promising to mimic the cumbersome gas-phase selenization step employed in most solution-based approaches.

Nederlandstalige Samenvatting

Het gebruik van oplossingen (inkten) voor de depositie van $Cu(In,Ga)(S,Se)_2$ (CIGS) lichtabsorberende lagen biedt een veelbelovende manier om de productiekost van CIGS dunne-film zonnecellen significant te verlagen. De efficiëntie van de finale zonnecel mag hierbij niet drastisch verlaagd wordt tegenover conventionele, vacuüm gebaseerde methoden. De inkten die gebruikt worden bevatten nanopartikels, zouten en/of moleculen. Door het gebruik van thermisch annealen worden deze precursoren omgezet naar lichtabsorberende CIGS lagen. In dit werk verkennen we de rijke chemie van deze inkten, met focus op colloïdale nanokristallen (NCs) als precursoren. Zowel de synthese als de oppervlakchemie van deze precursoren wordt uitgebreid onderzocht in dit werk. Verder onderzoeken we de omzetting van deze precursoren naar dense CIGS lagen, analyzeren we de relatie tussen de transformatie en de oppervlakchemie, en demonstreren we werkende dunne-film zonnecellen gebruik makende van onze procedures.

9.9 Synthese van precursoren

In Hoofdstuk II beschrijven we de synthese van $CuInS_2$ (CIS), CuS en In_2S_3 NCs door middel van het opwarmen van precursoren. Gebruik makende van elementanalyse verkrijgen we informatie over de kinetiek van de reactie die leidt tot ternaire NCs. Hierdoor demonstreren we dat de vorming van CIS NCs voorafgegaan wordt door de nucleatie van Cu_xS NCs gevolgd door geleidelijke opname van indium in de reeds gevormde NCs. De opbrengst van de reactie werd verbeterd en we presenteren mogelijkheden die de synthese van verschillende groottes en vormen van CIS NCs toelaten. Bovendien maakt onze geoptimalizeerde procedure het mogelijk om

CIS NCs met een volledige opbrengst te verkrijgen binnen enkele minuten na het mengen van de precursoren.

Vergeleken met sulfiden is de synthese van binaire en ternaire seleniden van het $CuInSe_2$ (CISe) systeem minder eenvoudig. In Hoofdstuk III beschrijven we hiervoor een nieuwe strategie, gebaseerd op de injectie van selenium poeder, heterogeen gedispergeerd in een drager vloeistof, aan een oplossing van kation precursoren in oleylamine (OLAm). Vergeleken met reeds bestaande synthese procedures die gebruik maken van elementair selenium, bijvoorbeeld voor CISe en $Cu_{2-x}Se$ NCs, leidt dit tot een snelle en nagenoeg volledige omzetting van precursoren tot NCs. Hiernaast kan deze methode gebruikt worden voor de vorming van In_2Se_3 NCs - een materiaal waarvoor weinig tot geen goedkope routes reeds beschreven zijn - wat opnieuw tot een snelle en volledige reactie leidt.

Naast colloïdale NCs beschouwen we ook metaal dithiocarbamaten als precursoren voor CIGS. In Hoofdstuk IV beschrijven we de synthese van Cu en In dithiocarbamaat complexen met een eenvoudige, goedkope en opschaalbare neerslagreactie in water. De resulterende complexen worden gekarakterizeerd met de nadruk op transformatie en we demonstreren de decompositie naar metaal sulfide dunne filmen. Hiernaast rapporteren we een synthese van selenium nanopartikels (NPs) door middel van een micro emulsie proces. We ontwikkelen een proces waarbij de organische moleculen geëxtraheerd worden van het NP en vervangen worden door sulfide of selenide zouten. Op deze manier kan een overmaat selenium toegevoegd worden aan de precursor inkten waarbij verontreining vermeden wordt.

9.10 Oppervlakchemie

Organische liganden zijn inherent deel van colloïdale NCs. Het doel van dit deel is het begrijpen en afstemmen van de onontgonnen oppervlakchemie van CIS NCs. In Hoofdstuk V starten we met het onderzoeken van CIS NCs gesynthetizeerd met amines door middel van nucleare magnetische resonantiespectroscopie (NMR) technieken voor het analyzeren van de oppervlaktechemie van nanokristallen. Hierdoor vinden we dat gesynthetizeerde CIS NCs een eerste voorbeeld verstrekken van stoichiometrische NCs met sterk gebonden, L-type amines, in contrast met de dynami-

sche stabilizatie die typisch gevonden wordt in andere NC systemen. Onze resultaten worden geplaatst in het kader van de covalente binding classificatie methode. Bovendien introduceren we een eenvoudige methode voor het onderscheiden van L-type en X-type binding door op te warmen tijdens de NMR meting. Het gevolg van de sterke binding van L-type liganden is dat de uitwisseling van het origineel amine naar andere liganden relatief hoge temperaturen en meerdere stappen vereist, naast de voorwaarde dat het nieuwe ligand als L-type kan binden. Dit demonstreren we door de liganduitwisseling door te voeren naar thiolen en zuren, waarbij enkel thiolen op het NC oppervlak gevonden worden na meerdere stappen. Bovendien tonen we dat het gebruik van technisch OLAm, veelvuldig gebruikt in NC synthese, leidt tot niet-stoichiometrische CIS NCs gestabilizeerd door een combinatie van L-type OLAm en X-type onzuiverheden. We schrijven dit verschil in oppervlakchemie toe aan de onzuiverheden die oorspronkelijk aanwezig zijn in het technisch OLAm.

Een alternatieve manier om colloïdale NCs te stabilizeren is het gebruik van anorganische liganden, een strategie die onlangs aan aandacht gewonnen heeft. In Hoofdstuk VI passen we deze methode toe op colloïdale NCs van het CIGS systeem en beschrijven we nieuwe manieren om deze liganden te produceren. Het proces van organische naar anorganische liganden wordt bestudeerd waarbij we een succesvolle uitwisseling tonen door middel van NMR spectroscopie. We besteden hierbij aandacht aan de colloïdale stabiliteit en introduceren het toevoegen van chloride zouten om de houdbaarheid van deze NCs drastisch te verhogen.

9.11 Filmvorming en transformatie

De stap van precursor dunne film naar $CuInSe_2$ lichtabsorberende laag is de focus in dit laatste deel. In Hoofdstuk VII onderzoeken we het verschil in thermisch anneal gedrag van ternaire en mengsels van binaire colloïdale NCs. Hier vergelijken we de reactiviteit van het anneal/sinter proces naar $CuInSe_2$. Tussen ternaire $CuInSe_2$ en $CuInS_2$ NCs is de selenizatie van de laatste duidelijk meer reactief wat we toeschrijven aan de uitwisseling van zwavel door selenium. We tonen aan dat tijdens de selenizatie van binaire sulfiden de reactiviteit sterk afhangt van de stoichiometrie, die kan aangepast worden door de relatieve hoeveelheid van CuS NCs te-

genover In_2S_3 NCs. Een Cu-rijke stoichiometrie wordt duidelijk geprefereerd tijdens de transformatie, wat aanleiding geeft tot grotere $CuInSe_2$ kristallieten. Bij het gebruik van binaire seleniden als precursor systeem bevestigen we dat selenizatie een positieve invloed heeft op de transformatie vergeleken met inerte atmosfeer. Deze binaire seleniden worden verkozen boven ternaire seleniden, en geven aanleiding tot de grootste finale kristalgroottes.

Vervolgens veranderen we de oppervlakchemie van CIS NCs om een relatie te bevestigen tussen de hoeveelheid koolstof rond de NCs in de precursor inkt, het sinter gedrag en de onzuiverheden in de finale laag. We nemen waar dat verschillende liganden aanleiding geven tot significante verschillen in de graad van sintering. Hiernaast hebben we gedemonstreerd dat het selenizeren van CIS NCs naar $CuInSe_2$ beloftevol is, door het produceren van een werkende dunne-film zonnecel met een cel efficiëntie van 1.38 %.

De waarneming dat anorganische sulfide liganden het sinteren van CIS NCs tegenwerken, vergeleken met lange organische liganden, is het vertrekpunt van Hoofdstuk VIII. Onder inerte atmosfeer tonen de NCs weinig tot geen sintering bij temperaturen tot 450 °C. Dit is in contrast met de kristalgroei die we waarnemen bij het annealen in het bijzijn van gasvormig waterstof. We onderzoeken dit verschil grondig en schrijven het toe aan het gedrag van S^{2-} liganden aanwezig op het oppervlak van de CIS NCs. Onder reducerende atmosfeer valt het sinteren samen met het vrijkomen van H_2S, terwijl onder inerte atmosfeer sulfide wordt behouden, geoxideerd en hierdoor het sinteren blokkeert. Geoxideerde zwavelionen kunnen het gevolg zijn van zowel blootstelling aan lucht en de decompositie van solvent moleculen tijdens het anneal proces zelf. We tonen aan dat dezelfde bevindingen kunnen toegepast worden op andere NC systemen, wat voor een uitdaging zorgt wanneer het doel bestaat uit het sinteren van de NCs, maar een kans biedt tot het behouden van de NC eigenschappen bij verhoogde temperatuur.

In het laatste Hoofstuk IX combineren we de resultaten uit de synthese, analyse van de oppervlakchemie en de transformatie van CIGS precursoren om oplossingen te bieden voor regelmatig voorkomende problemen bij het gebruik van inkten voor CIGS absorber lagen. Extra reactiviteit tijdens de selenizatie van CIS NCs is bekomen door het toevoegen van CuS NCs. Om een optimale stoichiometrie te garanderen wordt het gebruik van indium zouten

geopperd, die ook de colloïdale stabiliteit positief beïnvloeden wat leidt tot kraakvrije, vlakke filmen. Deze gecombineerde precursor -zogenaamde hybride inkt- leidt tot een volledige transformatie door selenizatie naar $CuInSe_2$ met gebruik van relatief milde selenizatie condities. We tonen dat de kristalgroei verder kan bevorderd worden door de filmen vooraf te annealen. We zijn erin geslaagd van hieruit een dunne-film zonnecel te bekomen met een beloftevolle efficiëntie van 2.38 %, en benadrukken dat er ruimte is voor verbetering. Hiernaast onderzoeken we de toevoeging van selenium in de precursor inkt in een poging gasfase selenizatie te ontwijken en hierdoor het proces van precursor naar laag te vereenvoudigen. Onze voorlopige resultaten resultaten tonen duidelijk aan dat het toevoegen van selenium aan $CuInS_2$ een selenizatie effect teweeg brengt tijdens het anneal proces in een inerte atmosfeer. We besluiten dat het toevoegen van selenium door zowel Se NPs als selenium zouten aan precursor inkten zeer beloftevol is om de selenizatie in gasfase na te bootsen die gebruikt worden in nagenoeg alle oplossing gebaseerde methoden voor CIGS.

Publications

1. Boris Capon, Ruben Dierick, Zeger Hens and Christophe Detavernier.*In situ XRD during selenization of colloidal nanocrystals: $CuInSe_2$ formation and grain growth* **2015**. Thin Solid Films, in submission.

2. Ruben Dierick, Freya Van den Broeck, Kim De Nolf, Qiang Zhao, André Vantomme, José Martins and Zeger Hens. *Surface chemistry of $CuInS_2$ colloidal nanocrystals, tight binding of L-type ligands* **2014**. Chemistry of Materials, 26 (20), 5950-5957.

3. Ruben Dierick, Boris Capon, Hanne Damm, Stijn Flamée, Pieter Arickx, Els Bruneel, Dirk Van Genechten, Marlies Van Bael, An Hardy, Christophe Detavernier and Zeger Hens. *Annealing of sulfide stabilized colloidal semiconductor nanocrystals* **2014** Journal of Materials Chemistry C, 2 (1), 178-183.

4. Stijn Flamée, Ruben Dierick, Marco Cirillo, Dirk Van Genechten, Tangi Aubert and Zeger Hens. *Synthesis of metal selenide colloidal nanocrystals by the hot injection of selenium powder.* Dalton transactions **2013**, 42 (35), 12654-12661.

Acknowledgments

In this final part, I would like to thank some people and animals that helped me trough the last four years, a chapter that I'm about to close as I'm writing this.
First, I'd like to thank my promoter Zeger Hens, for giving me the opportunity to start my PhD on this very ambitious Soppom project, a project of which he was one of the main driving forces before and during its duration. His directions and advice surely kept me on track, and I'm proud to have been part of his group.
Boris and Freya, I spent countless trips between S1-S3-S4 to provide you guys with samples, which you were always eager to measure, analyze and provide fast feedback. An amount of measurements of which 0.32 % ended up in this thesis. I'd like to thank you guys for the nice cooperation and discussions we had, and to be able to put bad results in perspective so at least we could have a laugh. I hereby also thank their supervisors, Prof. Dr. Detavernier and Prof. Dr. Martins for providing valuable ideas and support. I'd also like to acknowledge Olivier from the S1 for SEM and XRD measurements.
Many samples were sent around in the framework of the Soppom program and measured/thrown away externally. In this respect I'd like to thank Armin, Marie and co-workers of the KU Leuven and IMEC for their dedication to the project, and the analysis on our samples, supported by Dr. Marc Meuris. In some cases our collaborations turned more into a competition, but I'll forgive Armin for that. I'm grateful to the people from the University of Hasselt and Imomec; Hanne, Ken, Prof. Dr. Van Bael and Prof. Dr. Hardy especially for the measurements and discussions regarding the annealing paper. It was also nice to have these people around during meetings that recognize the problems of synthesizing and handling large amounts of nanomaterials in a research lab.
Talking about large amounts of nanomaterials, I'd like to thank

Dr. Guido Huyberechts and the people from Flamac for adapting and performing our nanocrystal synthesis to produce the insane batch of 100 g of nanocrystals. This brings me to thanking Yolanda and Pieter Arickx for their aid in this crazy task of handling these huge batches. I'd also like to thank Pieter for his work on the stabilization of nanocrystals by chloride ions and his help with making samples and layers.
For help with administrative and practical issues I want to thank Pierre, Claudine, An, Bart and Pat. I want to acknowledge Els Bruneel for aid with respect to teaching and XPS measurements. Thank you Jonas for your guidance with the inkjet printing setup but not for dragging me in this PhD symposium. Luckily presentations are not synonyms with anxiety and stress any more.
I would like to thank everyone of the PCN group, which is expanding and changing so fast nowadays I can't keep track of all the names. That's also because I don't make an effort to do that. I'm grateful to Yolanda, Tangi and Raquel for being nice post docs, in contrast to the ones that were put on the Soppom project at PCN. Thank you Sofie for the friendship, also outside of work. Tom, Guillaume, Dorien and Timo for keeping in touch after our studies.
I want to thank my lovely Mieke for her love and support during our first year together; and the many years to come. Boom and William for being best friends trough all the madness. Jorrit and his co-workers I want to thank for their aid. I dedicate this work to my dog Boris, who passed away yesterday, at least that what it feels like. I would give a lot to go running and swimming with you just for one day buddy. Vedett, Gilbert and Siezel; 3 awesome cats I'd like to thank for their unconditional friendship. Finally, I want to thank my parents, brothers and sisters for their continuous support. I'm very grateful to have a family like this.

Gent, 2015
Ruben Dierick